Modelling Dye-Sensitised Nanocrystalline Solar Cells

Staff, Daniel

Award date:
2013

Awarding institution:
University of Bath

MODELLING DYE-SENSITISED NANOCRYSTALLINE SOLAR CELLS

Daniel Staff

A thesis submitted for the degree of Doctor of Philosophy

University of Bath

Department of Physics

July 2013

Abstract

Dye-sensitized Solar Cells (DSCs) and Solid State Dye-sensitized Solar Cells (ssDSCs) are photovoltaic devices with short energy payback times compared to existing technologies. DSCs and ssDSCs have the potential to become cheap flexible devices with new building integrated and portable applications.

Despite over 20 years of research fundamental steps in the operation, construction and measurement of DSCs and ssDSCs are still not completely understood. For example, the competition between the rate of electron transport through the anode and the rate of electron transfer to I_3^- ions in the electrolyte determines the efficiency of the cell. The diffusion length is proportional to the average distance an electron will travel though the anode before reacting with I_3^-. Conventionally electron transfer to I_3^- has been described by the rate equation $r = k_r n_c$ where n_c is the concentration of photoelectrons and k_r is a constant. Recently there has been an increasing body of evidence suggesting so called non-linear recombination where the reaction order is in fact less than one where $r = k_r n_c^\beta$ and $\beta < 1$. Many of the standard methods for cell characterization have been reinterpreted in light of this result, however an obvious omission is that there is no general model for electrochemical impedance spectroscopy (EIS) experiments when $\beta < 1$. We present a full EIS model for DSCs anodes, valid for the case where $\beta < 1$, and the resulting EIS spectra at different points along the J-V curve and for different reaction orders β. The results are consistent with published experimental data and show that the diffusion length calculated from EIS experiments ought to decrease as the cell is moved from open to short circuit conditions.

In light of non-linear reaction kinetics it has become increasingly important to measure the diffusion length as simply and unambiguously as possible. As such, a new method of measuring the diffusion length has been developed using patterned electrodes. The electron extracting electrode is etched such that the required diffusion length for 100% electron collection is changed. A simple 1D analytical model for patterned electrode experiments is presented so that the diffusion length can easily be extracted from experimental data. The 1D model is verified with a 2D finite element model.

Understanding the processes involved in DSC construction is equally important as those involved in DSC operation if the devices are to be manufactured on a large

scale. The application of light sensitizing dye to the anode is one such example. Since the anode is porous on the nanoscale the dying process is slow, commonly 12 hours are required to apply dye to the anode. To best understand dye application optical waveguide spectroscopy (OWS) has been used to monitor the amount of dye entering the anode. This thesis presents a model of dye diffusion and adsoption within the anode and an optical model of the OWS experiment. The two models are used to interpret the OWS data and show that dye is entering the anode well after 12 hours. The model is then used to demonstrate that the distribution of dye within the film can be observed if a high refractive index rutile prism is used to couple light into the film.

In ssDSCs the conventional liquid electrolyte is replaced with a chemically doped organic hole conductor. Kinetic Monte Carlo Simulations are used explain the relationship between the conductivity of the organic matrix and the doping level. The results, which are consistent with experimental observations, suggest that at low doping levels carriers fail to disassociate from their host dopants causing a decrease in mobility. This explains the only modest increase in conductivity seen at low doping levels.

Acknowledgements

I would like to thank Alison Walker for her supervision over last three years and all of my collaborators, in particular Petra Cameron, Laurie Peter, Halina Dunn, Antonio Abate and Henry Snaith.

I am grateful to the device modelling group and the community at the department of physics past and present for making my PhD an enjoyable experience. I am especially grateful to Timo Peltola for discussions regarding chapter 3 and to Ed Wright for general discussion for moral support.

Fantastic IT support from Adrian Hooper and Simon Dodd has been essential throughout this project.

Thank you to my family for encouraging and helping me to learn about physics and thanks to all of my friends for their support.

Declaration of the input of work done by others

All of the work in this thesis was carried out by the author with the following exceptions:

The frequency domain model in chapter 3 was built on unpublished work by Alison Walker.

Measurements of cells with patterned substrates have been carried out by Halina Dunn and Per-Oskar Westin and the corresponding figures were generated by Halina Dunn.

Conductivity measurements of organic conductors were all performed by Antonio Abate who generated the corresponding figures.

Publications arising from this thesis

Antun Peic, Daniel Staff, Thomas Risbridger, Bernhard Menges, Laurence M. Peter, Alison B. Walker, and Petra J. Cameron. Real-time optical waveguide measurements of dye adsorption into nanocrystalline tio2 films with relevance to dye-sensitized solar cells. *The Journal of Physical Chemistry C*, 115(3):613–619, 2011.

Halina K. Dunn, Per-Oskar Westin, Daniel R. Staff, Laurence M. Peter, Alison B. Walker, Gerrit Boschloo, and Anders Hagfeldt. Determination of the electron diffusion length in dye-sensitized solar cells by substrate contact patterning. *The Journal of Physical Chemistry C*, 115(28):13932–13937, 2011.

Antonio Abate, Daniel Staff, Derek J. Hollman, Henry J. Snaith and Alison B. Walker. Influence of Ionizing Dopants on Charge Transport in Organic Semiconductors. *In preparation.*

Dedicated to Sarah Bough

Contents

Chapter 1

Introduction

Since the early 1990's photoelectrochemical methods have emerged as an alternative to solid state photovoltaics which became available in the late 1950's, primarily for use in the space program [1]. This totally new approach for harvesting energy from the sun is justified by a new motivation. The initial brief for the solar cell was a highly efficient device which produces the most power from a minimal mass of materials. High efficiency was critical and high cost was tolerated. We now face a global energy supply problem [2, 3, 4]. Most energy arrives on the planet in sparsely populated areas and people living in such areas often can not afford to take advantage of it [5]. Solid state cells have been demonstrated with staggering efficiencies in excess of 35% yet we continue to consume non-renewable sources of energy [6, 7]. As a global community we do not necessarily require efficient conversion of sunlight into useful energy. The new brief for the solar cell requires the affordable conversion of sunlight into useful energy and the means to distribute it to wherever it is needed.

Manufacture of p-n junction based silicon solar cells is energy intensive. Consequently the minimum energy payback time for commercial devices is approximately three years and around 5GJ are needed to produce a $1m^2$ silicon solar cell [8, 9]. The dye-sensitized solar cell (DSC), first reported in 1991, is a promising photovoltaic (PV) device which has been championed for the use of cheap abundant materials, simple construction and short energy payback times of less than one year [8, 10]. In addition DSC can be manufactured with different translucent colours onto flexible substrates paving the way for new applications

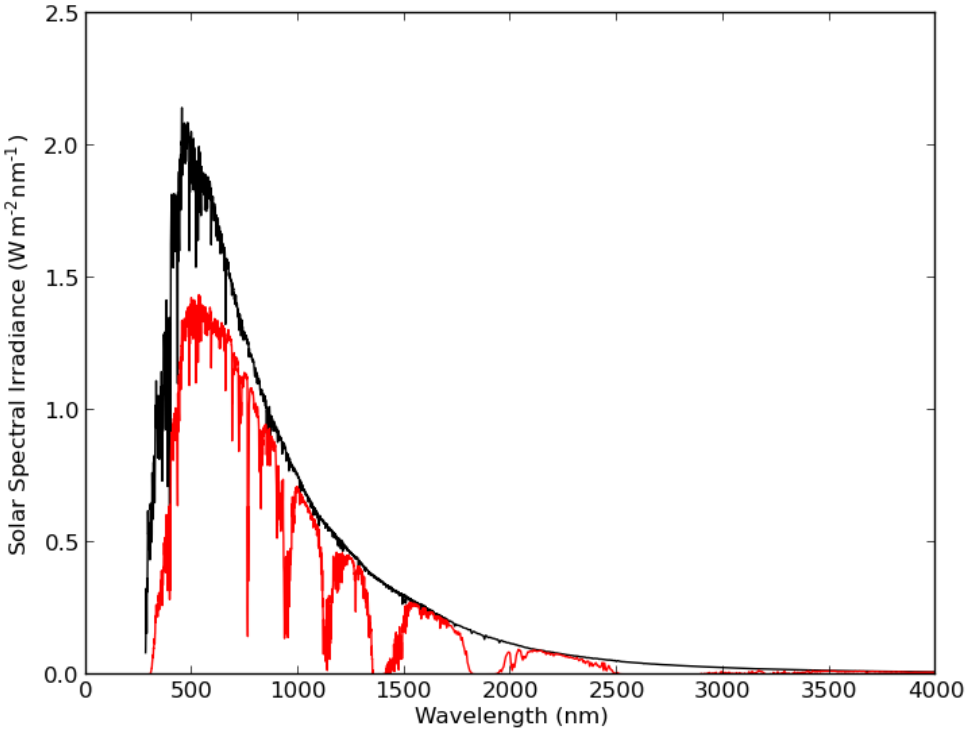

Figure 1.1: The extraterrestrial solar irradience (black) and the AM1.5 standard solar irradience (red) provided by NREL.

such as windows for building integrated PV [1].

In section 1.1 the feasibility of the sun as a limitless source of power is examined followed by an introduction to some fundamental photovoltaic principles. In section 1.2 the conventional p-n junction solar cell is introduced followed by the DSC in section 1.3 and the solid state DSC in section 1.4. An overview of the other chapters in this can be found in section 1.6.

1.1 PV fundamentals

Before examining the dye-sensitized solar cell it will be helpful to introduce some ubiquitous concepts in the field of photovoltaics.

1.1.1 The solar spectrum

The sun is a large and plentiful source of energy. 1.7×10^{17}W of energy is radiated from the sun towards the earth, approximately equivalent to 1.8×10^{14} metric tons of coal arriving on the planet per year. This dwarfs the 1.32×10^{9} metric tons of coal required to completely power the planet in 2002 [3]. [1]

Solar radiation arrives at the surface of the earth at different frequencies. The intensity and angle changes as the elevation of the sun changes throughout the day. When comparing the performance of different solar cells it is important to measure the cells consistently and under typical conditions. For this reason the National Renewable Energy Laboratory in Colorado has published the Air Mass 1.5 Standard for Solar Irradience (AM1.5 standard) [11]. This is the solar irradience from the sun after the light has travelled through an atmosphere 1.5 times as thick as the earth's atmosphere. Solar irradience is defined such that the integral of solar irradience between wavelength a and b is the power arriving on the ground per square meter between the two wavelengths. The AM1.5 spectrum is plotted in figure 1.1.

1.1.2 Figures of merit

The following universal measurements are important for comparing the performance off different devices and assessing why performance is good or poor.

The I-V curve

Figure 1.2 is typical of all PV devices and is normally referred to as a J-V curve (or I-V curve). The cells are held at a set of fixed biases and the current density (current / area of cell) is recorded at each instance. The bias required between the terminals to bring the current density to zero is V_{oc}. Equivalently this is the potential difference across the cell under open circuit conditions (infinite resistance between the terminals). At zero applied bias the terminals are shorted

[1] Of course a mixture of mainly coal, gas, oil and nuclear power continues to be used rather than just coal.

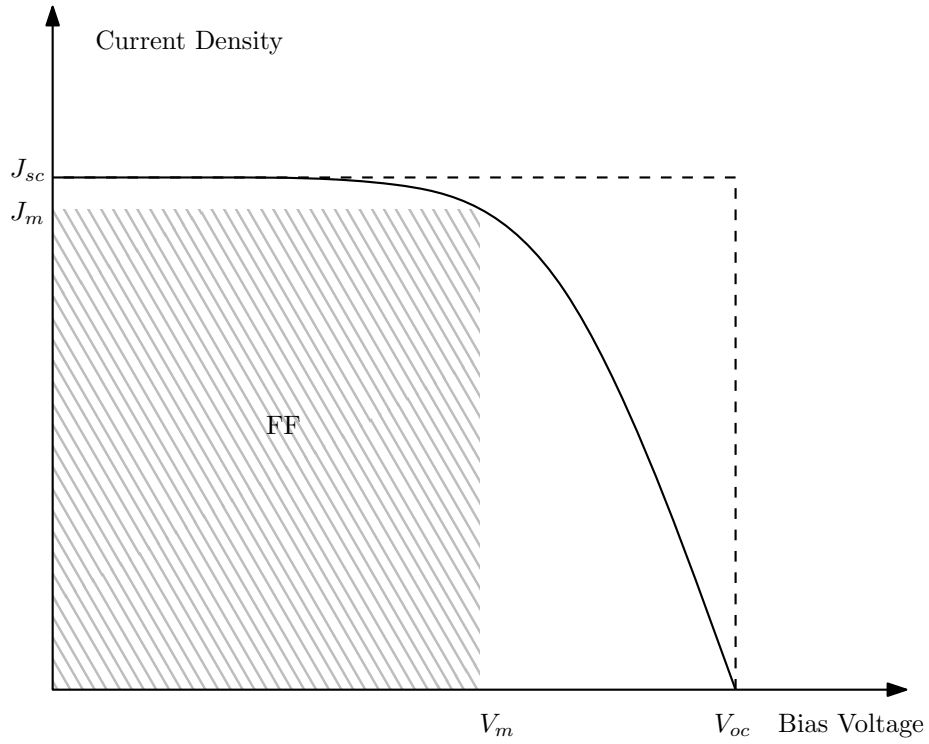

Figure 1.2: A generic plot of the current density - voltage curve for a generic photovoltaic device with the key features marked.

together and the short circuit current will flow, J_{sc}. The most power is generated when the product of the bias voltage V and current density J is maximum. At this point $J = J_m$ and $V = V_m$. The fill factor FF is defined as [11]

$$\mathrm{FF} = \frac{J_m V_m}{J_{sc} V_{oc}}. \tag{1.1}$$

FF is equivalent to the area of the shaded region divided by the area of the rectangle formed by the dashed line in figure 1.2. If there is a power P incident of the cell the efficiency is the device is

$$\eta = \frac{J_{sc} V_{oc} \mathrm{FF}}{P}. \tag{1.2}$$

It is clear from equation 1.2 that J_{sc}, V_{oc} and FF must be maximized if the cell is to be as efficient as possible.

Efficiency

In the most general terms the efficiency of a device converting sunlight into another form of energy under AM1.5 conditions at every wavelength λ is given by the solar energy conversion efficiency [11]

$$\eta = \frac{1}{\text{Device Area}} \int_0^\infty \frac{J_{sc} V_{oc} \text{FF}}{\text{AM1.5 Solar Spectral Irradience}(\lambda)\ d\lambda}. \tag{1.3}$$

In addition it is useful to define the incident photon to current conversion efficiency (IPCE). Under monocromatic conditions as [11]

$$\text{IPCE} = \frac{\text{rate of electrons out}}{\text{rate of photons incident of cell}}. \tag{1.4}$$

This is a measure of the cells ability to absorb photons at a given wavelength and deliver them to the external circuit [11]. The IPCE can be contrasted with the absorbed photons to current conversion efficiency (APCE) [11],

$$\text{APCE} = \frac{\text{rate of electrons out}}{\text{rate of photon absorption}}, \tag{1.5}$$

which is purely a measure of the fraction of electrons delivered to the external circuit. A low APCE is a sign that electrons are either flowing through the chassis of the device or undergoing recombination, otherwise known as back reactions. In the next section the solid state solar cell is explored and recombination is explained.

1.2 The p-n junction cell

A cell formed around a p-n junction is pictured in figure 1.3. Due to the intensional addition of defect atoms, electrons in the n-type region of the semiconductor have a higher chemical potential than those in the p-type region. When the two regions are joined, electrons diffuse into the p-type layer resulting in a depletion layer where there is net negative charge on the p-type side and net positive charge on the n-type side. The junction reaches equilibrium when the diffusion of electrons is balanced by drift of electrons moving in the opposite direction due to the electric field between the charged regions. This results in a permanent

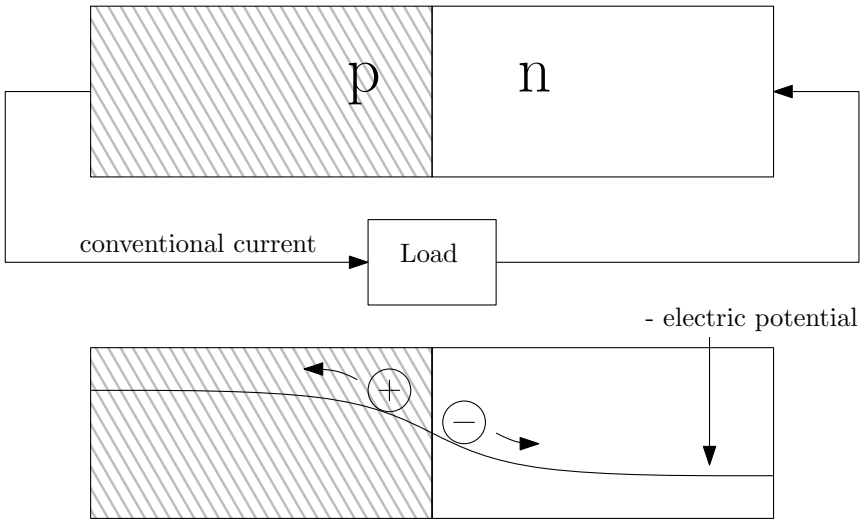

Figure 1.3: A diagram of a solid state solar cell with a built in voltage separating electrons and holes.

electric field at the boundary.

Incoming photons will be absorbed by the cell if the energy exceeds a critical material specific value referred to as the bandgap E_g. Photons can be absorbed anywhere within the device and the energy from the photon is transferred to an electron by moving it into an excited state (photoexcitation). The electron is now mobile and may be referred to as a photoelectron, the charge of the photoelectron must be balanced by a positive charge. This positive charge or hole is also free to move and is the second of the two carrier types. Electrons and holes are separated by the permanent electric field at the p-n junction and the build up of positive charge at one side of the cell and negative charge at the other creates a potential difference (photovoltage) across the device.

Recombination occurs when electrons and holes pair back together and heat is released rather than electrical potential energy. The presence of defects in the semiconducting crystal increases recombination; so extremely pure and precisely doped materials are required to make high performance cells.

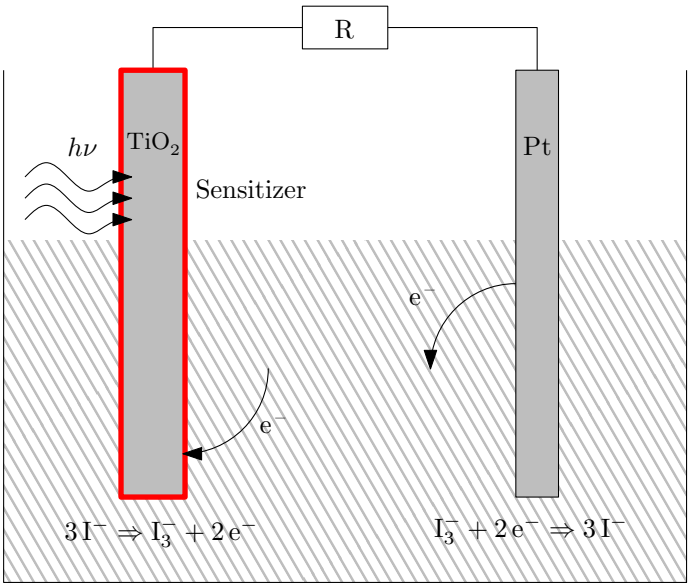

Figure 1.4: A dye-sensitized solar cell drawn as an electrochemical cell with a TiO_2 photoanode, Pt counter electrode and I^-/I_3^- redox couple.

1.3 The Dye-sensitized Solar Cell (DSC)

In a dye-sensitized solar cell the p-n junction is replaced by a junction between two different materials such as a liquid electrolyte and a semiconductor (predominantly TiO_2 and I^-/I_3^- in an organic solvent) in order to separate charge. They rely on mesoscopic networks of two different interpenetrating materials and extremely fast charge separation. Typically, they capture light from all angles, increase in efficiency as temperature rises and require far less energy for manufacture than solid state cells [9].

In the example shown in figure 1.4 a TiO_2 and a Pt electrode are immersed in an electrolyte containing a I^-/I_3^- redox couple. Under illumination iodide is created at the anode from triiodide and the reverse reaction takes place at the cathode leaving no net chemical change in the cell. TiO_2 has a high bandgap (> 3eV) [9]. Sensitizers (such as the archetypal ruthenium based dye N719) are used to absorb photons and inject electrons into the TiO_2 anode. N719 dye has absorption peaks at 400nm and 535nm [9]. Above 700nm the device becomes insensitive to visible light and a large proportion of the spectrum is not utilised. This sensitivity to visible light means that solar energy conversion efficiencies for DSCs have been demonstrated in excess of 10% and the adsorption peaks of organic dyes can be advantageous for building integrated photovoltaics since they can give the

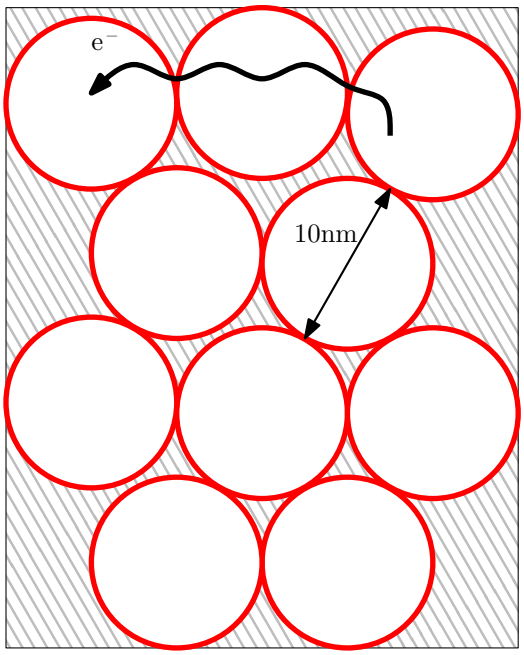

Figure 1.5: The mesoscopic structure of a TiO_2 electrode (shown in white) as used in photoelectrochemical solar cells.

appearance of translucent stained glass.

Figure 1.4 shows the most common materials for DSCs however there are many variations using different materials and chemicals. For instance, other metal oxides such as SnO_2 and ZnO have been used as alternatives to TiO_2 [12, 13]. Cobalt based redox electrolytes have reached competitive efficiencies over 12% using highly panchromatic dyes and greater than 7% efficient organic hole transporter cells have been reported [14, 15, 16]. Throughout this thesis conventional TiO_2 and I^-/I_3^- cells will be referred to for consistency, but the work will generally be applicable to all of these systems (with the exception of organic hole conductors which will be the subject of chapter 6).

A single molecular layer of dye is weakly adsorbing so planar devices give efficiencies less than 1%. It is essential to use a porous anode with a structure on the nanoscale to produce a high surface area. This way a photon will encounter many dye molecules as it passes through the anode and the chance of photoexcitation is greatly increased. A fundamental difference between solid state cells and DSCs is that light is only absorbed at the interface of a DSC, hence the requirement for a mesoporous structure in DSCs and a planar structure in solid state devices.

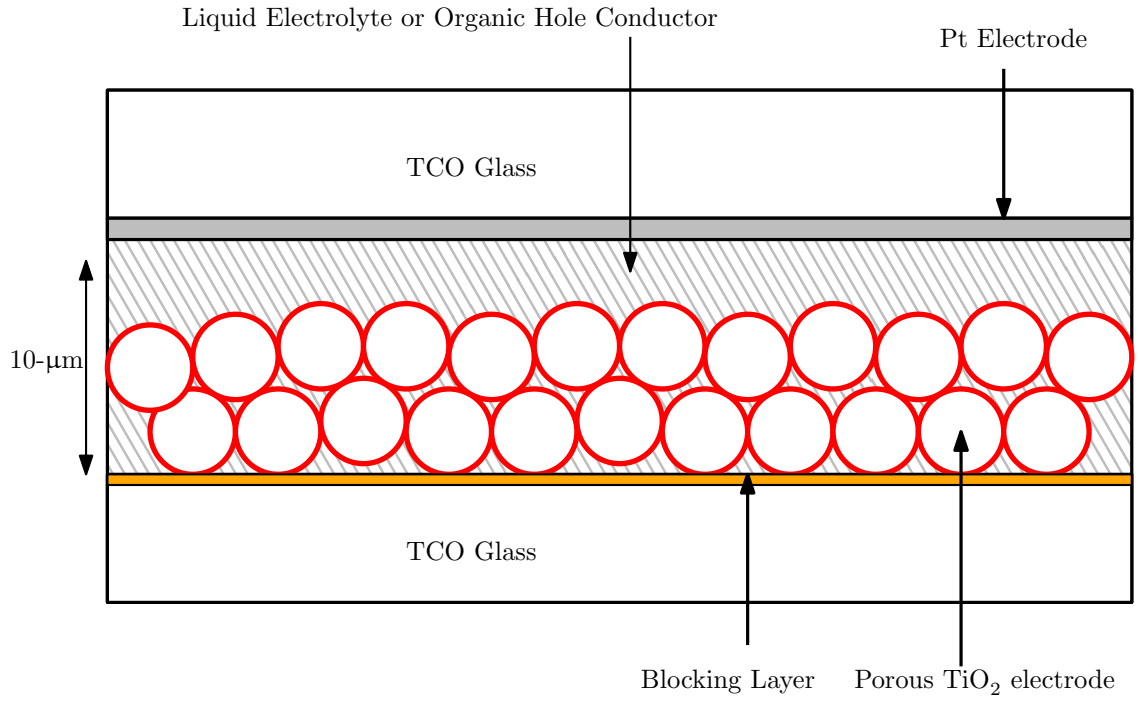

Figure 1.6: The conventional construction of a dye-sensitized solar cell with the key components labelled.

Figure 1.5 shows the mesoscopic structure of a DSC photoanode. It is composed of spherical TiO_2 grains with an average diameter of around 10nm sintered together to form a film with $50 - 65\%$ porosity, the average pore size it typically 15nm and the film thickness is between 5 and 20µm [17]. Photons transfer energy to the dye to form an excited state (photoexcitation). The excited dye subsequently relaxes by transferring an electron to the semiconducting anode (photoinjection) and is regenerated by receiving an electron from the electrolyte [18]. No electric fields are present in the anode over length scales larger than the diameter of the grains because of screening from the electrolyte solution. This is evidenced by the absence of any potential difference between different points in the film [19]. Consequently electrons move purely by diffusion through the film. Holes are transferred directly to the electrolyte and are completely separated from the electrons unlike in a p-n junction solar cell.

DSCs are usually manufactured between sheets of glass with a conducting flourine doped tin oxide (FTO) layer [20, 1]. The compact layer of TiO_2 is required at the porous TiO_2 / FTO contact to prevent electrolyte shorting the cell by contacting both glass slides (shown in orange on figure 1.6). Briefly, the cell is constructed as follows: Paste containing TiO_2 nanoparticles is applied to FTO glass by hand using a doctor blade technique. The glass is baked in an oven where organic

matter in the paste combusts leaving behind TiO_2 nanoparticles sintered together to make a film. The film is then placed in dye solution for up to 24 hours. The gap between the slides is of the order of 25μm and is maintained with a gasket which also glues the slides together. Finally, electrolyte is injected into the assembled cell through a small hole which must be subsequently sealed. This results in the structure pictured in figure 1.6 [1].

The fundamental steps in the cell are as follows [1, 21]:

1.3.1 Reaction Steps

Light Harvesting: Photons are absorped by dye molecules on the TiO_2 surface creating excited dye molecules

$$h\nu + S^0|TiO_2 \rightarrow S^*|TiO_2. \tag{1.6}$$

Electron Injection: Excited electrons are injected from the excited dye into the TiO_2

$$S^*|TiO_2 \rightarrow S^+|TiO_2 + e^-(TiO_2). \tag{1.7}$$

Dye Regeneration: Excited dye is reduced by I^-, I^- is oxidized to form $3\,I^-$

$$S^+|TiO_2 + \tfrac{3}{2}I^- \rightarrow S|TiO_2 + \tfrac{1}{2}I_3^-. \tag{1.8}$$

Electrolyte Regeneration: I_3^- is reduced to I^- by electrons which have done work through the external circuit.

$$I_3^- + 2\,e^-|Pt \rightarrow 3\,I^-. \tag{1.9}$$

1.3.2 Transport Steps

There are two principle transport steps:

Electron Transport: Injected electrons diffuse through the TiO_2 anode and are collected at the substrate to do work through the external circuit.

Electrolyte Mass Transport: Electron acceptors (typically I_3^-) diffuse through the TiO_2 anode to the platinum counter electrode and electron donors (typically I^-) diffuses from the counter electrode to the TiO_2 surface.

1.3.3 Recombination Steps

In addition there are two recombination pathways and the excited state decay that reduce efficiency .

Electron dye-recombination:

$$S^+|TiO_2 + e^-(TiO_2) \rightarrow S|TiO_2 \tag{1.10}$$

Electron-electrolyte recombination:

$$2e^-|TiO_2 + I_3^- \rightarrow 3\,I^-. \tag{1.11}$$

Excited state decay: the decay of dye back into the ground state before electron injection

$$S^*|TiO_2 \rightarrow S^0|TiO_2. \tag{1.12}$$

1.4 The Solid State Dye-sensitized Solar Cell

The Solid State Dye-sensitized Solar Cell (ssDSC) is similar to a DSCs however the liquid electrolyte is replaced with an organic hole conductor such as 2,2,7,7-tetrakis(N,N-di-p-methoxyphenyl-amine)9,9-Spirobifluorene (Spiro-OMeTAD). Typically, the counter electrode is made from silver rather than platinum [20]. The first demonstrated ssDSCs had an overall efficiency of 0.74% and since then the record efficiency now stands at over 7.1% [15, 16]. Charge screening in ssDSCs is not as effective. The anode thickness of these devices is limited to several microns because of poor pore filling [20].

Table 1.1: Top device efficiencies [6, 22, 16, 14].

Device	Efficiency(%)	V_{OC}	I_{SC}	FF
Crystalline Si	25.0	0.706	42.7	82.8
DSCs	12.3	0.935	17.66	74
$CH_3NH_3PbI_2Cl/Al_2O_3$ ETA	10.9	0.98	17.8	0.63
Amorphous Si	10.1	0.886	16.75	67.8
$CH_3NH_3PbI_2Cl/TiO_2$ ETA	7.6	0.8	17.8	0.53
ssDSCs	7.2	0.986	9.5	0.76

1.4.1 Perovskite Absorber Cells

In 2012, perovskite ($CH_3NH_3PbI_2Cl$) absorber cells were reported with an efficiency of 10.9% [22]. The organic dye used in DSCs and ssDSCs is replaced with a perovskite extremely thin absorber (ETA) layer. In this configuration the cells were measured with an overall efficiency of 7.6% under AM1.5 conditions. When the TiO_2 nanoparticles were replaced with Al_2O_3 (a wide bandgap semiconductor $E_g > 7$eV) the efficiency increased to 10.9%. The mismatch of energy levels between Al_2O_3 and perovskite mean that it will play no role in charge transport [22]. This is a large departure from the Al_2O_3 ssDSCs as only the organic hole conductor Spiro-OMeTAD is retained for extracting holes from the device. Light harvesting and electron transport are provided by one single material. This highlights the importance of materials such as Spiro-OMeTAD in emerging devices and also the diversity of emerging devices which bare little resemblance to DSCs.

1.5 Analysis

Table 1.1 gives a breakdown of some devices for comparison with DSCs. The crystalline Si cell and the DSC have a similar V_{OC} however J_{SC} is almost double that of the DSC. This is indicative of the band gap of Si (1.1eV) which will harvest photons at wavelengths of 1365nm and below; however, N719 sensitized TiO_2 is insensitive above 700nm [20]. The DSC is only harvesting approximately half of the incoming photons and has approximately half the efficiency of top crystalline cells. There is clearly a need for dyes with a broader sensitivity [20].

Amorphous silicon is an excellent absorber of light but the disorder gives electric properties resulting in a J_{SC} and FF lower than top DSCs. Given the DSC are disordered devices which absorb far fewer photons than amorphous Si the charge transport properties of DSCs are impressive. Indeed, even the first reported DSC had an IPCE of greater that 80% [10]. It would be tempting to conclude that improvement of electron transport in DSCs is not necessary however, attempts to make DSCs sensitive to a broader band of the solar spectrum invariably result in either reduced efficiency or stability, hence improved charge transport may result in a wider range of useful materials for DSC designs.

The ssDSC has half the J_{SC} of top DSC which suggests that the ssDSC could be at least as efficient as the regular DSC if the charge collection efficiency was comparable. The $CsSnI_3/TiO_2$ cell has similar performance to ssDSCs however when TiO_2 is replaced with $CsSnI_3$ perovskite this leads to a dramatic increase in V_{OC} and hence efficiency. If the light harvesting efficiency and charge collection of $CsSnI_3/TiO_2$ matched that of DSCs then the efficiency could be increased even further.

1.6 Overview of Thesis

The thesis focuses on the simulation of DSCs. Each chapter presents a different computational problem relating to different aspects of DSCs operation or construction with the exception of chapter 2.

1.6.1 Chapter 2

Chapter 2 will examine the properties of materials for DSCs in much more detail. In particular the band model of semiconducting materials will be reviewed, especially in the context of liquid junctions. Then the standard mathematical model for DSCs will be presented. This model will form the foundation for chapters 3 and 4.

1.6.2 Chapter 3

Chapter 3 builds on the standard model of DSCs presented in Chapter 2 to model the frequency response of DSCs. The model is then used to demonstrate how to measure the rate of recombination reactions in DSCs and verify the voltage dependence of these processes.

1.6.3 Chapter 4

Chapter 4 builds on the standard model of DSCs presented in Chapter 2 to demonstrate how to measure the collection efficiency and diffusion length of electrons in TiO_2 DSC photoanodes. The work is applied to some experimental measurements to show that, on average, electrons travel of the order of 100μm in TiO_2 DSC photoanodes before undergoing recombination.

1.6.4 Chapter 5

Chapter 5 is concerned with the application of dye to TiO_2 anodes for DSCs. A model is made of an optical sensor which can detect the whereabouts of dye within the film in real time during the dye application process. Typically, TiO_2 films are dyed during a $\sim$ 12 hour process, a key result from this chapter is that major changes in the distribution of dye are still taking place on much longer time scales.

1.6.5 Chapter 6

Chapter 6 models the doping of organic semiconductors used for ssDSCs. The model is used to identify the ideal concentration of doping molecules in the semiconductor.

Chapter 2

Theory

DSCs rely on a junction between a liquid and a solid in order to separate charge, so a basic understanding of this interface is essential. In particular, the interface is formed between a semiconductor electrode and a liquid electrolyte. The electronic properties of semiconductors will be reviewed before examining the semiconductor/electrolyte interface. Finally, semiconductor surface states must be accounted for because of the extremely high surface area of the TiO_2 semiconducting anode. In the second half of this chapter a basic model of DSCs will be formed.

2.1 The Band Model of Semiconductors

For an isolated atom the electrons are confined to discrete atomic orbitals with definite energy levels. Only two electrons of opposite spin may occupy each orbital and additional electrons must occupy higher orbitals. As atoms are brought closer together to make a crystal the energy levels broaden to form energy bands separated by forbidden regions or band gaps as pictured in figure 2.1. The Fermi level is defined as the energy where the probability of occupation is one half. If the Fermi level is in a forbidden gap between energy bands and the band gap is large then the material will be insulating. The band immediately below the Fermi level is called the valence band and the band above is called the conduction band.

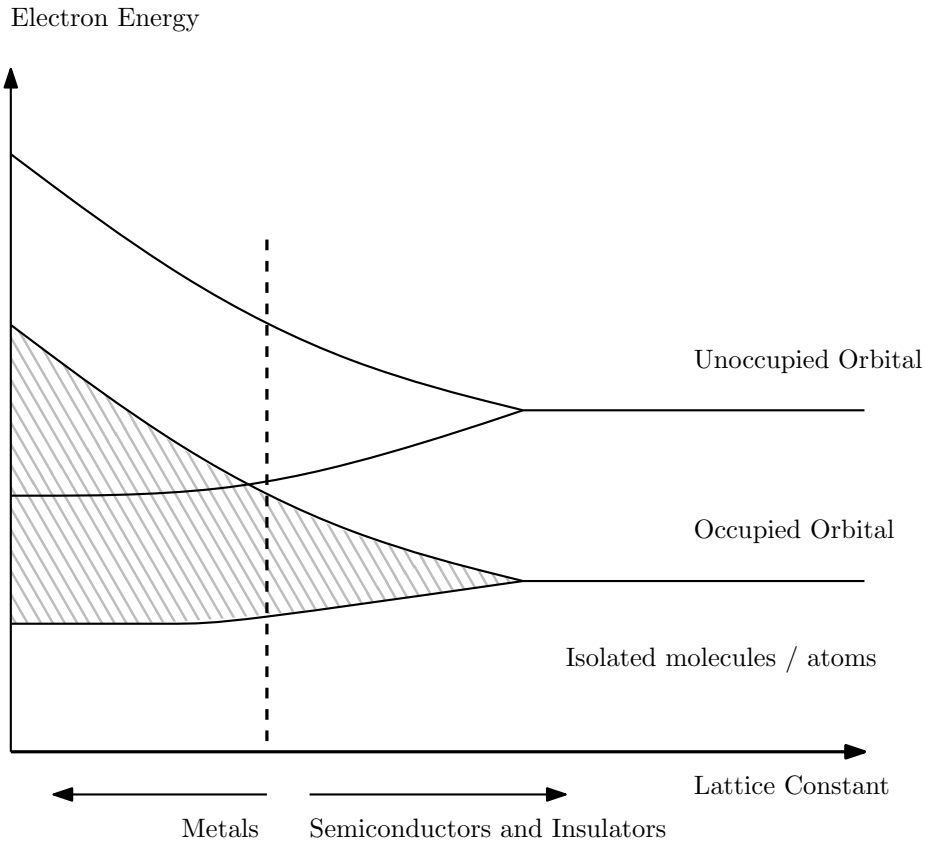

Figure 2.1: An illustration showing the transition from atomic orbitals around isolated atoms to the energy bands found in a crystal of atoms. If the fermi level is between the two states then the transition from metal to insulator is marked by the dashed line where the two bands merge.

If the Fermi energy is within one of the bands the material is a metal and states resulting in a net current are available. The semiconducting case occurs when the band gap is small or the Fermi level is close to the conduction band edge. In this case electrons can be thermally or optically excited across the band gap into the conduction band and current may flow.

In figure 2.2 an incoming photon has excited an electron into the conduction band. E_g and E_f are labelled. The resulting positive charge in the valance band forms a hole. Electrons and holes may recombine and annihilate each other in the reverse process to excitation. The number of electronic states per energy interval is the density of states (DOS with units $\mathrm{cm}^{-3}\mathrm{eV}^{-1}$). In general, the DOS is a complex function of energy. For the purposes of this thesis it will be sufficient only to consider the effective density of states at the conduction band edge. This is because the density of electrons in the conduction band will always be small compared to the DOS. All of the electrons are to good approximation

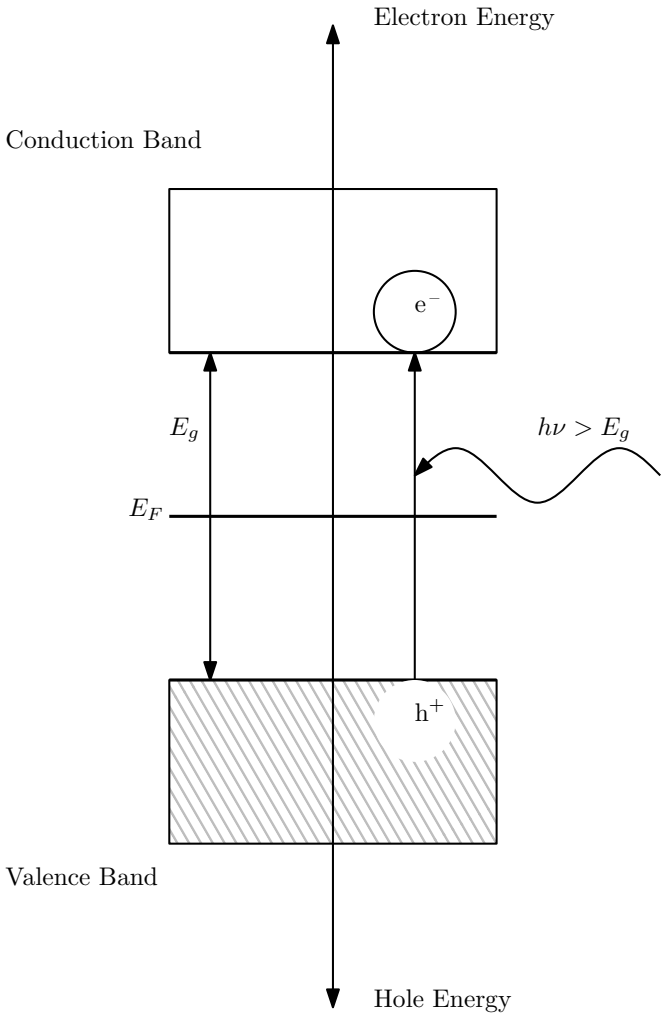

Figure 2.2: The simple model of band structure with no energy dependence. Each band is separated by an energy E_g. For a semiconductor where the valence band is approximately full and the conduction band empty the Fermi energy E_F must be half way between the two bands. An incident photon of frequency ν can excite an electron into the conduction band if $h\nu > E_g$ where h is Planck's constant.

at the band edge. For example, the density of states in porous TiO_2 electrodes has been determined electrochemically and theoretically to be of the order of $10^{19}\text{cm}^{-3}\text{eV}^{-1}$[23, 24, 25]. Typically, the electron density in a DSC will be of the order of 10^{16}cm^{-3} spread over $30 - 100\text{meV}$ [24]. It is common to refer to N_c as the density of states, more precisely this is the concentration of electrons in the conduction band when the Fermi level is at the conduction band edge. From this point onwards it is assumed that $E_F \leq E_c$ since this is the case under any reasonable operating conditions for DSCs.

The energy of the different energy bands/levels in a DSC are shown in figure 2.3. The energy of the ground state and the excited state of the dye are displayed and

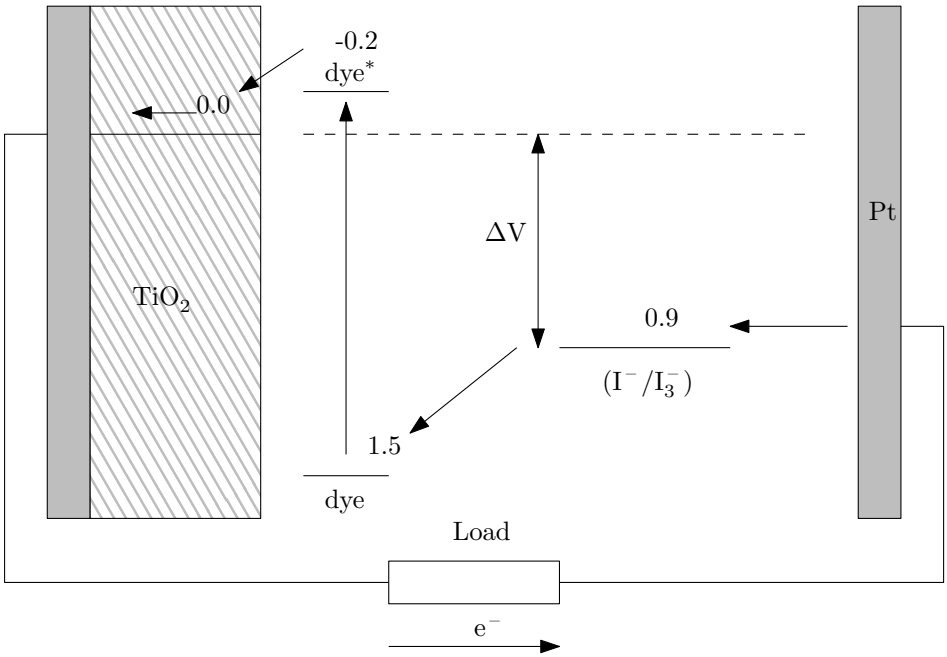

Figure 2.3: Schematic of a DSC with potentials marked in volts relative to the TiO_2 conduction band away from the surface. Note the $\sim$ 600meV overpotential for dye regeneration. ΔV represents the maximum possible photovoltage.

only the TiO_2 conduction band is shown.

2.2 The Chemical Potential

At equilibrium the energy of an electron at the Fermi level is identical to the chemical potential, μ, formally defined as the change in Gibbs free energy with respect to number of particles at constant temperature and pressure

$$\mu = \left(\frac{\partial G}{\partial n}\right)_{T,P}. \tag{2.1}$$

Note that this means, by definition, μ is constant across the device at equilibrium. In the dark the chemical potential for electrons is ${}_nE_{F,redox}$ everywhere and there is a concentration $n_{c,eq}$ of electrons in the TiO_2 conduction band (in practice this concentration is minuscule, less than 10^4 cm^{-3} [26]). Strictly speaking, under illumination the chemical potential given by equation 2.1 is not valid since the cell is not in equlibrium and one must resort to working with a quasi Fermi level. Providing electrons are locally at equilibrium with their immediate environment a quasi-fermi level, ${}_nE_F$ can be defined in terms of the electron concentration at

any point. Since no long range electric fields are present the photovoltage can be written in terms of the chemical potential of an ideal gas of electrons where the chemical potential is related to the concentration n by [27]

$$\mu_e \approx {}_nE_F \propto k_B T \ln(n/n_0). \tag{2.2}$$

For our purposes, n_0 is merely a constant that defines the zero potential. Hence potential differences can be described as [27]

$$V = qU_{photo} = {}_nE_F - {}_nE_{F,redox} = k_B T \ln\left[\frac{n_c}{n_{c,eq}}\right] \tag{2.3}$$

remembering that in the dark the potential is $E_{F,redox}$ across the device. The voltage measured across the device V is the difference in chemical potential between the anode-electrode contact and the counter electrode. This can be rearranged to calculate n_c [27],

$$n_c = N_c \exp\left[-\frac{E_c - {}_nE_F}{k_B T}\right], \tag{2.4}$$

remembering that $E_F \leq E_c$ for reasonable operating conditions. Each conduction band electron is considered to be an independent particle moving between an infinite number of states at the conduction band edge. When the Fermi energy is at the highest possible value $E_c = {}_nE_F$ there is a concentration N_c of electrons in the conduction band.

2.3 The Electrolyte-Semiconductor Interface

It can be seen in figure 2.3 that the potential of (I^-/I_3^-) is 0.9V higher than the TiO_2 conduction band. When TiO_2 is brought into contact with (I^-/I_3^-) electrons will flow from the TiO_2 conduction band into the electrolyte to make the chemical potential continuous across the interface and a depletion layer is formed. The mobile charge is provided by a tiny number of intrinsic dopants (impurities) [29]. A layer of negatively charged ions in the electrolyte is balanced by an exponential distribution of positive donor states decaying into the TiO_2 [29]. This is conventionally depicted as a bending of the conduction and valance bands so that electrons generated at the interface are driven away from the interface and holes are driven toward it as in figure 2.4.

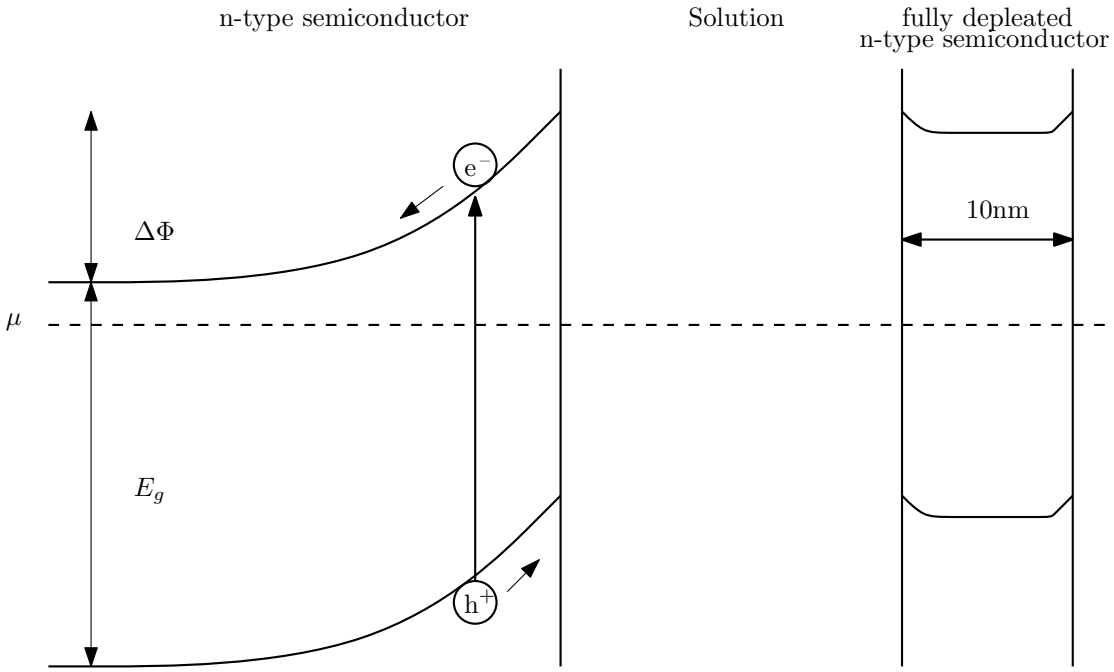

Figure 2.4: Band bending for a planar n-type semiconductor - electrolyte interface and a nanoscale n-type semiconductor-electrolyte interface. The planar interface will separate electrons and holes but, according to Albery and Bartlett, the change in potential between the surface and interior of a nanoscale semiconductor will be small compared to the thermal energy k_BT and there will be no separation [28].

2.3.1 The Fully Depleted Regime

In DSCs the anode consists of small spheres of TiO_2. The band bending can be predicted by the formalism of Albery and Bartlett who derived the difference in potential $\Delta\phi$ between the center $r = 0$ and the surface of a spherical semiconductor with radius r as

$$\Delta\phi = \frac{k_BT}{6e}\left(\frac{r - r_W}{L_D}\right)^2\left(1 + \frac{2 - r_W}{r}\right) \tag{2.5}$$

where r_W is the position of the edge of the depletion layer and L_D is the Debye length [28]. For small r ($< 1\mu m$) this simplifies to

$$\frac{e\Delta\phi}{k_BT} = \frac{1}{6}\left(\frac{r}{L_D}\right)^2. \tag{2.6}$$

The Debye length in TiO_2 is much larger than 10nm so the change in potential energy across the particle is not significant compared to the thermal energy k_BT

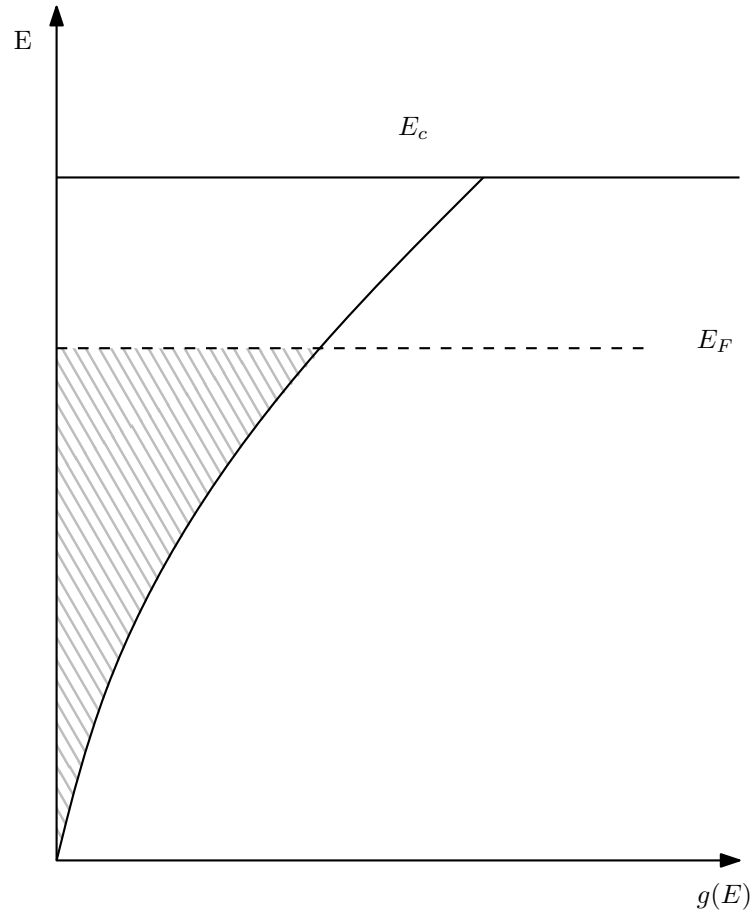

Figure 2.5: The experimentally observed distribution of electronic trap states $g(E)$ as a function of energy E in a DSC TiO_2 photoanode given by equation 2.7.

so band bending is not significant [29, 27].

2.3.2 Semiconductor Surface States

In 1948 Shockley and Pearson constructed a parallel plate capacitor from a thin sheet of n-type germanium and a metal plate [30]. By applying a negative potential to the metal plate, an increase in carrier density and, hence, conductivity was observed in the germanium. However the increase in conductivity was only one tenth of what would be expected. It was suggested by Bardeen that the extra charge was residing in immobile surface states in the germanium and this accounted for the absent increase in conductivity [31]. Similar immobile trap states are normally referred to as traps in the context of electrochemical solar cells.

Trap states in TiO_2 electrodes have been measured using IR illumination techniques [32]. It has become generally accepted that the density of trap states has the form [33, 32, 26, 34, 35, 27]

$$g(E_t) = \frac{N_{t,0}}{k_B T_0} \exp\left(-\frac{E_c - E_t}{k_B T_0}\right). \tag{2.7}$$

$N_{t,0} = 10^{19} - 10^{20}\text{cm}^{-3}$ is the total density of trap states at the conduction band edge and $T_0 = 600 - 1500\text{K}$ is the trapping temperature [26].

Electrons are assumed to obey Fermi-Dirac statistics so the probability of a state of energy E being occupied is given by [27]

$$f_{FD}(E) = \frac{1}{1 + \exp\left[\frac{E - {}_nE_F}{k_B T}\right]} \tag{2.8}$$

and the number of trapped electrons is therefore [27]

$$n_t = \int_{E_{F,redox}}^{E_c} f_{FD}(E) g(E) dE. \tag{2.9}$$

It is common to invoke the zero Kelvin approximation where f_{FD} reduces to a step function so that [27]

$$n_t = \int_0^{{}_nE_F} g(E) dE. \tag{2.10}$$

2.4 The Continuity Model for DSCs

Using the continuity equation, a surprisingly simple model can be constructed to solve for the concentration of electrons in the conduction band of a DSC anode, n_c [26, 36],

$$\frac{\partial n_c(x,t)}{\partial t} = G(x) - R(x, n_c) + D_0 \frac{\partial^2 n_c(x,t)}{\partial x^2} - \frac{\partial n_t(x,t)}{\partial t} \tag{2.11}$$

G is the generation term and represents the rate of electrons generated per unit

volume. R is the recombination term and represents the rate of electrons lost per unit volume. D_0 is a diffusion coefficient. n_t is the concentration of trapped electrons. n_c is the concentration of mobile electrons.

The current density at any point can be calculated using the spatial derivative of n_c (Fick's law) [27]:

$$J(x,t) = D_0 \frac{\partial n_c(x,t)}{\partial x}. \tag{2.12}$$

The continuity equation relies on the following approximations:

- There are no long range (> 10nm) electric fields.
- ${}_nE_F$ is less than E_c.
- The carrier concentration in the dark is small.
- The anode is fully depleted.
- The cell is not limited by electrolyte mass transport.

Benkstein *et al.* have investigated the dependence of D_0 on film porosity [37]. Providing the porosity of the film is well below the critical porosity of $\sim 76\%$ the diffusion model will be valid.

Each term in the continuity equation (2.11) will be explored in more detail in the following subsections.

2.4.1 Generation

The generation term in the continuity equation can be derived from the Beer-Lambert law for the flux of photons Φ travelling through a material multiplied by the injection efficiency [38]:

$$I = \eta_{inj} \Phi(\lambda) \exp\left[-\alpha(\lambda)\, x\right]. \tag{2.13}$$

Time-resolved single photon counting suggests that η_{inj} is only weakly dependent on n_c or on the concentration of I^- or I_3^-. Since the electron injection efficiency

is not studied in detail in this thesis the above equation is reduced to the simpler form [26, 39]

$$I = I_0(\lambda) \exp[-\alpha(\lambda) x]. \tag{2.14}$$

The number of injected electrons per unit volume per unit time between positions x and Δx must be:

$$G = \frac{\Delta I}{\Delta x} = I_0(\lambda) \frac{\exp[-\alpha(\lambda) x] - \exp[-\alpha(\lambda)(x - \Delta x)]}{\Delta x}. \tag{2.15}$$

In the limit of $\Delta x \to 0$ this becomes the derivative of equation 2.14:

$$G = \alpha(\lambda) I_0(\lambda) \exp[-\alpha(\lambda) x]. \tag{2.16}$$

Equation 2.15 can be useful if performing numerical calculations away from the limit of $x \to 0$. Note that I_0 and α will change with wavelength λ and that to model a cell in sunlight strictly speaking one would have to intergrate over the AM1.5 spectrum.

2.4.2 Recombination

The two remaining loss pathways after excited state decay, electron electrolyte and electron dye recombination, are included in the recombination term. A full model must account for the concentration of iodide [I^-] and concentration of dye awaiting regeneration [S^+]. Conventionally, recombination is simply taken to be proportional to n_c using either a recombination rate k_r or recombination time $\tau_0 = 1/k_r$ [26, 38, 27, 40].

$$R = \frac{n_c - n_{eq}}{\tau_0} = k_r (n_c - n_{eq}) \tag{2.17}$$

This is consistent with the approximations listed in section 2.4.

2.4.3 Trapping

Detailed work has shown that τ_0 and D_0 must be adjusted in the presence of traps to give an effective lifetime τ_n and effective diffusion coefficient D_n [41, 42,

38, 27, 43, 26],

$$\tau_n = \left(1 + \frac{\partial n_t}{\partial n_c}\right) \tau_0 \tag{2.18}$$

$$D_n = \left(1 + \frac{\partial n_c}{\partial n_t}\right) D_0. \tag{2.19}$$

These expressions rely on the quasi-static approximation

$$\frac{\partial n_t}{\partial t} \approx \frac{\partial n_t}{\partial n_c} \frac{\partial n_c}{\partial t} \tag{2.20}$$

which states that traps are in local equilibrium with n_c [41].

Using the zero Kelvin approximation and equation 2.7 an expression for $\partial n_t / \partial n_c$ can be found [41]

$$\frac{\partial n_t}{\partial n_c} = \frac{N_{t,0} T}{N_c T_0} n_c^{\frac{T}{T_0} - 1}. \tag{2.21}$$

The significance of equation 2.21 is that $\partial n_t / \partial n_c$ is, to a good approximation, well defined for a given fermi level and it is possible to state that [36, 42, 44, 38, 45, 43]

$$L = \sqrt{D_n \tau_n} = \sqrt{D_0 \tau_0}. \tag{2.22}$$

This is the diffusion length and its significance is explained in the next section.

2.4.4 Boundary Conditions

The rate of electron extraction at the anode-substrate interface is commonly described by an extraction rate k_{ext} which relates the current density J of electrons being extracted from the device to the concentration of electrons at the interface $n(x = 0, t)$ [21, 43]

$$\left.\frac{\partial n_c(x,t)}{\partial x}\right|_{x=0} = J = q k_{ext} n_c \left(x = 0, t\right). \tag{2.23}$$

The cell can then be described anywhere between short and open circuit by setting k_{ext} between 0 and infinity (or a large number compared to other rate constants in the continuity equation). Throughout the thesis the convention used here will be maintained where the anode-substrate interface is at $x = 0$ and continues to $x = d$ where d is the thickness of the film.

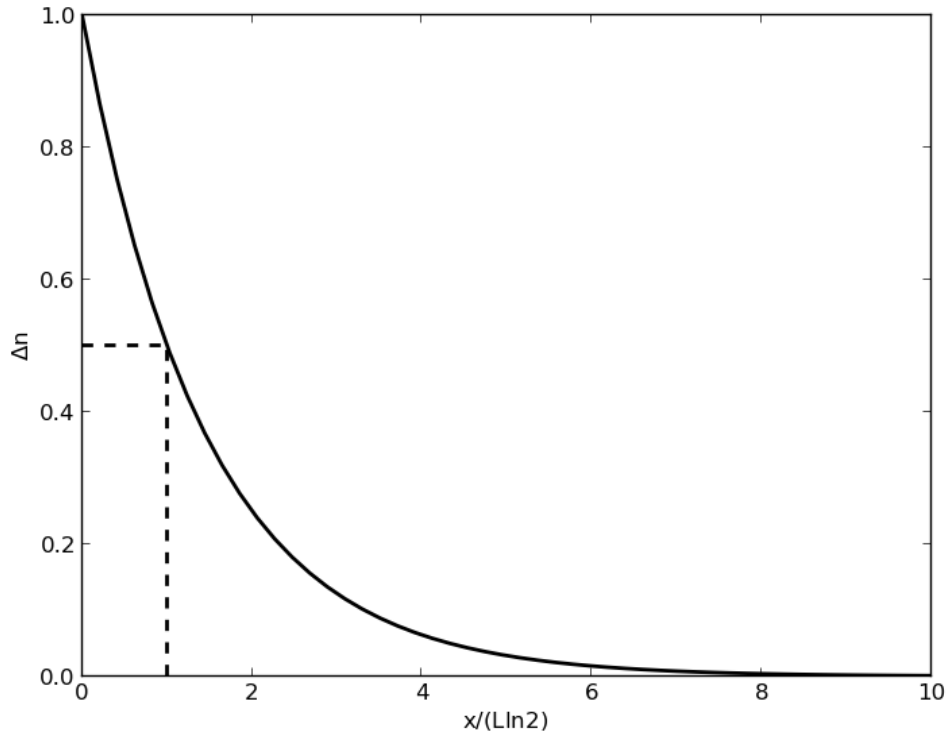

Figure 2.6: The electron concentration predicted by equation 2.28 plotted as a function of distance scaled by $L\ln(2)$. The concentration has halved over a distance $L\ln(2)$.

2.4.5 Example: The Diffusion Length

One of the most important and frequently debated results from the diffusion model is the value of the diffusion length $L = \sqrt{D_0/\tau_0}$. To illustrate the importance of L, the situation in figure 2.6 is analysed using the continuity model. At the left hand side of a film of width d, n_c is held constant by a potentiostat in the dark so that

$$n_c(0) = \text{constant}. \tag{2.24}$$

At the right hand side the film is uncontacted so there is no current at the boundary

$$\left.\frac{\partial n_c}{\partial x}\right|_{x=d} = 0. \tag{2.25}$$

In full the continuity equation is

$$\frac{\partial n_c(x,t)}{\partial t} = \alpha I_0 \exp\left[-\alpha x\right] - \frac{n_c - n_{eq}}{\tau_0} + D_0\frac{\partial^2 n_c}{\partial x^2} - \frac{\partial n_t}{\partial t} \tag{2.26}$$

where $\partial n_c/\partial t = \partial f/\partial t = 0$. If there is no generation in the film ($I_0 = 0$) it is easy to show that the change in n_c as a function of position is

$$\Delta n_c = n_c(x=0) - n_c(x) = n_c(x=0)\left[1 + \frac{e^{x/L}}{1+e^{2d/L}} - \frac{e^{-x/L}}{1+e^{-2d/L}}\right] \tag{2.27}$$

If $d >> L$ this simplifies to

$$\Delta n_c \approx n_c(x=0)\left[1 - e^{-x/L}\right]. \tag{2.28}$$

n_c decreases by $1/e$ over the length L, $1/e^2$ over the length $2L$ and so forth. Half the electrons have recombined after a distance $L\ln 2$ as illustrated by the dashed lines in figure 2.6.

Under uniform illumination through the whole film and under short circuit conditions this still holds true. For example when the boundary conditions are

$$\frac{\partial n_c}{\partial x}_{x=d} = 0, n_c(x=0) = 0 \tag{2.29}$$

$$\Delta n_c = n_c(x=0)\left[1 - \frac{e^{x/L}}{1+e^{2d/L}} - \frac{e^{-x/L}}{1+e^{-2d/L}}\right] \tag{2.30}$$

This simplifies to equation 2.28 when $d >> L$.

Chapter three explores the measurement of the diffusion length and how numerical modelling can help in its determination.

Chapter 3

A frequency dependent device model for dye-sensitized solar cells

This chapter presents a device model for simulating the frequency response of DSCs. Firstly, in section 3.1 the motivation for such a model is explored. Next, in section 3.2 frequency dependent experiments are reviewed. Section 3.3 contains the details of the frequency dependent model and the numerical analysis required to solve it. Results are presented in section 3.4.

3.1 Motivation for the device model

The standard model for dye-sensitized solar cells outlined in chapter 2 predicts that the slope of open circuit voltage plotted against $\log_{10}$ of light intensity will be 59mV per order of magnitude change in light intensity. In practice, an ideality factor m has to be introduced, where $1 < m < 3$, because it is not uncommon to see gradients as high as 120mV per decade; the reasons why are not well understood [46][47].

$$\frac{dV_{OC}}{d\log_{10} I_0} = m\frac{2.303k_BT}{q} \tag{3.1}$$

This is a major shortcoming in the understanding of DSCs and suggests that there is something fundamental about DSCs which is not completely resolved. For the rest of this thesis the following terminology is used

$$m \begin{cases} = 1 & \text{for ideal cells} \\ \neq 1 & \text{for non-ideal cells} \end{cases} \tag{3.2}$$

This non-ideal behaviour is consistent with nonlinear recombination [45, 40, 48]

$$R = \frac{(n_c - n_{eq})^{\beta}}{\tau_0 n_c^{\beta-1}} \tag{3.3}$$

where the reaction order $\beta = 1/m < 1$ is a constant. One needs to be careful to preserve the correct units of the recombination term, R. Often equation 3.4 is used in preference to equation 3.3 despite the units of τ_0 depending on β.

$$R = \frac{(n_c - n_{eq})^{\beta}}{\tau_0}. \tag{3.4}$$

The form used in equation 3.4 is used throughout the rest of the thesis in order to conform to existing conventions.

Nonlinear recombination is not the sole explanation for non-ideal behaviour and there are still inconsistencies between some experimental results. For instance, Wang and Peter measured trapped electron densities at open and short circuit as a function of incident photon flux using near IR absorbance and found that the results support first order recombination [49].

Jennings and co-workers have attributed non ideal behaviour to interactions between electrons and ions in the electrolyte manifesting as a non-Boltzmann like relationship between electron concentration and the quasi Fermi level [36]. Symbolically $m = 1/\gamma$ appears in the Boltzmann factor

$$n_c = N_c \exp\left[-\gamma \frac{E_c - {}_nE_F}{k_B T}\right]. \tag{3.5}$$

O'Regan and Durrant have proposed a third interpretation having observed a shift in the conduction band edge with open circuit voltage which was attributed

to changing surface charge on the TiO_2 pores [50].

A clear hypothesis is needed for each one of these scenarios. Numerical DSC models are a useful tool for generating such predictions since the empirical factors β, γ and m make the equations increasingly difficult to solve analytically.

There have been many numerical models published for DSCs. Cao used forward time central space finite differencing to explore the consequences of a diffusion coefficient dependent on electron concentration [51]. Ferber published a full numerical DSC model in 1998 which solved for the concentrations of electrons in the TiO_2 film and ions in the electrolyte for ideal cells where $m = 1$ [52] . Cass *et al.* used Monte Carlo simulations to simulate charge in TiO_2 grains [53].

In the last couple of years numerical models have been presented that can solve for transient and steady state properties of the cell when $m \neq 1$. Barnes *et al.* have published a full model for non-ideal cells and concluded that non-ideal behavior was required to describe laboratory cells [21] . In 2012, Anta *et al.* published numerical solutions to the continuity equation with nonlinear $m \neq 1$ recombination using shooting methods [54]. This is potentially a useful tool for analysing transient and steady state experiments on DSC since it provides solutions predicting the IV curve for non-ideal cells [54].

There is currently no model for the frequency responce of non-ideal DSCs. The main form of analysis available is the inadequate linear equivalent circuit model which is only valid if $m = 1$ [55, 56, 57]. This chapter extends the work of Anta *et al.* and Barnes *et al.* to simulate frequency dependent experiments, namely Electrochemical Impedance Spectroscopy (EIS), Intensity Modulated Voltage Spectroscopy (IMVS) and Intensity Modulated Photocurrent Spectroscopy (IMPS) when $m \neq 1$. The methods used by Anta *et al.* and Barnes *et al.* are not reviewed here because they are largely the same as those used in the rest of this chapter. This work is an obvious extension to the available numerical tools since these frequency dependent experiments are some of the most common tools for characterizing DSCs and they are not covered by any of the present models.

The next section reviews the three principle frequency domain techniques, EIS, IMVS and IMPS.

3.2 Frequency domain characterization techniques

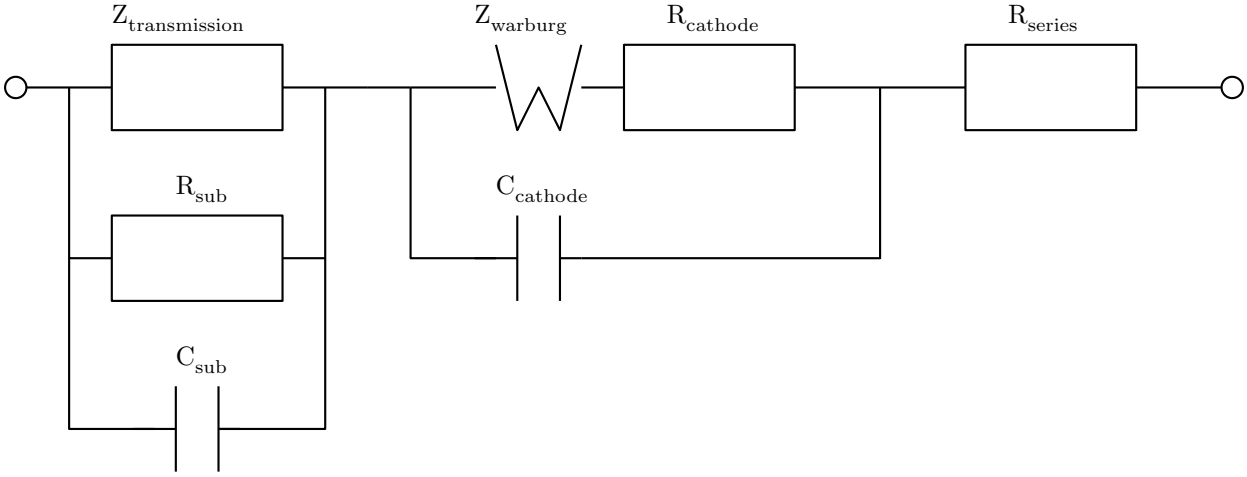

Figure 3.1: The equivalent circuit for a dye-sensitized solar cell [1, 58].

Before introducing any detailed mathematics the three principle frequency domain techniques will be introduced. One can either perturb the cell using time varying illumination (intensity modulated spectroscopy) or one can perturb the cell by applying a time varying potential or current at the electrode (electrochemical impedance spectroscopy). Intensity modulated methods are further divided into two subcategories, depending on if the resulting photovoltage or photocurrent is measured. These are intensity modulated photovoltage spectroscopy (IMVS) and intensity modulated photocurrent spectroscopy (IMPS) respectively.

Throughout this chapter it is important to remember that DSCs are complicated objects with a substrate, contacts and interfaces which will all respond differently when driven at different frequencies. Figure 3.1 is an equivalent circuit of a DSC [1, 58]. Both the substrate and the cathode have a resistance and capacitance which will have their own time constants. The whole device also has an additional series resistance. The TiO_2 film is represented by the transmission impedance $Z_{transmission}$ and electrolyte by the Warburg impedance $Z_{Warburg}$. $Z_{Warburg}$ is an element that models diffusion to a large planar electrode, at high frequencies it produces a $\pi/4$ phase difference between the voltage and the current. $Z_{transmission}$ will be investigated in this chapter, if one wishes to reproduce the trends given by a real whole cell then one must insert $Z_{transmission}$ back into the equivalent circuit in figure 3.1, providing that the other elements are sufficiently understood.

3.2.1 IMVS experiments

Figure 3.2 (top) shows a basic outline of an IMVS setup [44, 59]. The cell is illuminated by an LED driven by a function generator with some steady state part $I_{0,ss}$ which keeps the cell under normal operating conditions and a harmonic time dependent part $I_0 \exp(i\omega t)$ which must be sufficiently small to generate a linear response from the cell. Conventionally, the cell is held at open circuit, although this is not strictly a requirement but it is the case for the vast majority of experiments [57]. Strictly speaking, the cell can be galvanostatically controlled at any point on the IV curve [57]. The amplitude of the time dependent potential difference between the cell contacts is recorded and the phase of the potential difference relative to the signal driving the LED is also recorded over a range of different driving frequencies ω [44, 59].

Conventionally, the data is plotted on the complex plane by considering the potential difference as a complex number with a real part $\Re(V(\omega))$ and an imaginary part $\Im(V(\omega))$ rather than as a phasor with an amplitude $V_0(\omega)$ and phase $\phi(\omega)$ [57]. These are related in the usual way,

$$V_0(\omega) = \sqrt{\Re(V(\omega))^2 + \Im(V(\omega))^2} \tag{3.6}$$

and

$$\phi(\omega) = \arctan \frac{\Im(\omega)}{\Re(\omega)}. \tag{3.7}$$

At the angular frequency ω_{rec} there is a resonance. This is usually identified by a minimum in the imaginary part of the signal. An example is shown in figure 3.2 (bottom). It is also useful to note that an IMVS experiment driven at ω_{rec} will have a phase difference of $\pi/4$ rad (or equivalently $\Re\left[V\left(\omega\right)\right] = \Im\left[V\left(\omega\right)\right]$) between the driving signal and the resulting signal which is typical of resonances in general. It is straightforward to show that

$$\omega_{rec} = \tau_n^{-1} \text{ if } m = 1 \text{ and } N_{t,0} = 0. \tag{3.8}$$

It should be noted that figure 3.2 only shows the response for $\mathrm{Z}_{\mathrm{transmission}}$ in figure 3.1, it doesn't include the substrate or cathode impedances.

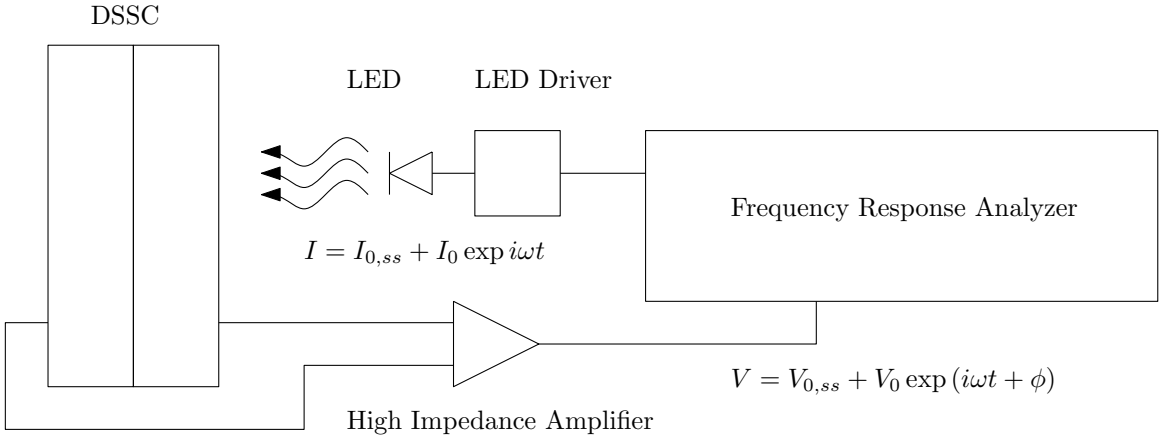

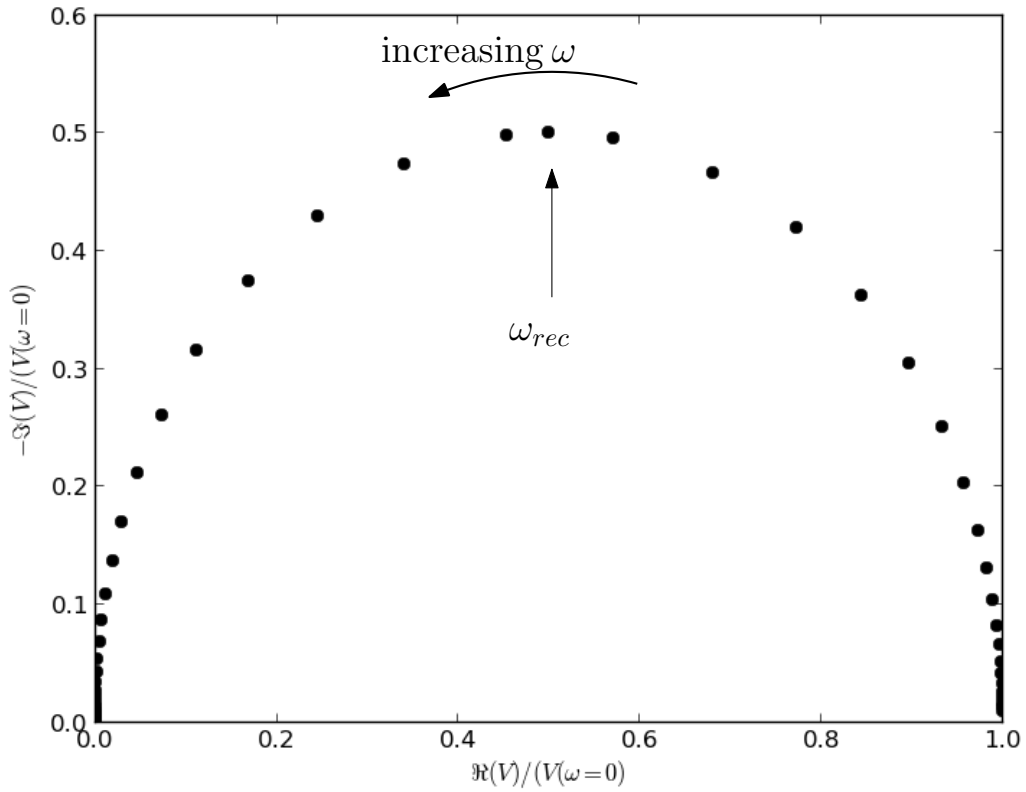

Figure 3.2: Setup for an IMVS experiment (top) and an illustration of a typical IMVS result with the resonant frequency marked (bottom).

3.2.2 IMPS experiments

IMPS experiments are similar to IMVS experiments except that the cell is under short circuit conditions (more strictly potentiostatic conditions) [44, 59]. The cell is illuminated in exactly the same way as the IMVS experiments described in section 3.2.1. Unlike IMVS experiments it is the amplitude and phase of the photocurrent which is measured against frequency rather than the photovoltage. Figure 3.3 (top) illustrates the experimental setup.

Interpreting IMPS experiments is not so straight forward, even for ideal DSCs. Equation 2.21 becomes highly nonlinear near short circuit conditions complicating the interpretation of both D_n and τ_n. Basic modelling shows that when the imaginary part of the photocurrent is minimised [43]

$$\omega = \omega_{tr} \propto \frac{D_0}{d^2} \text{ if } m = 1 \text{ and } N_{t,0} = 0. \tag{3.9}$$

At high frequencies the phase difference between the illumination and the resulting photocurrent becomes $\pi/4$ rad. This is indicative of unrestricted diffusion to a planar surface (Warburg behaviour). ω_{tr} then marks the transition from Warburg behaviour to restricted behavior hence equation 3.9. Figure 3.3 only shows the response from $Z_{\text{transmission}}$. Since the cell is under short circuit conditions the quasi Fermi level will not be constant across the device. This clearly has implications when $\beta \neq 1$ since the effective carrier lifetime τ_n is not constant through the TiO_2 film.

3.2.3 Measuring L_0 using IMVS/IMPS

For ideal cells the diffusion length can be measured if $m = 1$. Equations 3.8 and 3.9 are only valid if there are no traps however equations 2.18 and 2.19 show that L_0 can still be calculated since

$$L_0 \propto \frac{\omega_{tr}}{\omega_{rec}} \tag{3.10}$$

and trapping effects cancel providing that the steady state quasi-Fermi level ${}_nE_F$ is the same at all points during both the IMPS and IMVS experiments [38].

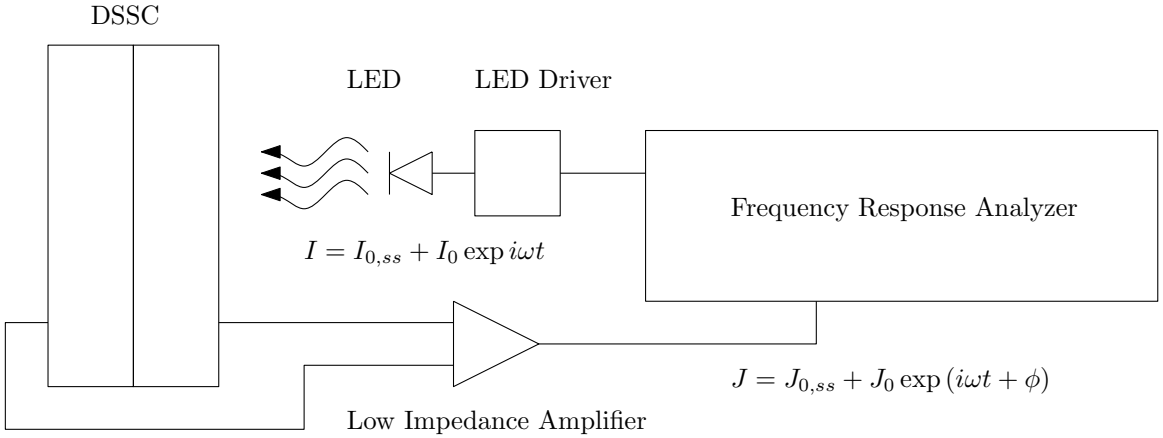

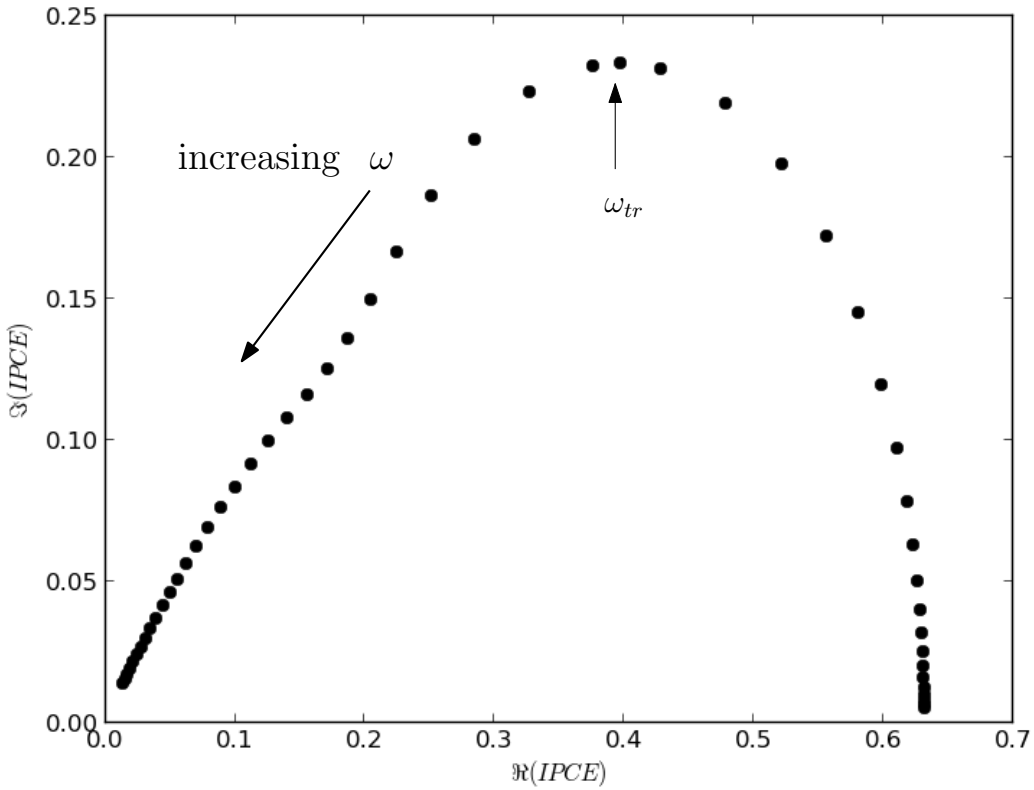

Figure 3.3: Setup for an IMPS experiment (top) and an illustration of a typical IMPS result with the resonant frequency marked (bottom) where illumination is through the substrate.

3.2.4 EIS experiments

Figure 3.2 shows the setup (top) and typical results (bottom) for an EIS experiment [60, 61, 58, 1]. The light source is now constant. The cell is driven with a time dependent potential difference across the terminals

$$V = V_{0,ss} + V_0 \exp(i\omega t). \tag{3.11}$$

The amplitude of the resulting time dependent current density J_0 and the phase difference ϕ between the applied potential and the resulting current are recorded as a function of frequency where

$$J = J_{0,ss} + J_0 \exp(i\omega t + \phi). \tag{3.12}$$

The impedance is given by the derivative

$$Z = \frac{1}{A}\frac{dV_0}{dJ_0} \tag{3.13}$$

where A is the area of the cell is plotted on the complex plane. Historically, the interpretation of EIS experiments has differed significantly from IMPS/IMVS experiments since there is a preference for using equivalent circuits rather than the continuity equation [61, 57]. The transmission line method is presented here. Later it will be demonstrated that the continuity equation approach is equally valid.

The standard equivalent circuit used for fitting EIS results is shown in figure 3.5. It is the same as the equivalent circuit for an infinitesimal section of a transmission line dx. $\mathrm{r_{tr}}$ is the transmission resistance per incremental distance dx. $\mathrm{r_{ct}}$ is the charge transfer resistance per incremental distance dx and $\mathrm{c_{\mu}}$ is the chemical capacitance per incremental distance dx.

The potential difference ΔV along the transmission line over a distance Δx (as opposed to the potential difference between the two ports) is

$$\Delta V = V(x + \Delta x) - V(x) = -r_{tr}\Delta x\ I(x) \tag{3.14}$$

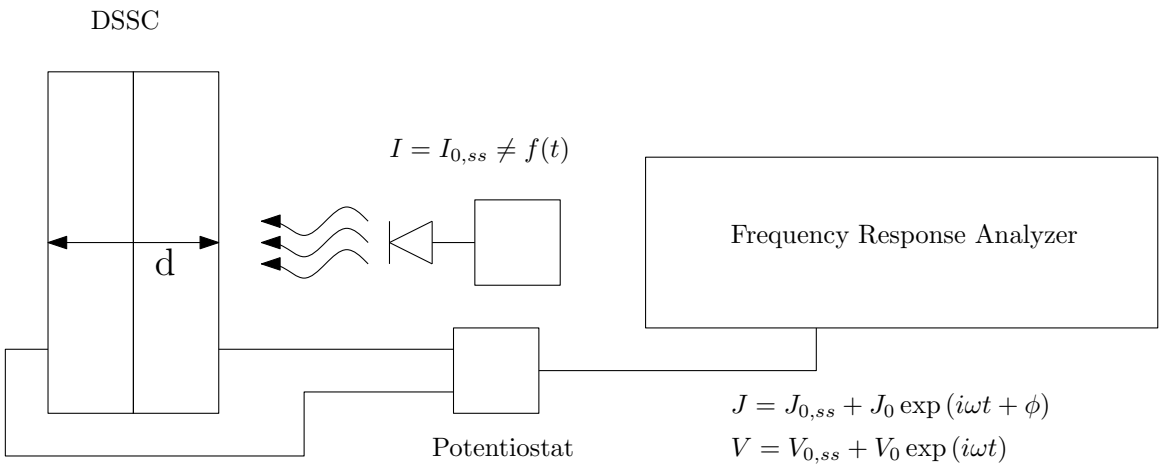

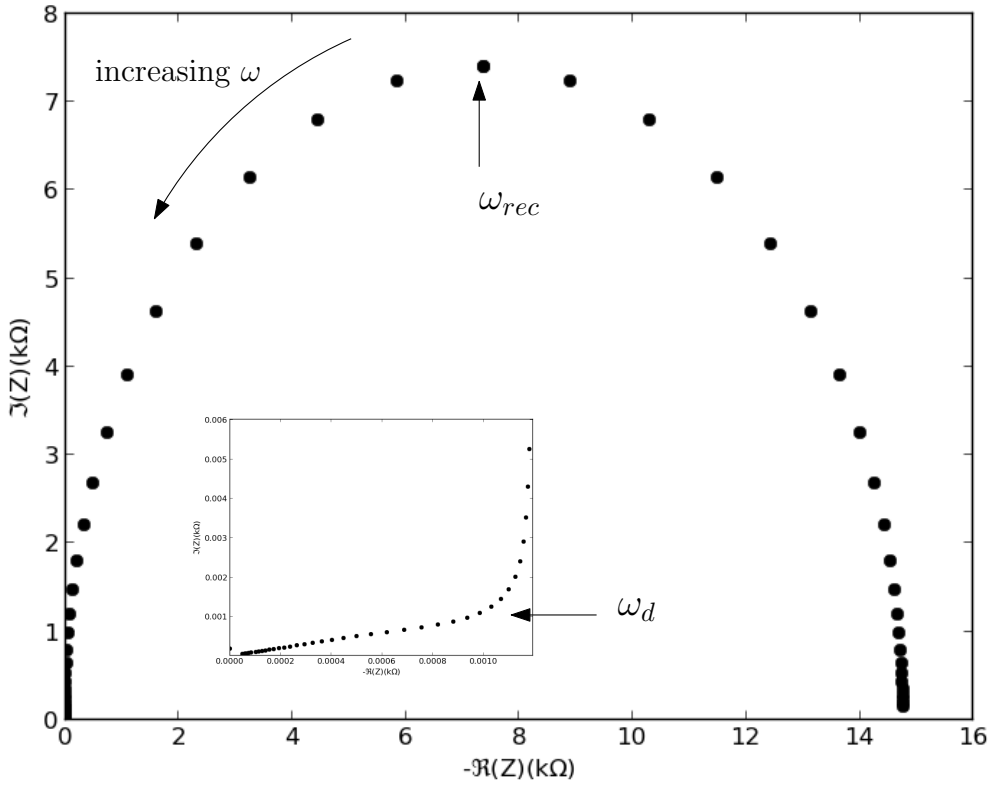

Figure 3.4: Setup for an EIS experiment (top) and an illustration of a typical EIS result with the resonant frequency marked (if $m = 1$) and an inset showing the high frequency response (bottom).

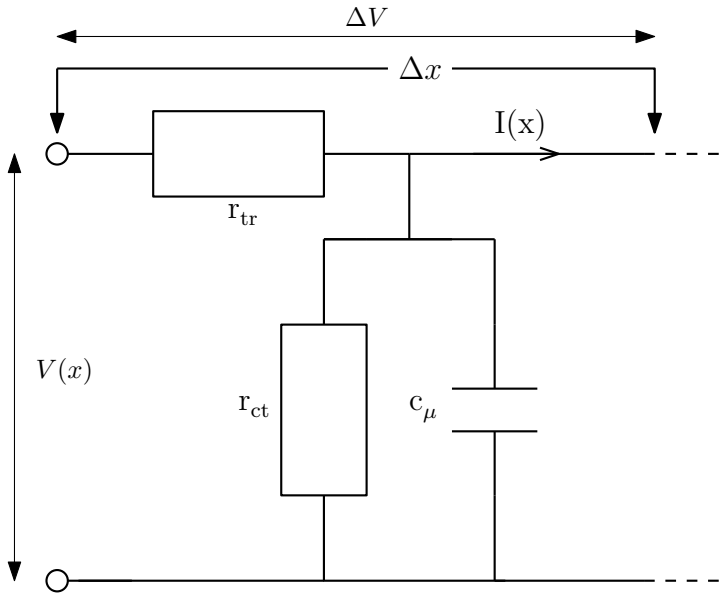

Figure 3.5: The elementary unit of the transmission line model.

and the change in current along the transmission line is

$$\Delta I = I\left(x + \Delta x\right) - I\left(x\right) = \Delta x \left(\frac{1}{r_{ct}} + i\omega c_{\mu}\right) V(x) \tag{3.15}$$

In the limit of $\Delta x \to 0$ the two equations 3.14 and 3.15 become

$$\frac{\partial V(x)}{\partial x} = -r_{tr} I(x) \tag{3.16}$$

and

$$\frac{\partial I(x)}{\partial x} = -\left(\frac{1}{r_{ct}} + i\omega C\right) V(x) \tag{3.17}$$

Combining the two equations, a single expression for the potential difference as a function of position is reached for a given angular frequency ω.

$$\frac{d^2 V(x)}{dx^2} = -\alpha\left(\omega\right)^2 V(x) \tag{3.18}$$

where

$$\alpha\left(\omega\right)^2 = \mathrm{r_{tr}}\left(\mathrm{r_{ct}}^{-1} + i\omega \mathrm{c}_{\mu}\right) \tag{3.19}$$

and

$$I\left(x\right) = \frac{1}{\mathrm{r_{tr}}} \frac{\partial V}{\partial x}. \tag{3.20}$$

Equation 3.18 will be referred to as the transmission line equation.

A long chain of such circuit elements will produce the same impedance as a function of frequency as $Z_{transmission}$ which is shown in figure 3.4 (bottom). r_{tr}, r_{ct} and c_μ can be found by performing a curve fit to DSC impedance using the transmission line model. In the next section the continuity equation is used to arrive at the same result as the telegraph equation showing that the two approaches of continuity equations and equivalent circuits are really the same. Unlike equivalent circuits, it will be relatively easy to extend the continuity equation to describe IMVS/IMPS experiments and to describe nonlinear recombination where $\beta \neq 1$. Generation through illumination, nonlinear recombination and cell non-ideality all become rather abstract concepts when applied to the transmission line model.

3.3 The frequency domain model

In this section the continuity equation is taken as a starting point and used to derive a differential equation for small time dependent first order harmonic perturbations. The equation has the same form as the telegraph equation used for modelling the transmission line in figure 3.5, as an aside the equivalence of the equivalent circuit and continuity equation methods is demonstrated. At all points care is taken to make sure that the expressions are valid for the general case for non-ideal cells.

3.3.1 Derivation of the telegraph equation from the continuity equation

Starting with the continuity equation (2.11) n_c is substituted by a concentration with a small first order time dependent part.

$$n_c = n_{c,ss} + \delta n_c \exp(i\omega t) \tag{3.21}$$

where δn_c is the amplitude of the perturbed conduction band electron concentration with frequency ω. Likewise, δI_0 is the perturbed photon flux (which may be

zero for some techniques)

$$I_0 = I_{0,ss} + \delta I_0 \exp(i\omega t) \tag{3.22}$$

and consequently the concentration of trapped electrons n_t goes as

$$n_t = n_{t,ss} + \delta n_t \exp(i\omega t) \tag{3.23}$$

provided that δI_0, δn_c and δn_t are sufficiently small.

By substituting equations 3.21, 3.22 and 3.23 into equation 2.11 and only including first order time dependent terms one finds that

$$\frac{\partial^2 \delta n_c}{\partial x^2} + \frac{\alpha \delta I_0 \exp(-\alpha x)}{D_0} - \mu(x,\omega)^2 \delta n_c = 0. \tag{3.24}$$

where $\mu(x,\omega)^2$ is the recombination / trapping term

$$\mu(x,\omega)^2 = \frac{i\omega \left(1 + \frac{\partial n_t}{\partial n_c}\right) + \tau_0^{-1} \beta (n_{ss}(x) - n_{eq})^{\beta - 1}}{D_0} \tag{3.25}$$

where the following approximation is valid for small perturbations

$$(n_c + \delta n_c + n_{eq})^\beta \approx (n_c + \delta n_c)^\beta \approx n_c^\beta + \beta n_c^{\beta-1} \delta n_c. \tag{3.26}$$

Note this equation is also the same form as the telegraph equation 3.18. If the quasi-static approximation holds and if n_c is constant across the device then the trapping term amounts to a frequency shift (see equation 2.21).

δn_c is complex and represents the amplitude and the phase of the perturbed n_c (a phasor) with amplitude

$$r = \sqrt{(\Re(n_c)^2 + \Im(n_c)^2))} \tag{3.27}$$

and phase

$$\theta = \arctan \frac{\Im(n_c)}{\Re(n_c)}. \tag{3.28}$$

3.3.2 Comparing the continuity equation with equivalent circuits

If $\beta = 1$ the transmission line equation (or telegraph equation) 3.18 has exactly the same form as the frequency dependent continuity equation 3.64. Comparing the two expressions

$$\alpha(\omega)^2 = \mathrm{r_{tr}}\left(\mathrm{r_{ct}} + i\omega \mathrm{c}_\mu\right) \text{ and } \mu(\omega)^2 = \frac{\tau_0^{-1} + i\omega\left(1 + \partial n_t/\partial n_c\right)}{D_0} \tag{3.29}$$

By solving the telegraph equation one can eventually show that for the special case where $\beta = 1$ and $T = T_0$.

$$\mathrm{r_{tr}} = \frac{k_B T}{q^2 A n_c D_0}, \tag{3.30}$$

$$\mathrm{r_{ct}} = \frac{k_B T \tau_0}{A q^2 n_c} \tag{3.31}$$

and

$$\mathrm{c}_\mu = \left(1 + \frac{\partial n_t}{\partial n_c}\right) \frac{A q^2 n_c}{k_B T}. \tag{3.32}$$

Both models using transmission lines or the continuity equation are fundamentally the same. It can be useful to use equivalent circuits because one can use well understood physics to interpret $\mathrm{Z_{transmission}}$. It can be useful to use continuity equations when the equivalent circuit analogy breaks down so one can deal with microscopic parameters with physical meaning.

3.3.3 Numerical Methods

To solve the transmission line equation numerically, δn_c has to be separated into real and imaginary parts where

$$\delta n_c(x) = \Re\delta n_c(x) + \sqrt{-1} \times \Im\delta n_c(x). \tag{3.33}$$

Substituting this into the telegraph equation for a constant angular frequency ω

and collecting real and imaginary terms it can be seen that the second spatial derivative of the real part is given by

$$\frac{\partial^2 \Re\delta n_c(x)}{\partial x^2} = \frac{\beta\left(n_{ss}\left(x\right)-n_{eq}\right)^{\beta-1}}{D_0\tau_0}\Re\delta n_c(x) - \frac{\omega\left(1+\frac{\partial n_t}{\partial n_c}\right)}{D_0}\Im\delta n_c(x) - \frac{\alpha\delta I_0\exp\left(-\alpha x\right)}{D_0} \quad (3.34)$$

and the imaginary part

$$\frac{\partial^2 \Im\delta n_c(x)}{\partial x^2} = \frac{\beta\left(n_{ss}\left(x\right)-n_{eq}\right)^{\beta-1}}{D_0\tau_0}\Im\delta n_c(x) + \frac{\omega\left(1+\frac{\partial n_t}{\partial n_c}\right)}{D_0}\Re\delta n_c(x) - \frac{\alpha\delta I_0\exp\left(-\alpha x\right)}{D_0}. \quad (3.35)$$

The background or steady state electron concentration must be known and can be calculated using the solution to the equation

$$0 = \alpha I_0\exp\left[-\alpha x\right] - \frac{\left(n_{c,ss}\left(x\right)-n_{eq}\right)^{\beta}}{\tau_0} + D_0\frac{d^2 n_{c,ss}\left(x\right)}{dx^2} \quad (3.36)$$

with boundary conditions

$$\left.\frac{dn_{c,ss}}{dx}\right|_{x=0} = k_{ext}n_{c,ss}\left(x=0\right) \quad (3.37)$$

and

$$\left.\frac{dn_{c,ss}}{dx}\right|_{x=d} = 0 \quad (3.38)$$

where k_{ext} depends on the bias using the method published by Anta and co-workers [54].

Equations 3.34 and 3.35 must then be further split into four first order equations.

$$\Re\delta n_c'(x) = \frac{d\Re\delta n_c(x)}{dx} \quad (3.39)$$

$$\Im\delta n_c'(x) = \frac{d\Im\delta n_c(x)}{dx} \quad (3.40)$$

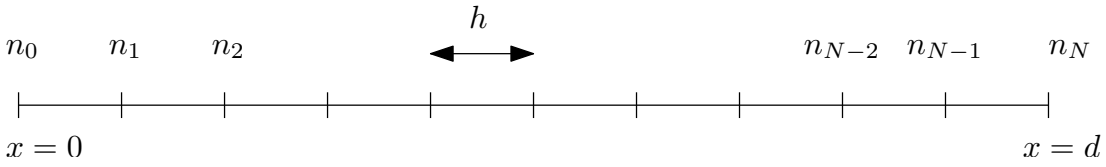

Figure 3.6: Representation of the N discrete points separated by distance h used to represent solutions to the telegraph equation solved through shooting methods.

$$\frac{\partial \Re\delta n_c'(x)}{\partial x} = \frac{\beta\left(n_{ss}(x) - n_{eq}\right)^{\beta-1}}{D_0\tau_0}\Re\delta n_c(x) - \frac{\omega\left(1+\frac{\partial n_t}{\partial n_c}\right)}{D_0}\Im\delta n_c(x) - \frac{\alpha\delta I_0\exp\left(-\alpha x\right)}{D_0} \quad (3.41)$$

$$\frac{\partial \Im\delta n_c'(x)}{\partial x} = \frac{\beta\left(n_{ss}(x) - n_{eq}\right)^{\beta-1}}{D_0\tau_0}\Im\delta n_c(x) + \frac{\omega\left(1+\frac{\partial n_t}{\partial n_c}\right)}{D_0}\Re\delta n_c(x) - \frac{\alpha\delta I_0\exp\left(-\alpha x\right)}{D_0} \quad (3.42)$$

Next, these four equations are solved as initial value problems on a discrete grid of points between $x = 0$ and $x = d$ as shown in figure 3.6. If $\Re\delta n_c(x=0)$, $\Im\delta n_c(x=0)$, $\Re\delta n_c'(x=0)$, $\Im\delta n_c'(x=0)$ are all known then the system of four equations can be integrated through Euler integration and δn_c can be approximated at each point $x_{0,1,2..N}$ in figure 3.6.

Explicitly, the steps are as follows: The second spatial derivative of the real and imaginary parts of δn_c can be calculated directly from δn_c using equations 3.41 and 3.42.

$$\frac{d\Re\delta n_c'(x=0)}{dx} = f\left(\Re\delta n_c(x=0), \Im\delta n_c(x=0)\right) \quad (3.43)$$

$$\frac{d\Im\delta n_c'(x=0)}{dx} = f\left(\Re\delta n_c(x=0), \Im\delta n_c(x=0)\right) \quad (3.44)$$

then if h is sufficiently small to disregard higher order terms the first spatial derivative of $\delta n_c(x=h)$ can be approximated.

$$\Re\delta n_c'(x=h) = \Re\delta n_c'(x=0) + h\frac{d\Re\delta n_c'(x=0)}{dx} \quad (3.45)$$

$$\Im\delta n_c'(x=h) = \Im\delta n_c'(x=0) + h\frac{d\Im\delta n_c'(x=0)}{dx} \quad (3.46)$$

Finally, $\delta n_c(x = h)$ itself can be approximated.

$$\Re\delta n_c(x = h) = \Re\delta n_c(x = 0) + h\Re\delta n_c'(x = 0) \tag{3.47}$$

$$\Im\delta n_c(x = h) = \Im\delta n_c(x = 0) + h\Im\delta n_c'(x = 0) \tag{3.48}$$

This process can be repeated to find $\delta n_c(2h)$, $\delta n_c(3h)...\delta n_c(Nh)$. For all of the studies in this thesis a value of $h = 20$nm was used and was more than adequate.

There are eight boundary conditions; eight first order differential equations each with a boundary condition. In this example, the value at the left hand side was known for each equation however this need not be the case. As long as the value at one boundary is known it is possible to solve the system using variational methods. If the value of one of the equations at the left hand side is not known a trial value must be used. As before, the solution is found by integrating the four equations between 0 and d. If a boundary condition at the right hand side is not satisfied then the trial value must be adjusted and another attempt is made to solve the system until all boundary conditions are satisfied. This is a root finding problem and the root finder fsolve, from the scientific python optimization package, was used.

Avoiding negative square roots

When trying to solve for n_c in the case where recombination is non-linear and $\beta < 1$ a poor initial guess can lead to complications. If the guess is poor the integration of the continuity equation may proceed into a region where $n_c < 0$. This is not normally a problem if $\beta = 1$, but if $\beta < 1$ the recombination term becomes imaginary and the root finding algorithm cannot proceed in a useful or meaningful way.

A simple remedy to this problem is to solve the linear problem where $\beta = 1$ and then use this solution as an initial guess to the similar problem $\beta = 1 - \delta$ where delta is a small number. Repeating this process one can solve the problem where $\beta = 1 - 2\delta, 1 - 3\delta$ etc. until the desired β is reached. In practice $\delta = 0.003$ was used. This is not a computationally expensive process so the most efficient value for δ was not investigated.

3.4 Solutions to the frequency domain model

All of the frequency domain techniques can be described by second order boundary value problems and are easily solved by the methods described in the previous section. In the following three subsections the boundary value problems for EIS, IMVS and IMPS are defined and solutions are presented to show the influence of nonlinearity on the solution. For each of the three techniques the solution for an ideal cell is presented to demonstrate that the model is working. Then for each of the three techniques the relevant characteristic frequencies (ω_{tr} or ω_d and ω_{rec}) are shown at different points along the JV curve for ideal and non-ideal cells. The results are presented without any trap states in order to show purely the influence of ideality factor m on the results. When measuring L_0 trapping effects will cancel as was the case in section 3.2.3, this will be proved for EIS experiments in section 3.5 where results with full trapping are presented.

3.4.1 Electrochemical impedance spectroscopy (EIS)

To simulate EIS experiments one needs to solve the telegraph equation

$$\frac{d^2\delta n_c}{dx^2} - \mu^2(x)\delta n_c = 0 \tag{3.49}$$

at a fixed frequency ω. $\delta I_0 = 0$ since the cell is under constant steady illumination.

$$\mu(x,\omega)^2 = \frac{i\omega\left(1+\frac{\partial n_t}{\partial n_c}\right) + \tau_0^{-1}\beta(n_{ss}(x)-n_{eq})^{\beta-1}}{D_0} \tag{3.50}$$

The voltage perturbation is applied at the left hand boundary so by definition the phase of δn_c is zero. The magnitude of δn_c will not change the impedance so it is usually set to 1 in practise.

$$\Re\left(\delta n_c(x=0)\right) = \text{constant} \tag{3.51}$$

$$\Im\left(\delta n_c(x=0)\right) = 0 \tag{3.52}$$

and (as is always the case) for a film of thickness d

$$\Re\left(\left.\frac{dn_c}{dx}\right|_{x=d}\right) = 0. \tag{3.53}$$

$$\Im\left(\left.\frac{dn_c}{dx}\right|_{x=d}\right) = 0. \tag{3.54}$$

The impedance is given by the ratio of the amplitudes of the voltage and current at the contact

$$Z(\omega) = \frac{\delta V(\omega)}{\delta I(\omega)} = \frac{k_B T \frac{\delta n_c(x=0)}{n_{ss}(x=0)}}{qAD_0 \left.\frac{d\delta n_c(x,\omega)}{dx}\right|_{x=0}}. \tag{3.55}$$

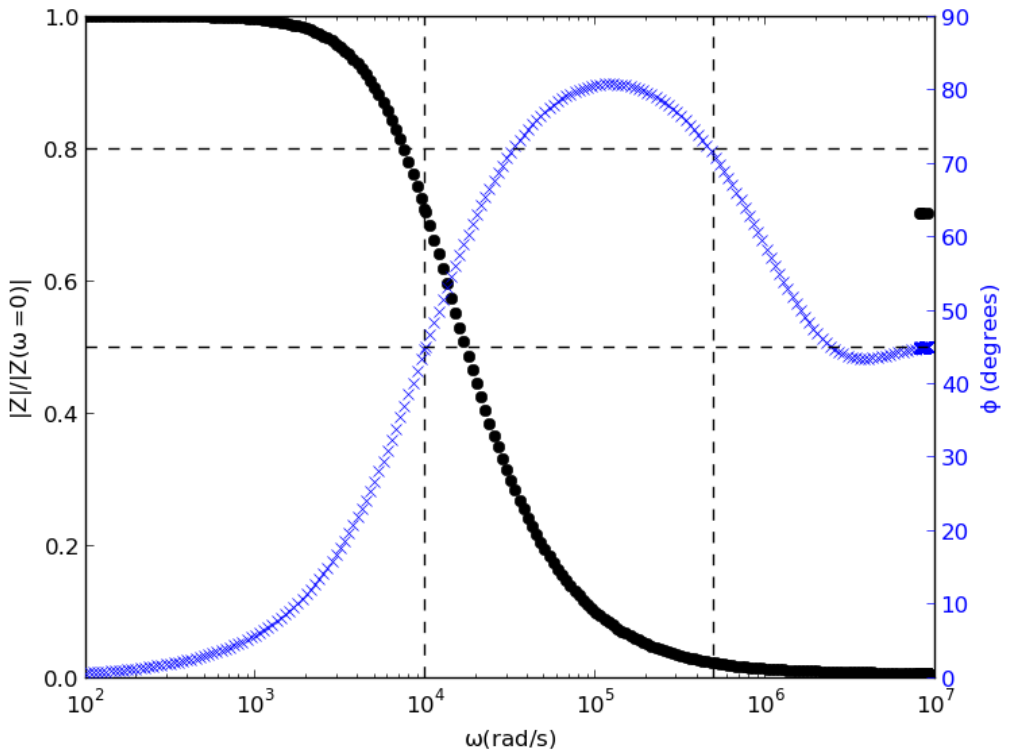

Figure 3.7: EIS Bode plot showing the magnitude (circles) and phase (crosses) of the frequency response. The two horizontal lines are at exactly 45° and 72°. The vertical lines are at τ_0^{-1} and D_0/d^2. $\beta = 1$, $d = 10\mu$m, $\tau_0^{-1} = 10^4$s, $D_0 = 0.5$cm^{-2}s^{-1}, $N_{t,0} = 0$ cm^{-3}, $N_c = 1 \times 10^{22}$ cm^{-3}. The x-axis terminates at ω_d.

Figure 3.7 shows an example of a solution for the linear case. Rather than plotting the results on the complex plane (normally seen in the literature) the plot is a Bode plot so that it is easy to see the solution as a function of frequency. The minimum in the complex plane when $\omega = \tau_0^{-1}$ is now signified by a 45° phase in

the impedance. This is easily visible in the plot and indicates that the model is working well. At high frequencies the phase on the impedance returns to exactly 45° and will remain so as $\omega \to \infty$. In figure 3.7 the phase will remain at exactly 45° beyond the high frequency limit of the x-axis however once the 45° limit is reached the simulation terminates since both the real and imaginary parts of the impedance approach zero and this will eventually lead to a floating point underflow. The characteristic frequency ω_d can be viewed as the point where the phase departs from 45° if one starts at the high frequency limit and decreases the frequency.

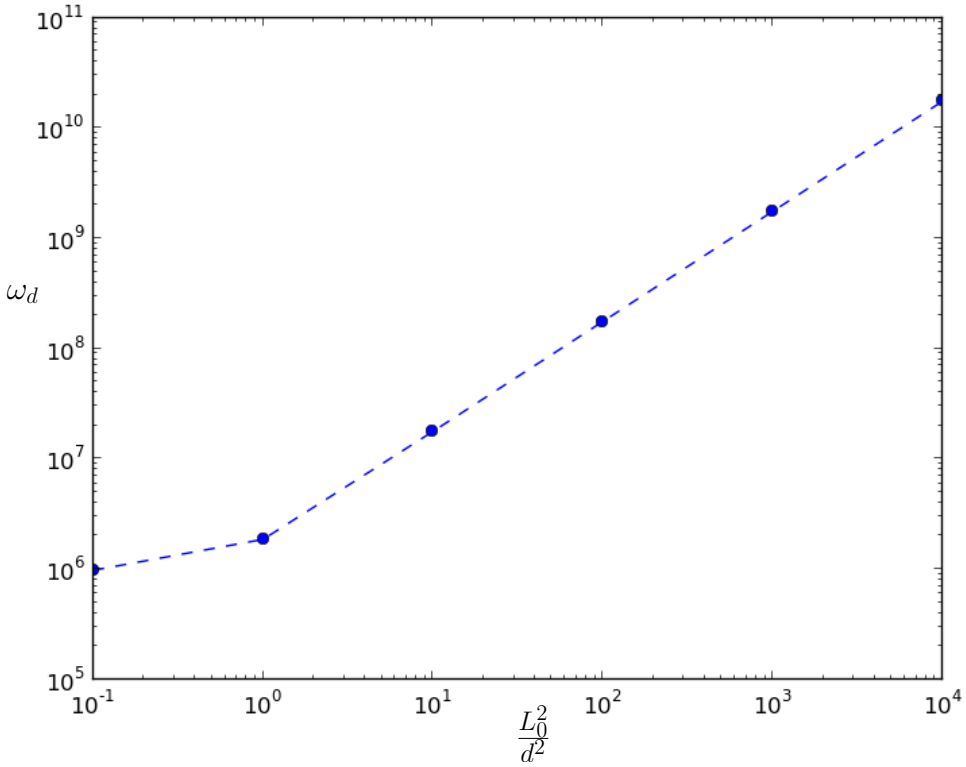

Figure 3.8: Relationship between ω_d and D_0 in the absence of trapping where $L_0^2 = D_0\tau_0$. D_0 was varied while τ_0 and d were kept constant. $\beta = 1$, $d = 10\mu$m, $\tau_0^{-1} = 10^4$s, $N_{t,0} = 0$ cm^{-3}, $N_c = 1 \times 10^{22}$ cm^{-3}.

Figure 3.8 shows that in the absence of trapping D_0 is proportional to ω_d if L is longer than the film thickness d

$$\omega_d \propto \frac{D_0}{d^2} \text{ if } L > d \text{ and } N_{t,0} = 0. \tag{3.56}$$

This is consistent with the equivalent circuit model [56]. If L_0/d becomes small then this interpretation breaks down. Essentially this is because facets used to

identify the two critical frequencies start to overlap and become convoluted as the characteristic times for transport and recombination becomes similar. In this case the model would need to be fitted to the impedance spectra in order to extract L.

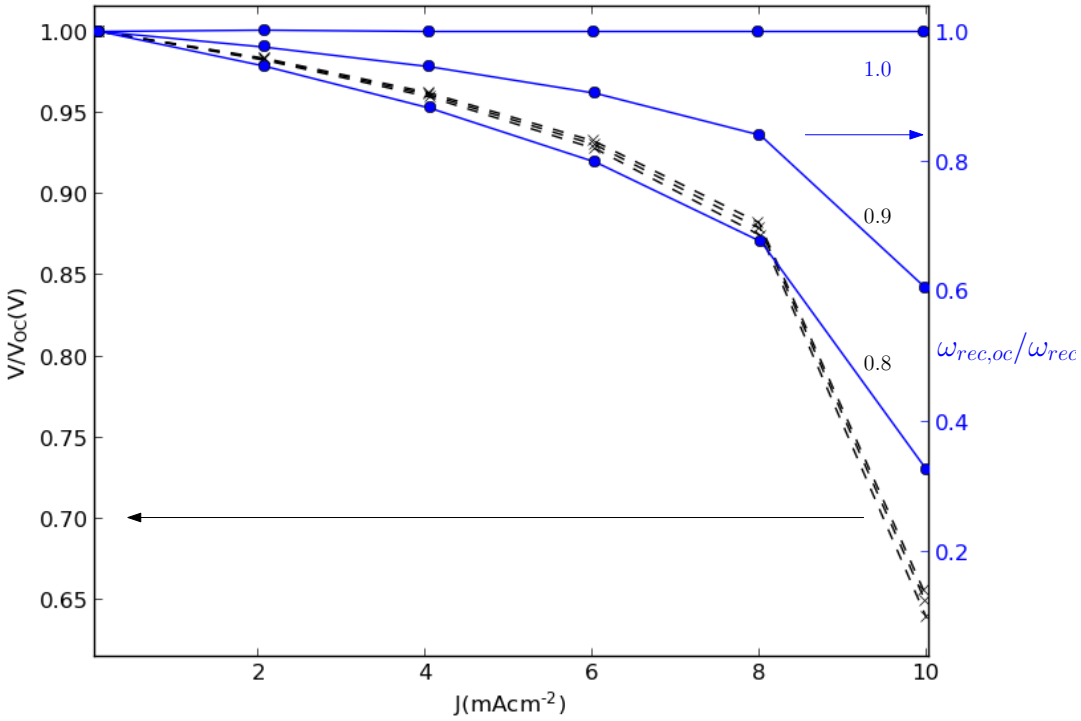

Figure 3.9: Cell bias (crosses) and ω_{rec} (circles) from simulated EIS experiments where V_{OC} and $\omega_{rec,oc}$ are the respective open circuit values. $d = 10\mu\text{m}$, $\tau_0 = 10^{-4}\text{s}$, $D_0 = 0.5\text{cm}^2\text{s}^{-1}$, $N_{t,0} = 0\ \text{cm}^{-3}$, $N_c = 1 \times 10^{22}\ \text{cm}^{-3}$, $\alpha = 1 \times 10^3\text{cm}^{-1}$, $I_0 = 10^{17}\text{cm}^{-2}\text{s}^{-1}$. $\beta = 1.0, 0.9, 0.8$.

Figure 3.9 shows the change in ω_{rec} with respect to position on the IV curve. As β becomes smaller ω_{rec} diverges increasingly from its open circuit value and becomes more sensitive to $n\,(x)$. The figure suggests that although ω_{rec} diverges significantly from its open circuit value it is unlikely to vary by more than an order of magnitude even under extreme conditions (near short circuit, high non-linearity). The $\beta = 1$ solution is consistent with the equivalent circuit model result where [56]

$$\omega_{rec} = \tau_n^{-1} \text{ if } N_{t,0} = 0 \text{ and } m = 1. \tag{3.57}$$

Note that this implies that

$$\omega_d/\omega_{rec} \propto L_0 \text{ if } \beta = 1. \text{ and } L > d \tag{3.58}$$

in the presence of traps and as such curve fitting is not strictly necessary in order to extract L_0 for ideal cells.

3.4.2 Intensity Modulated Photovoltage Spectroscopy (IMVS)

During Intensity Modulated Photovoltage Spectroscopy (IMVS) the cell is held under galvanostatic (constant current) conditions and subjected to a modulated light intensity. Now the telegraph equation has to include the generation term

$$\frac{\partial^2 \delta n_c}{\partial x^2} + \frac{\alpha \delta I_0 \exp(-\alpha x)}{D_0} - \mu^2(x,\omega)\delta n_c = 0. \tag{3.59}$$

and

$$\mu(x,\omega)^2 = \frac{i\omega\left(1+\frac{\partial n_t}{\partial n_c}\right) + \tau_0^{-1}\beta(n_{ss}(x)-n_{eq})^{\beta-1}}{D_0}. \tag{3.60}$$

Under galvanostatic conditions

$$\Re\left(\frac{d\delta n_c}{dx}_{x=0}\right) = \Re\left(\frac{d\delta n_c}{dx}_{x=d}\right) = 0. \tag{3.61}$$

and

$$\Im\left(\frac{d\delta n_c}{dx}_{x=0}\right) = \Im\left(\frac{d\delta n_c}{dx}_{x=d}\right) = 0. \tag{3.62}$$

This gives the IMVS response with zero phase at low frequencies which is given by $\delta n_c(x=0)$.

$\delta V/\delta V(\omega=0)$ is plotted in figure 3.10 at open circuit. τ_n is given by

$$\tau_n = \frac{1}{\omega_{rec}}. \tag{3.63}$$

Figure 3.11 shows the change in ω_{rec} with respect to open circuit voltage. The figure is nearly exactly the same as figure 3.9. This reflects the deep similarities between the two experiments. They are essentially the same except in EIS the stimulus is provided at the electrode and in IMVS the stimulus is applied across the whole film through illumination. For substrate illumination and strong light

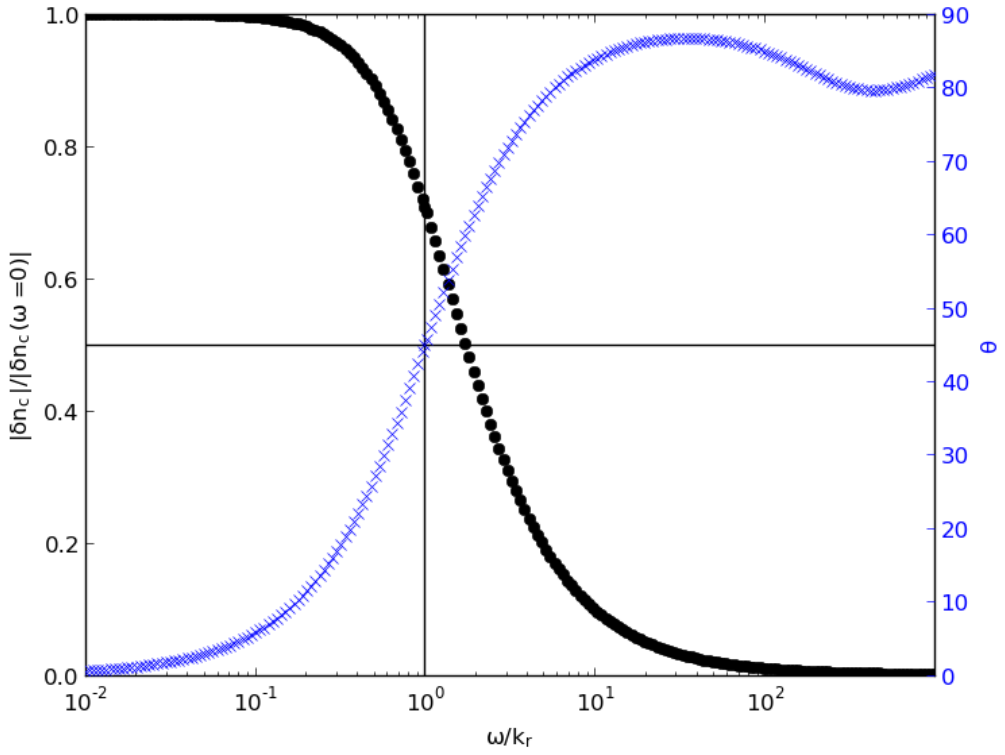

Figure 3.10: Simulated IMVS frequency response showing magnitude (circles) and phase (crosses). The horizontal line is at exactly 45°. The vertical line marks $\omega = \tau_0^{-1}$. $d = 10\mu\text{m}$, $\tau_0 = 10^{-4}\text{s}$, $D_0 = 0.5\text{cm}^{-2}\text{s}^{-1}$, $N_{t,0} = 0\ \text{cm}^{-3}$, $N_c = 1 \times 10^{22}\ \text{cm}^{-3}$, $\alpha = 1 \times 10^3\text{cm}^{-1}$, $I_0 = 10^{17}\text{cm}^{-2}\text{s}^{-1}$. $\beta = 1.0$.

harvesting (large α) the stimulus is also near to the substrate.

3.4.3 Intensity Modulated Photocurrent Spectroscopy (IMPS)

Intensity Modulated Photocurrent Spectroscopy (IMPS) is the response of a cell to a modulated light intensity under potentiostatic conditions. The amplitude and phase of the resulting photocurrent is recorded as a function of frequency and plotted on the complex plane. The governing equation is the same as for IMVS

$$\frac{\partial^2 \delta n_c}{\partial x^2} + \frac{\alpha \delta I_0 \exp(-\alpha x)}{D_0} - \mu^2(x,\omega)\delta n_c = 0. \tag{3.64}$$

and

$$\mu(x,\omega)^2 = \frac{i\omega\left(1 + \frac{\partial n_t}{\partial n_c}\right) + \tau_0^{-1}\beta(n_{ss}(x) - n_{eq})^{\beta-1}}{D_0}. \tag{3.65}$$

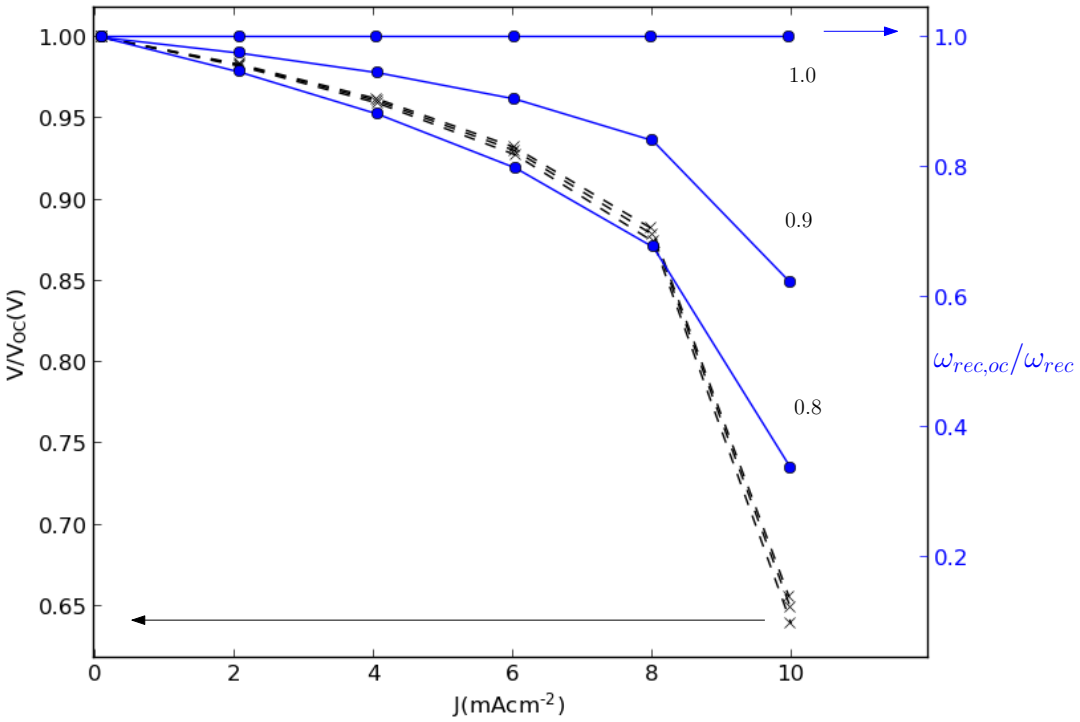

Figure 3.11: Cell bias (crosses) and ω_{rec} (circles) from simulated IMVS experiments where V_{OC} and τ_0 are the respective open circuit values. $d = 10\mu\text{m}$, $\tau_0 = 10^{-4}\text{s}$, $D_0 = 0.5\text{cm}^2\text{s}^{-1}$, $N_{t,0} = 0\ \text{cm}^{-3}$, $N_c = 1 \times 10^{22}\ \text{cm}^{-3}$, $\alpha = 1 \times 10^3\text{cm}^{-1}$, $I_0 = 10^{17}\text{cm}^{-2}\text{s}^{-1}$. $\beta = 1.0, 0.9, 0.8$.

Under potentiostatic conditions the boundary conditions become

$$\Re\left(\delta n_c\left(x=0\right)\right) = \Im\left(\delta n_c\left(x=0\right)\right) = 0 \tag{3.66}$$

and

$$\Re\left(\frac{d\delta n_c}{dx}_{x=d}\right) = \Im\left(\frac{d\delta n_c}{dx}_{x=d}\right) = 0. \tag{3.67}$$

The diffusion coefficient is related to the characteristic frequency by

$$\omega_{tr} = \frac{2.54 D_n}{d^2} \tag{3.68}$$

in the limit of weakly absorbed light [36]. We should expect the spectra to be independent of recombination since ω_{rec} is not proportional to the diffusion coefficient D_n. Indeed this is the case, Figure 3.12 shows the real and imaginary parts of the IMPS spectra at 6 different points along the IV-curve with a recombination order of $\beta = 1.0, 0.9, 0.8$. No difference between the spectra is discernible. No dif-

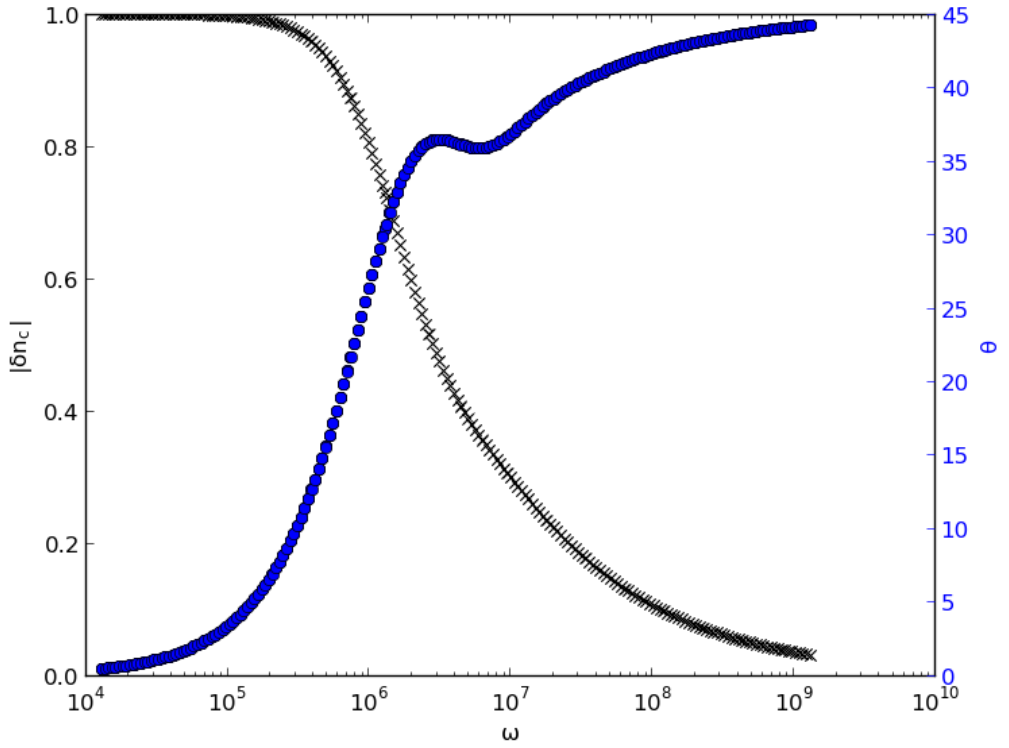

Figure 3.12: Simulated IMPS frequency response showing magnitude (crosses) and phase (circles). $d = 10\mu\text{m}$, $\tau_0 = 10^{-4}\text{s}$, $D_0 = 0.5\text{cm}^2\text{s}^{-1}$, $N_{t,0} = 0\ \text{cm}^{-3}$, $N_c = 1 \times 10^{22}\ \text{cm}^{-3}$,$\alpha = 1 \times 10^3\text{cm}^{-1}$, $I_0 = 10^{17}\text{cm}^{-2}\text{s}^{-1}$. $\beta = 1.0, 0.9, 0.8$. No dependence on β is visible.

ference between the spectra is discernible, this is expected since the characteristic IMPS frequency $\omega_t r$ is indicative of transport not recombination.

3.5 Results and Discussion

In this last section some examples are given to show the utility of the frequency dependent model.

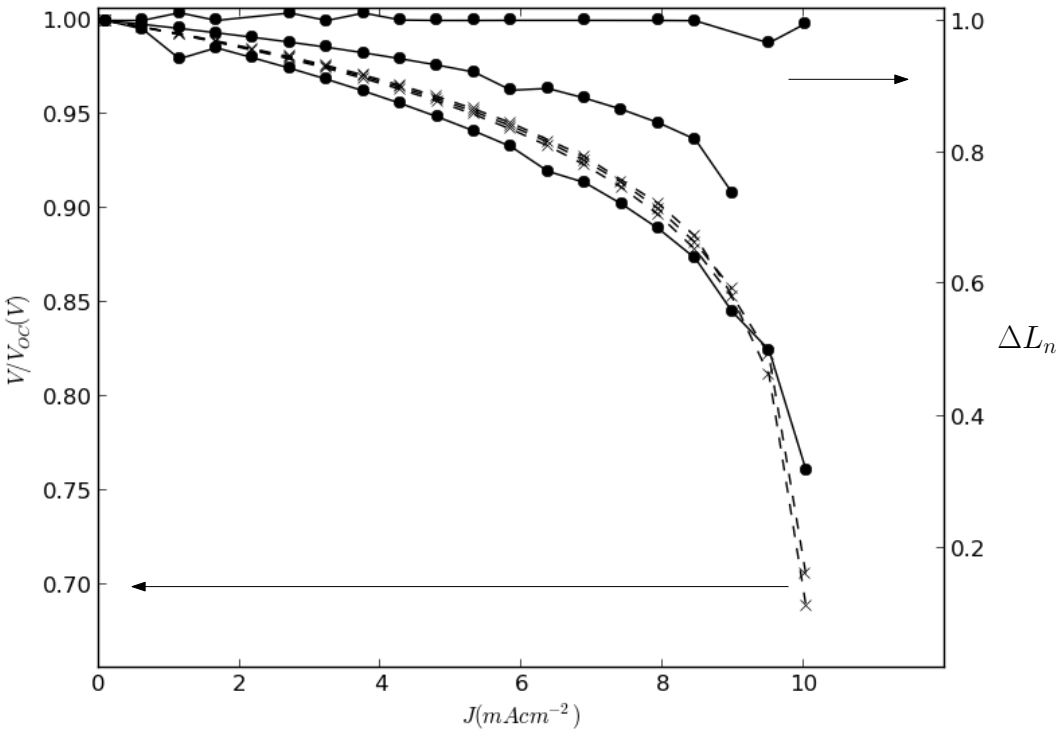

Figure 3.13: Simulated EIS measurements of the change in diffusion length ΔL (circles) and different points on the JV curve (crosses). $d = 10\mu$m, $\tau_0 = 10^{-4}$s, $D_0 = 0.5\text{cm}^2\text{s}^{-1}$, $N_{t,0} = 5 \times 10^{21}$ cm^{-3}, $N_c = 1 \times 10^{22}$ cm^{-3} , $T_0 = 800°$, $\alpha = 1 \times 10^3\text{cm}^{-1}$, $I_0 = 10^{17}\text{cm}^{-2}\text{s}^{-1}$. $\beta = 1.0, 0.9, 0.8$.

3.5.1 The relationship between the measured diffusion length and cell bias

Figure 3.13 shows simulations of diffusion length measurements using EIS at different points along the JV-curve for three cells where $\beta = 1.0, 0.9, 0.8$ by plotting

$$\Delta L_n = \sqrt{\frac{d^2\omega_{tr}}{\omega_{rec}}} / \sqrt{\frac{d^2\omega_{tr,OC}}{\omega_{rec,OC}}} \tag{3.69}$$

where $\omega_{tr,OC}$ and $\omega_{rec,OC}$ are the open circuit resonant frequencies with traps from figure 3.4 and d is the film thickness.

When $\beta = 1$ the diffusion length is constant irrespective of the operating point of the cell, even with an exponential trap distribution. This confirms that if the quasi-static approximation is valid then trapping effects will cancel out if the

product $L_0^2 = D_n\tau_n$ is taken confirming equation 3.58.

When $\beta \neq 1$ the diffusion length appears to decrease as the cell is moved to short circuit. If all the cell parameters were sufficiently well known then a fit could be performed to calculate β. However, even just observing this shift would still be interesting to contribute to the growing body of evidence suggesting that $\beta \neq 1$.

3.5.2 The relationship between the average carrier concentration and the measured diffusion length

Using the model it is straight forward to predict EIS spectra for any given steady state background concentration of photoelectrons. This provides the opportunity to compare the diffusion length calculated from the EIS spectra to the diffusion length expected from average concentration of photoelectrons in the device $\lambda\left(< n_c >\right)$ where, [70, 71]

$$\lambda_n\left(< n_c >\right) = \left(\frac{\beta < n_c >^{\beta-1}}{D_0\tau_0}\right)^{-\frac{1}{2}} \tag{3.70}$$

Figure 3.14 shows such a comparison. In each case the operating point of the cell has been moved from open toward short circuit. At each data point the diffusion length has been extracted from a calculated EIS spectra and the average background electron concentration, $< n_c >$, has been recorded. This has been repeated for reaction orders of 0.8 and 0.9.

From figure 3.14 it is clear that, as expected, the average concentration approximation will hold near open circuit. As short circuit is approached the extracted diffusion length will diverge from $\lambda(\langle n_c \rangle)$ towards lower values. For increasingly non-linear cells the two measures will diverge more significantly. This is also to be expected since the EIS perturbation is applied to the electron extracting electrode where n_c will be lower than average away from open circuit.

Ultimately neither description of the diffusion length produced here is correct and it would not be right to say that EIS underestimates or overestimates the diffusion length. The heart of the matter is that the diffusion length is not a good quantity if the cell is not near open circuit. If the cell is at short circuit

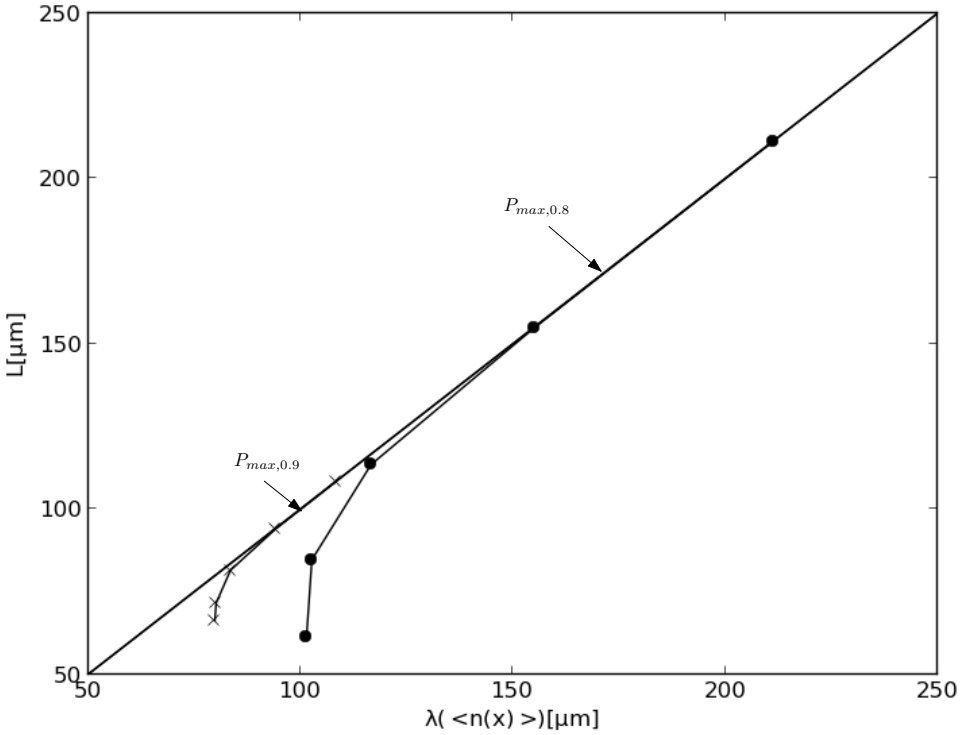

Figure 3.14: Diffusion length extracted from EIS simulations against the diffusion length expected from the average carrier concentration $\lambda(< n_c >)$ for different points along the IV-curve where $\beta = 0.8, 0.9$ (circles and squares respectively). $d = 10\mu\text{m}$, $\tau_0 = 10^{-4}\text{s}$, $D_0 = 0.5\text{cm}^2\text{s}^{-1}$, $N_{t,0} = 5 \times 10^{21}$ cm^{-3}, $N_c = 1 \times 10^{22}$ cm^{-3}, $T_0 = 800°$, $\alpha = 1 \times 10^3\text{cm}^{-1}$, $I_0 = 10^{17}\text{cm}^{-2}\text{s}^{-1}$.

there is no diffusion length, rather there is some position dependant distribution of electron lifetimes depending on $n_c(x)$. However, this does not mean that it is meaningless to conduct EIS away from open circuit. The results show that, for instance, at the maximum power point L_0 and $\lambda(\langle n_c \rangle)$ are consistent and using $\lambda(\langle n_c \rangle)$ is a good approximation.

3.5.3 The relationship between the shape of EIS spectra and cell nonlinearity

One may wonder how non-ideal behaviour changes the shape of the EIS spectra on the complex plane. This is a topical question since fitting of EIS spectra conventionally relies on the use of equivalent circuits with extra fitting parameters which do not have a clear physical interpretation. The prime example of this is

the use of constant phase elements rather than capacitors in the equivalent circuit in figure 3.1 [62, 56]. By understanding how non-linear recombination kinetics may change EIS spectra one may be able to replace abstract fitting parameters with terms from the continuity equation.

In order to inspect any change in the shape of EIS spectra one needs a benchmark as a point of comparison. The natural choice is to use the equivalent circuit shown in figure 3.5 to perform a fit to the simulated non-linear data [62]. The impedance $Z_{\mathrm{TiO_2}}$ can be written as

$$\mathrm{Z_{TiO_2}} = \sqrt{\frac{\mathrm{r_{ct}ct_{tr}}}{1+(i\omega/\mathrm{r_{ct}c_{\mu}})}}\coth\left((\mathrm{r_{ct}c_{\mu}}/\omega_{tr})\sqrt{1+(i\omega/\mathrm{r_{ct}c_{\mu}})}\right) \tag{3.71}$$

Expressions for $\mathrm{r_{ct}}$, $\mathrm{r_{tr}}$, $\mathrm{c_{\mu}}$ have all been given in section 3.3.2. This leaves ω_{tr} which is varied to give the best fit.

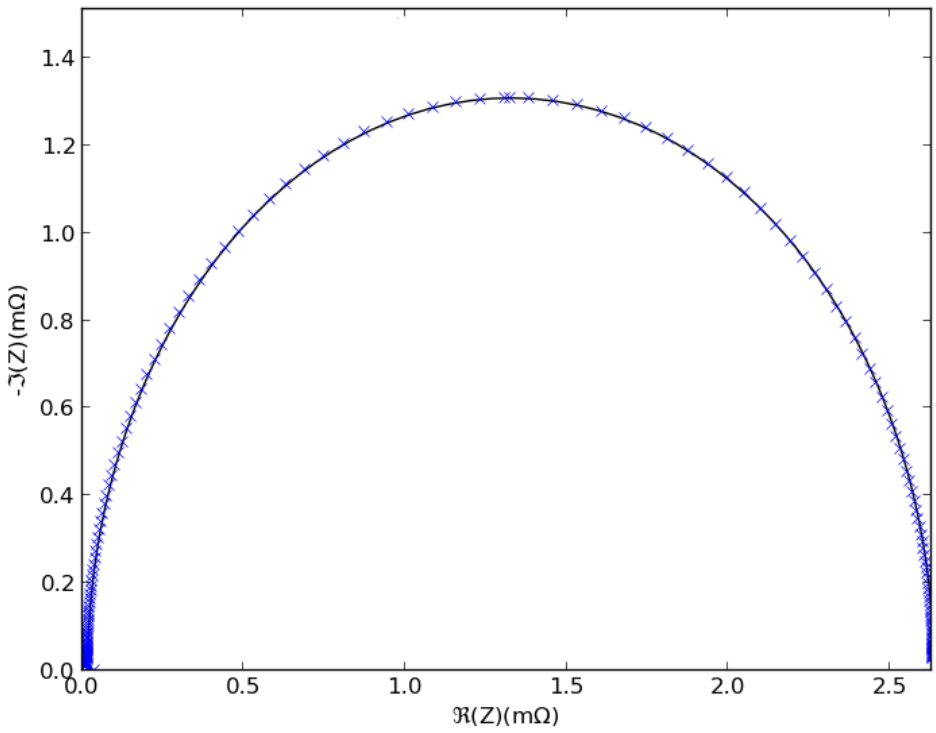

Figure 3.15: Simulated EIS spectra at short circuit without trapping (crosses) and curve fit using equation 3.71 (line). $d = 10\mu\mathrm{m}$, $\tau_0 = 10^{-4}\mathrm{s}$, $D_0 = 0.5\mathrm{cm^2s^{-1}}$, $N_c = 1\times10^{22}\ \mathrm{cm^{-3}}$. Fitted using $\omega_{tr} = 0.485\times10^6$.

Figures 3.15 and 3.16 show that is perfectly possible to fit the linear equiva-

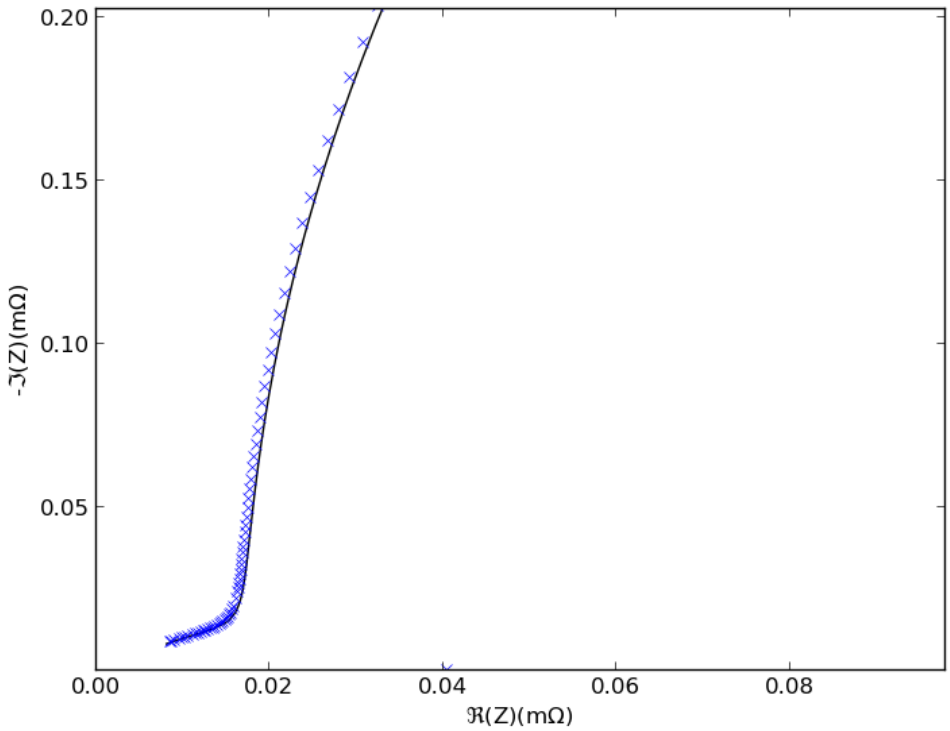

Figure 3.16: As in figure 3.15 but showing data points only at high frequencies.

lent circuit model to the full model with non-linear recombination provided that trapping effects are not included. This is to be expected given that the low frequency section of the plot, which is governed by recombination, is normally fitted successfully with the equivalent circuit model using real non-linear cells. The fit has been made to a short circuit simulation where one would expect any changes in the spectra to be greatest since the electron concentration changes most dramatically through the device under these conditions.

Figures 3.17 and 3.18 show that the data is no longer possible to fit using equivalent circuits once trapping effects are included. This is not surprising given that this high frequency section of the spectra is the hardest to fit when analysing real cells and given that the equivalent circuit does not contain anything resembling a concentration dependant trapping term. One may be tempted to improve the closeness of the fit by replacing the capacitors in the equivalent circuit with constant phase elements however, this would not be advised for the following reason. Mathematically the use of constant phase elements is equivalent to adding the

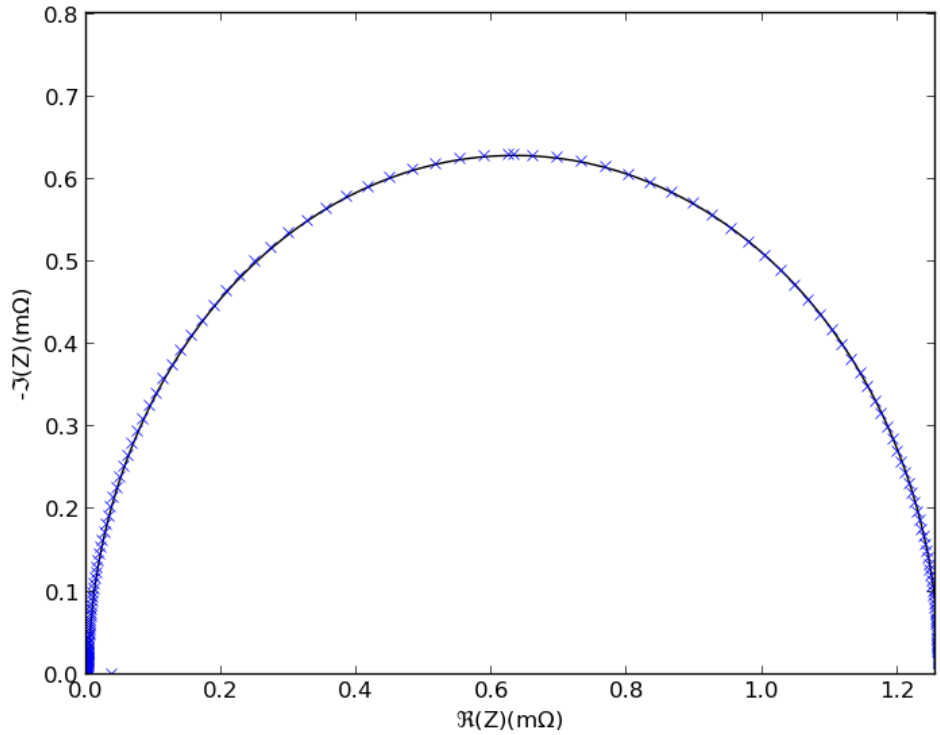

Figure 3.17: Simulated EIS spectra at short circuit with trapping (crosses) and curve fit using equation 3.71 (line). $d = 10\mu m$, $\tau_0 = 10^{-4}s$, $D_0 = 0.5cm^2s^{-1}$, $N_c = 1 \times 10^{22}$ cm^{-3}, $N_{t,0} = 5 \times 10^{21}$. Fitted using $\omega_{tr} = 2.5$.

factor β_{CPE} [62]

$$Z_{TiO_2} = \sqrt{\frac{r_{ct} ct_{tr}}{1 + (i\omega / r_{ct} c_\mu)^{\beta_{CPE}}}} \coth\left((r_{ct} c_\mu / \omega_{tr})^{\frac{\beta_{CPE}}{2}} \sqrt{1 + (i\omega / r_{ct} c_\mu)^{\beta_{CPE}}} \right). \tag{3.72}$$

By taking the high frequency limit of this expression one can show that β_{CPE} controls the phase of Z_{TiO_2} at high frequencies [62]

$$\theta(\omega \to \infty) = \tan\left(\frac{\beta_{CPE} \pi}{4} \right). \tag{3.73}$$

When $\beta_{CPE} = 1$ then at high frequencies the phase will tend to 45°. This is observed in figure 3.18 and any attempt to fit the spectra using constant phase elements results in $\beta_{CPE} = 1$ which reduces the fit to the standard equivalent circuit without constant phase elements. This affirms the original proposition by Bisquert and coworkers that constant phase elements should be attributed to capacitance between TiO_2 and the electrolyte which is not included in this

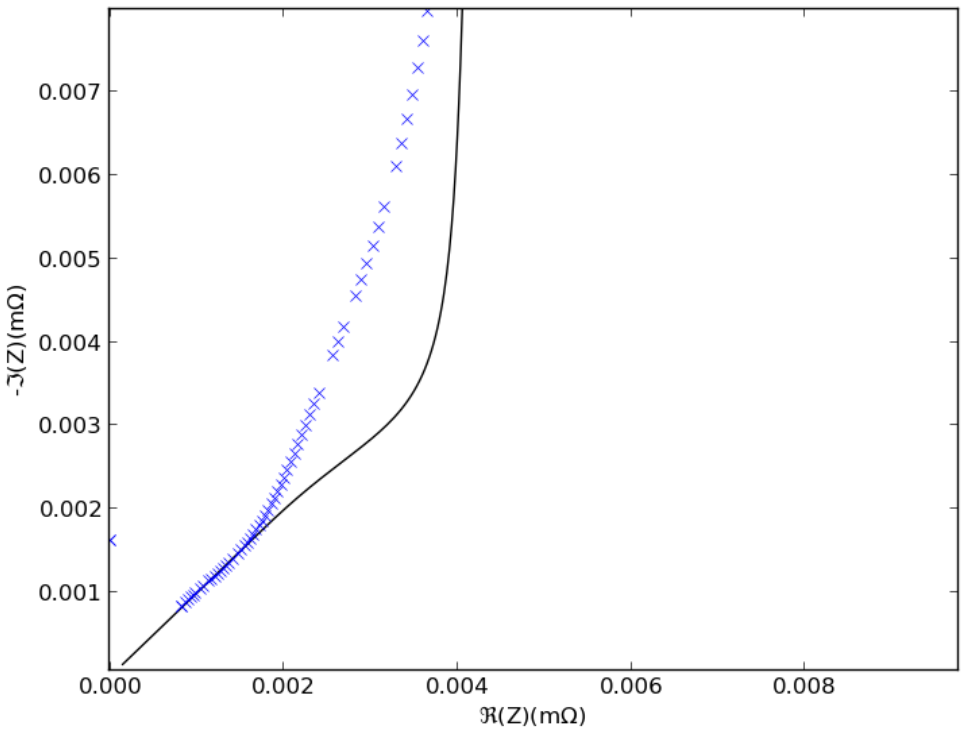

Figure 3.18: As in figure 3.15 but showing data points only at high frequencies.

model [62].

The failure of the equivalent circuit model to fit multiple trapping begs the question, if EIS spectra cannot be fitted with realistic trapping then why has this not been a problem when fitting experimental data? It is likely that these trapping effects are not pronounced enough to prevent fitting under seasonable circumstances. For instance in figure 3.19 the cell is moved to the maximum power point and the fit is recovered because there is much less variation in electron concentration through the device. Moreover the discrepancy is probably masked by capacitance at the TiO_2/electrolyte interface.

3.6 Conclusions

A model for the frequency response of non-ideal DSC photoanodes has been presented for modelling EIS, IMPS and IMVS experiments on non-ideal cells for

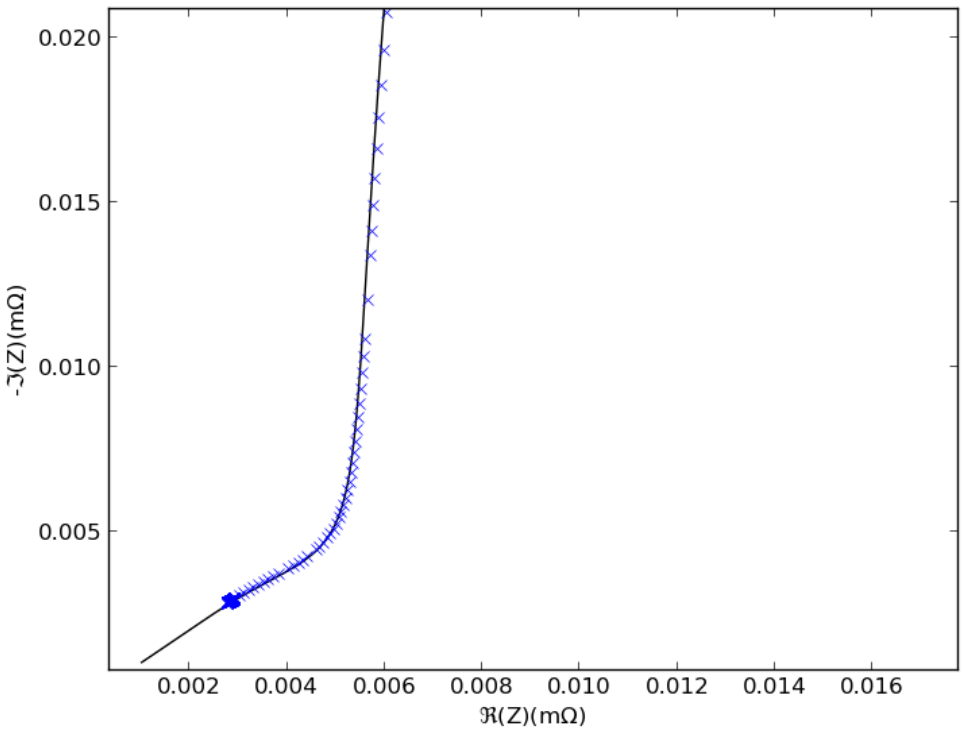

Figure 3.19: Reproduction of 3.15, showing data points only at high frequencies, calculated at the maximum power point rather than short circuit. Fitted using $\omega_{tr} = 75$.

the first time. The frequency response for the anode has been presented for each of the experiments using recombination orders of $1.0, 0.9, 0.8$. The results predict that the measured carrier lifetime will decrease as the cell is moved from open circuit to short circuit conditions. It should be emphasised that the model only considers the impedance of the TiO_2 photoanode and to make a true comparison to experimental data the substrate and electrolyte impedances will need to be included. The model is however a vital stepping stone towards a full impedance model of DSSC.

Even though the model does not consider a full cell it has still been possible to make some useful and interesting insights at this stage. The overriding conclusion is that despite the governing equations behind frequency dependant measurements being complex, the resulting behaviour can be interpreted using relatively simple and practical techniques. It is well known that EIS data can be fitted using relatively simple procedures using equivalent circuits and the model presented in this chapter has been used as a particularly rigorous test of these procedures. The results show clearly that even in the presence of an exponential trap dis-

tribution and non-linear recombination the diffusion length can still be reliably extracted from EIS spectra and the results have a simple physical interpretation. At open circuit the diffusion length is well defined and at the maximum power point length can be interpreted in terms of an average diffusion length.

The behaviour which is not produced by the model gives further insight. For instance, neither trapping or non-linear recombination could simulate capacitative dispersion consistent with constant phase elements hence one can be reasonably certain the origin of this dispersion is not recombination or trap related.

It is interesting to compare these conclusions to those from simulated charge collection efficiency experiments using transient decay rates presented for non-ideal cells by Sivaram and co-workers [63]. This is one of the few other studies where non-ideal behaviour has been fully included by using a numerical simulation. Here non-ideal cell behaviour manifests as an overestimation of charge collections efficiency compared to the true value. Although EIS and transient decay measurements are very different both experiments elucidate a key property of the underlying equations that govern cell behaviour. There is no universal correction factor that can be applied to either of these measurements to account for under or overestimates resulting from non-linear recombination. In both cases simulation is required to interpret the results with the exception of a small set of special cases. Ultimately this is because in the presence of non-linear recombination and trapping any measurement will be a functional of $n_c(x)$ through the whole device and at present $n_c(x)$ can only be calculated numerically.

Chapter 4

Measuring the diffusion length using patterned electrodes

In general, the diffusion length L_0 is the average distance a carrier diffuses in a semiconducting film before recombining. In the particular case of DSCs it is the mean distance an electron travels in the TiO_2 conduction band before recombining with I_3^-. Recall from section 2.4.5 that

$$L_0 = \sqrt{D_0 \tau_0} = \sqrt{D_n \tau_n}. \tag{4.1}$$

An early method for measuring the diffusion length of electrons in germanium is that of Harrick shown in figure 4.1 [64]. The rods are illuminated at one end, then the density of photoelectrons is measured using infra-red absorption techniques as a function of position. The concentration of photoelectrons is kept sufficiently low such that carriers move purely by diffusion. Recombination is due to electron hole annihilation. Harrick's experiment is convincing because it is an intuitive and direct measurement of what is happening in the material. This is not always the case for measurements of L_0 in DSCs, for example, the techniques presented in chapter 3 required numerical analysis in order to extract the correct result. There has been much debate in the past over the correct value of the diffusion length, often because linear ($\beta = 1$) recombination kinetics have been assumed [65, 66]. This chapter concerns determining the diffusion length in a TiO_2 DSC anode in a similar spirit to Harrick. By patterning the electron extracting substrate of a DSC, a simple and intuitive method of measuring the

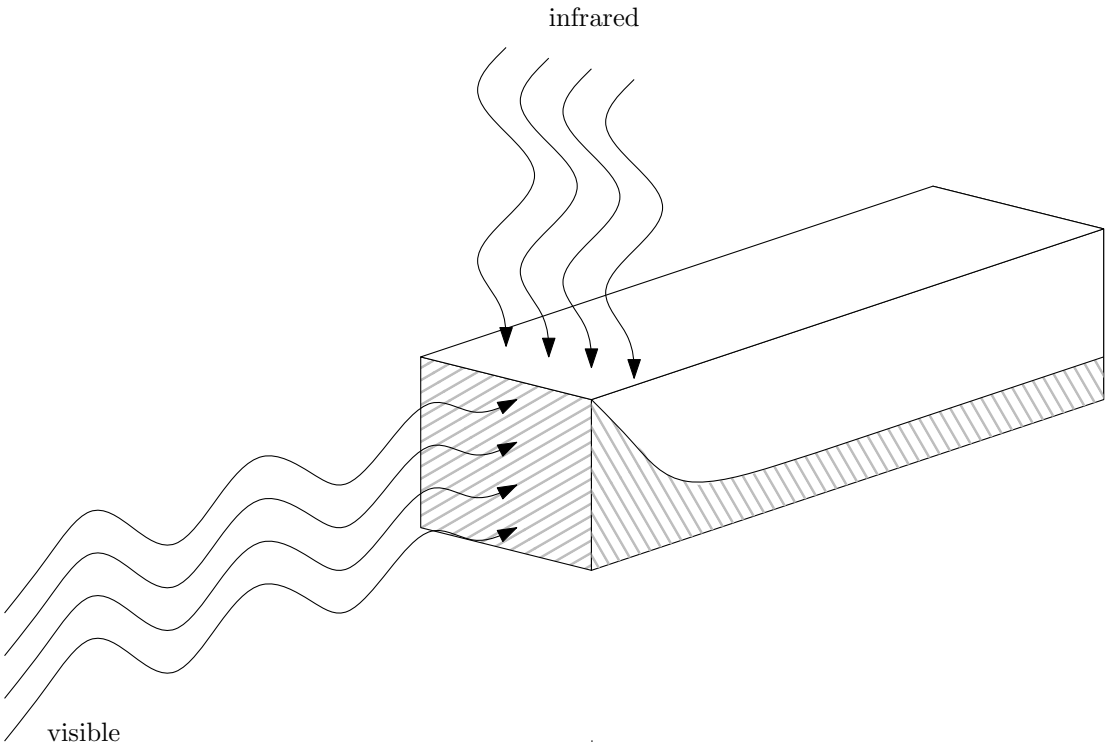

Figure 4.1: Harrick's diffusion length experiment. Carriers are created by illuminating the end of the germanium rod. The carrier concentration along the rod can be probed using an infrared beam from the top. The carrier concentration (shaded area) decreases along the rod.

diffusion length may be produced. In particular, this chapter is concerned with the theory and modelling behind this experiment which was used to confirm and interpret the results. The key result is that the diffusion length is $L_0 \sim 100\mu$m at high open circuit voltages ($\approx$ 800mV). The change in diffusion length with electron concentration is consistent with a recombination reaction order of $\beta = 0.88$. This is consistent with results using impedance spectroscopy [49, 67, 65] and IPCE measurements [68]. Moreover these results can be analysed without the use of any complex numerical model. These findings have been published in The Journal of Physical Chemistry C [69].

For the remainder of this subsection the IPCE method is reviewed and analysed in terms of the continuity equation and non-ideality. This is the predominant time independent diffusion length measurement. In the next section the patterned substrate method is introduced and a new expression for the diffusion length is derived. The results are then confirmed with a 1D and 2D model of electron diffusion with patterned electrodes.

4.0.1 The IPCE method

The diffusion length in DSCs can be measured by using two time independent illumination sources. A bias light causes a generation rate of G photoelectrons in the cell per unit volume. If a small extra source of illumination is then activated the generation rate becomes $G + \delta G$. If all time derivatives are zero then the equation for $n_c(x) + \delta n_c(x)$ may be written

$$\frac{d^2}{dx^2}\left[n_c(x) + \delta n_c(x)\right] = \frac{\left(n_c(x) + \delta n_c(x) - n_{eq}\right)^{\beta}}{\tau_0 D_0} - \frac{G}{D_0} - \frac{\delta G}{D_0} \tag{4.2}$$

The non first order recombination factor $\beta \neq 1$ requires that this equation must be solved numerically if one wants to solve for the total electron concentration in the conduction band. An analytically solvable expression for the perturbed electron concentration δn_c may be constructed if δn_c is sufficiently small. By collecting first order terms containing δn_c and disregarding higher order terms one finds that

$$\frac{d^2 \delta n_c(x)}{dx^2} = \frac{\delta n_c}{\lambda_n^2(n_c)} - \frac{\delta G}{D_0} \tag{4.3}$$

where

$$\lambda_n(n_c) = \left(\frac{\beta n_c^{\beta-1}}{D_0 \tau_0}\right)^{-\frac{1}{2}} \tag{4.4}$$

is a local diffusion length for the perturbed concentration $\delta n_c(x)$. The expression for λ_n is valid providing that

$$\left(n_c + \delta n_c + n_{eq}\right)^{\beta} \approx \left(n_c + \delta n_c\right)^{\beta} \approx n_c^{\beta} + \beta n_c^{\beta-1} \delta n_c \tag{4.5}$$

when n_{eq} and δn_c are small. If the cell is near open circuit then $n_c(x)$ is approximately constant and equation 4.4 can be solved without the need for computer simulations. This is the same interpretation of the local diffusion length as Bisquert and Mora-Seró or Barnes and O'Regan [70, 71].

Conventional IPCE measurements are conducted by comparing the IPCE for front side and rear side illumination under short circuit conditions and more recently potentiostatic conditions are used to compare perturbed and non-perturbed cells [71, 72, 68, 65]. Using the perturbation method outlined above the IPCE

for illumination through the electrolyte (or electrolyte electrode, EE) is given by

$$\mathrm{IPCE}_{col,EE}(\alpha, d, n_c) = \frac{\left[-\lambda_n(n_c)\,\alpha\cosh\left(d/\lambda_n(n_c)\right) + \sinh\left(d/\lambda_n(n_c)\right) + \lambda_n(n_c)\,\alpha e^{-\alpha d}\right]\lambda_n(n_c)\,\alpha}{\left(1-e^{-\alpha d}\right)\left[1-\lambda_n(n_c)^2\,\alpha^2\right]\cosh\left(d/\lambda_n(n_c)\right)} \tag{4.6}$$

and the IPCE though the substrate electrode (SE) is given by

$$\mathrm{IPCE}_{col,SE}(\alpha, d, n_c) = \frac{\left[\lambda_n(n_c)\,\alpha\cosh\left(d/\lambda_n(n_c)\right) + \sinh\left(d/\lambda_n(n_c)\right) - \lambda_n(n_c)\,\alpha e^{\alpha d}\right]\lambda_n(n_c)\,\alpha e^{-\alpha d}}{\left(1-e^{-\alpha d}\right)\left[1-\lambda_n(n_c)^2\,\alpha^2\right]\cosh\left(d/\lambda_n(n_c)\right)} \tag{4.7}$$

as derived from equation 4.4 where

$$\delta n_c(x=0) = 0 \tag{4.8}$$

and

$$\left.\frac{\delta n_c(x)}{dx}\right|_{x=d} = 0. \tag{4.9}$$

Using these equations the local diffusion length λ_n may be calculated. Jennings in particular has shown clearly that IPCE measurements and EIS experiments are consistent providing that the cells are at the same open circuit voltage [65].

4.1 The patterned substrate method

Measuring the diffusion length using patterned substrates improves on the IPCE method by reducing the fitting to only a single parameter. The result is completely independent of the shape of the anode or any optical characteristics. The structure of the experiment is shown in figure 4.2. Half of the FTO contacting the TiO_2 to the external circuit is removed (through laser ablation) and half remains intact. This results in stripes of FTO and glass each with width s. Figure 4.3 is a white light interferometry image of the FTO/glass stripes showing a 3D perspective. To interpret the experiment it was necessary to solve the continuity equation for the perturbed conduction band electron concentration (4.4) to find the relationship between s and λ_n.

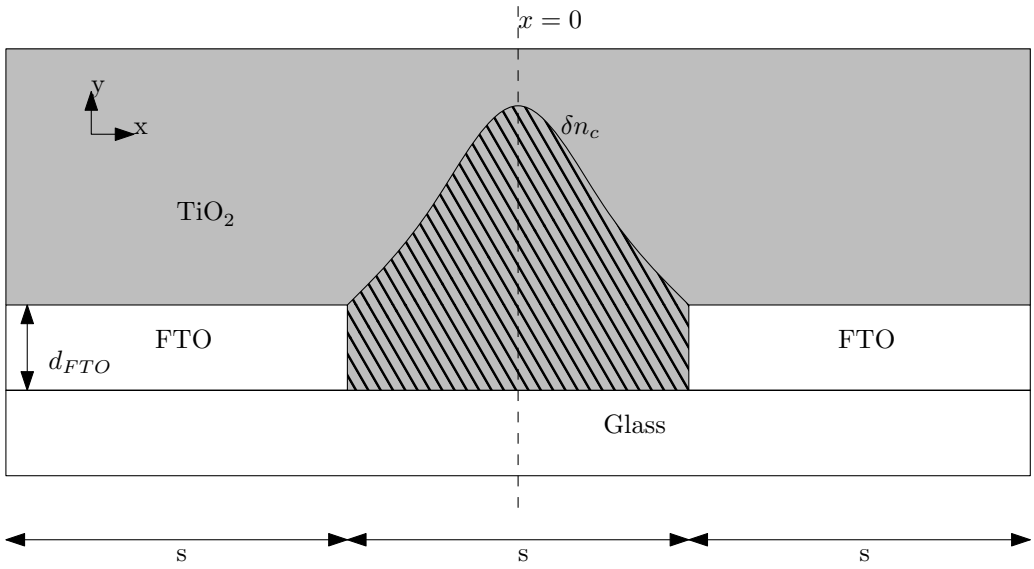

Figure 4.2: The patterned electrode experiment. The contact is made of strips of FTO with width s (electron extracting) and strips of glass also with width s (not electron extracting). The electron concentration n_c is high nearest the glass and low near the FTO. The IPCE is measured for a set of cells each with different length s and the diffusion length can be calculated. The thickness of the FTO layer is d_{FTO}.

4.1.1 The 1D patterned substrate model

To find λ_n equation 4.4 must be solved for the situation in figure 4.2. If n_c is approximately constant in the y direction and if $d_{FTO} << L$ then the situation in figure 4.2 amounts to solving the diffusion equation (2.11) in the steady state for weakly absorbed light ($\alpha d << 1$).

$$\frac{d^2\delta n_c(x)}{dx^2} + \frac{\alpha I_0 e^{-\alpha x}}{D_0} - \frac{\delta n_c(x)}{\lambda_n^2\,(n_c)} = 0 \tag{4.10}$$

If $x = 0$ is the center of a glass stripe and if

$$\delta n_c(-s/2) = \delta n_c(s/2) = 0 \tag{4.11}$$

then the solution is given by

$$\delta n_c(x) = \alpha I_0 \tau_n \left(1 - \frac{e^{x/\lambda_n(n_c)} + e^{-x/\lambda_n(n_c)}}{e^{s/2\lambda_n(n_c)} + e^{-s/2\lambda_n(n_c)}}\right). \tag{4.12}$$

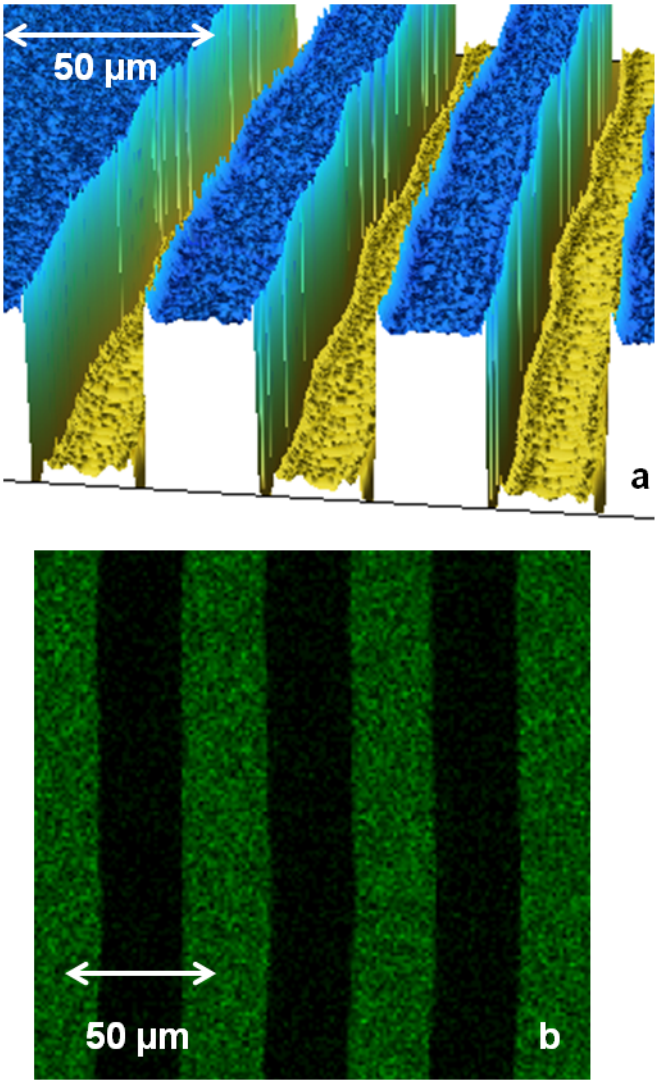

Figure 4.3: White light scattering experiments performed by Dunn and Wastin showing the substrate patterning.

Given that the perturbed current density (due to extra electrons δn_c) provided to the external circuit by each stripe must be

$$\delta j = D_n \left(\frac{d\delta n_c}{dx}_{x=-s/2} - \frac{d\delta n_c}{dx}_{x=s/2} \right) \tag{4.13}$$

the relative electron collection efficiency can be calculated, η_{rel}. This is defined as the current density from a cell with an ablated FTO film of stripe width s divided by the current density from a cell where $s = 0$

$$\eta_{rel} = \frac{\delta j\,(s)}{\delta j\,(s=0)} = \frac{1}{2} + \frac{\tanh\left(s/2\lambda_n\left(n_c\right)\right)}{s/\lambda_n\left(n_c\right)}. \tag{4.14}$$

If one has a set of cells with a range of known s one can calculate $\lambda_n(n_c)$ by fitting η_{col} to equation 4.14.

4.1.2 The 2D patterned substrate model

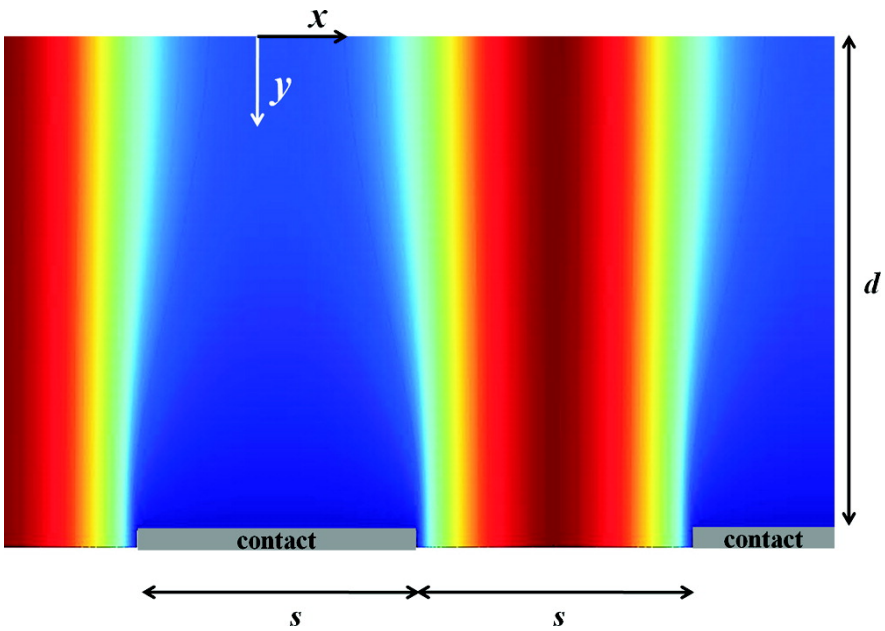

Figure 4.4: Two dimensional solution to the continuity equation with $d = 6.5\mu m$, $s = 30\mu m$, $L = 100\mu m$, $\tau = 1 \times 10^4 s$, $\alpha = 340/cm$, $I_0 = 10^{16} cm^{-2} s^{-1}$. $n(x, y)$ varies from 0 (dark blue) to 4.85×10^{12} electrons/cm^{-3}(dark red). Not to scale.

To test the validity of the 1D model and equation 4.14 a 2D simulation was constructed where n_c is allowed to vary in the y-direction. The thickness of the FTO layer was also included so that $d_{FTO} \neq 0$ as illustrated in figure 4.4. This was performed using the COMSOL Multiphysics finite element package. Zero flux conditions were imposed at all boundaries except for at the FTO edges where a zero concentration condition was imposed. The governing equation, now with two spatial derivatives, becomes

$$\nabla^2 \delta n_c(x, y) + \frac{\alpha I_0 e^{-\alpha x}}{D_0} - \frac{\delta n_c(x, y)}{\lambda_n^2(n_c)} = 0 \tag{4.15}$$

Figure 4.4 is an example of a 2D solution. This calculation was performed for a film thickness $d = 6.5\mu m$ and local diffusion length $\lambda_n = 100\mu m$. Note that for

equation 4.14 there is the requirement that

$$d << L_0 \tag{4.16}$$

otherwise there will be a dependency of the solution in the y-direction. Figure 4.5 compares the 2D solution with equation 4.14 which are in excellent agreement showing that equation 4.14 is valid in this case.

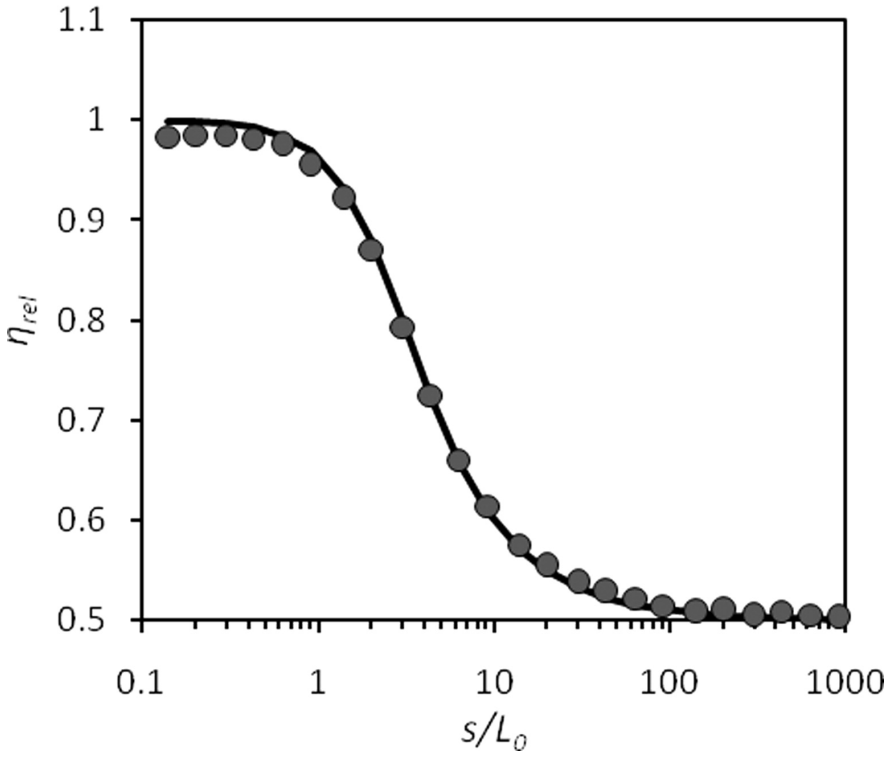

Figure 4.5: Comparison between the two dimensional model (points) and the 1D model (line) using the same parameters as in figure 4.4.

4.2 Results

This section presents the results of Dunn and Westin fitted using the 1D patterned electrode model to calculate the diffusion length and electron recombination reaction order β [69].

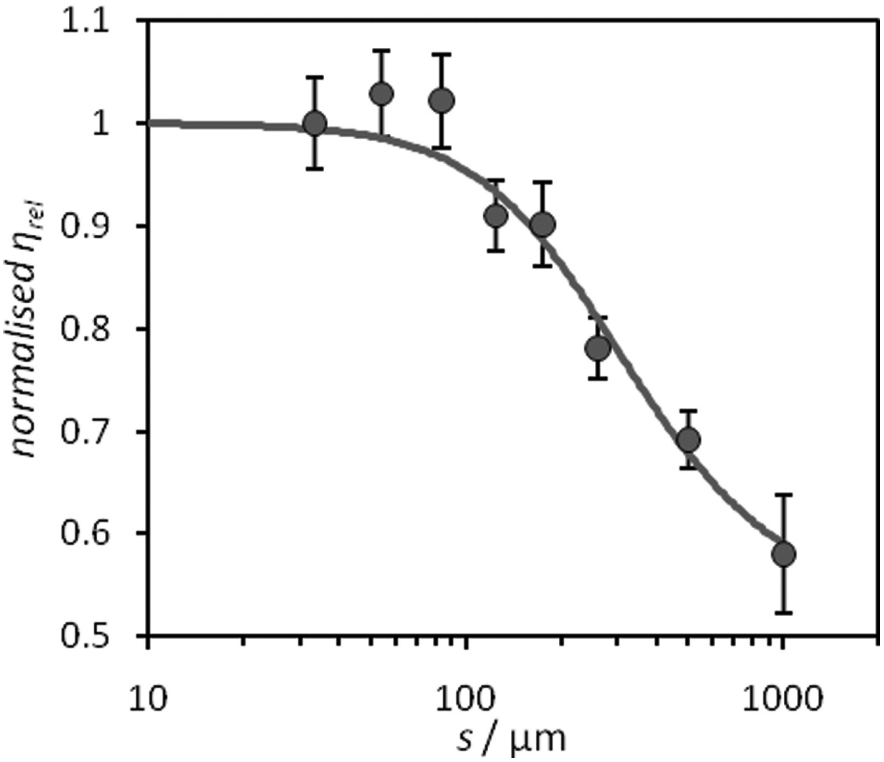

Figure 4.6: Comparison between measurements by Dunn and Westin at open circuit and equation 4.14. 627nm illumination with a photon flux of $9 \times 10^{15}\text{cm}^{-2}\text{s}^{-1}$. The value of the first data point before normalisation was 85%. The best fit was given for $L_0 = 90\text{nm}$.

4.2.1 Determining the local diffusion length

Figure 4.6 shows data collected by Dunn and Westin compared to equation 4.14 [69]. For the case where $s < 80\mu\text{m}$ the relative collection efficiency n_{rel} is independent of s. When $s > 80\mu\text{m}$ n_{rel} decreases rapidly, implying that the local diffusion length is of the order of 80µm under these conditions.

When $s << L_0$ experimental η_{rel} converged to 85% yet 4.14 predicts that η_{rel} ought to converge to 100%. The reason for this is not clear but it has been suggested that light scattering due to the patterned FTO may change the path length of light through the device giving an artificially low collection efficiency. In order to compare the experimental results with equation 4.14 the experimental results have been scaled so that they tend to $n_{rel} = 1$ when $s << L_0$.

The error bars in figure 4.6 and 4.7 represent the standard deviation of n_{rel} taken from different cells divided by the square root of the number of samples (5-7

cells).

4.2.2 Determining cell nonlinearity

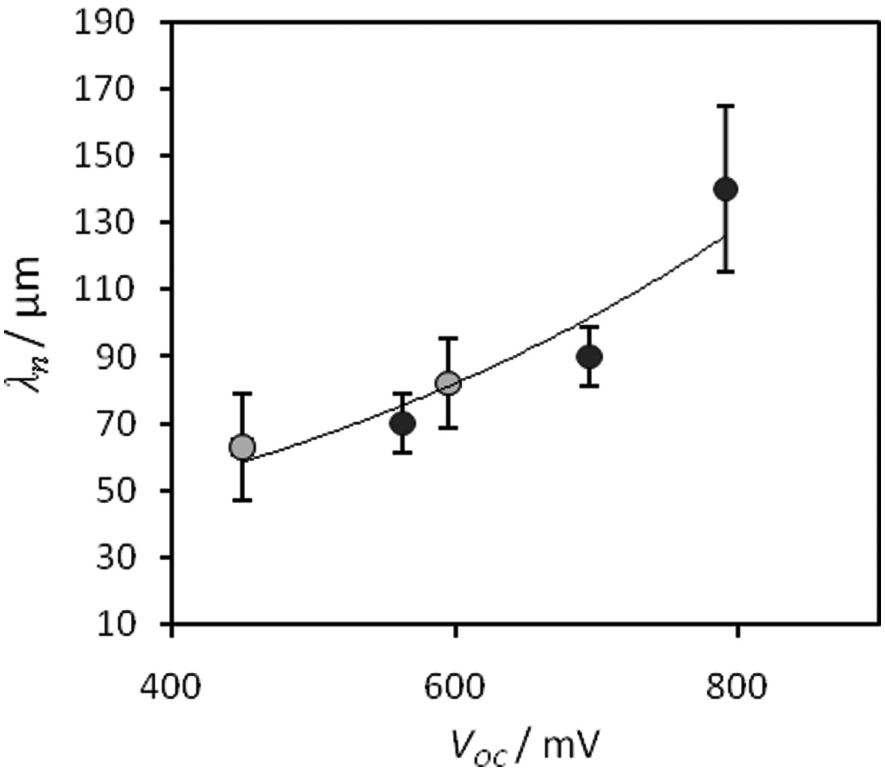

Figure 4.7: Diffusion length calculated using equation 4.14 from experiments by Dunn and Westin at open circuit (black circles) and at the maximum power point (gray circles) consistent with a reaction order of $\beta = 0.88$.

The reaction order for electron recombination was determined by fitting equation 4.14 to a series of cells under progressively higher illumination intensities and hence open circuit voltages as shown in figure 4.7. This was performed both at open circuit (black circles) and at the maximum power point (gray circles) where the electron concentration is still approximately constant. The results are consistent with a reaction order of $\beta = 0.88$. Error bars are as in figure 4.6.

4.2.3 Discussion

Figure 4.7 contains points taken at both open circuit and at the maximum power point. At the maximum power point background concentration of electrons

$n_c(x, y)$ will change in the y-direction (using the coordinate system in figure 4.4) unlike at open circuit. Experiments at the maximum power point are still a true indication of how far electrons are diffusing before recombining, $n_{rel}(s)$ still has the same form at the maximum power point as at open circuit and there is still a clear plateaux for small s where n_{rel} is independent of s. However, the potential at the contact will be lower than in the rest of the anode so one would expect that the points will be shifted to slightly to the left on the figure since the potential in the film is higher than at the contact. Indeed this appears to be the case although given the size of the error bars one cannot conclusively state the magnitude of this shift exactly. As an approximate guide figure 4.8 shows the photoelectron concentration in a 6.5µm thick film where electrons have a diffusion length $L = 63$µm and a flux of 10^{17}photons cm^{-2}s^{-1} is incident. The potential difference between the front and the rear of the film is approximately 10mV so one would expect a shift of this order of magnitude. Such a shift is consistent with figure 4.7 and suggests that one can get a good indication of the diffusion length at the maximum power point using this method.

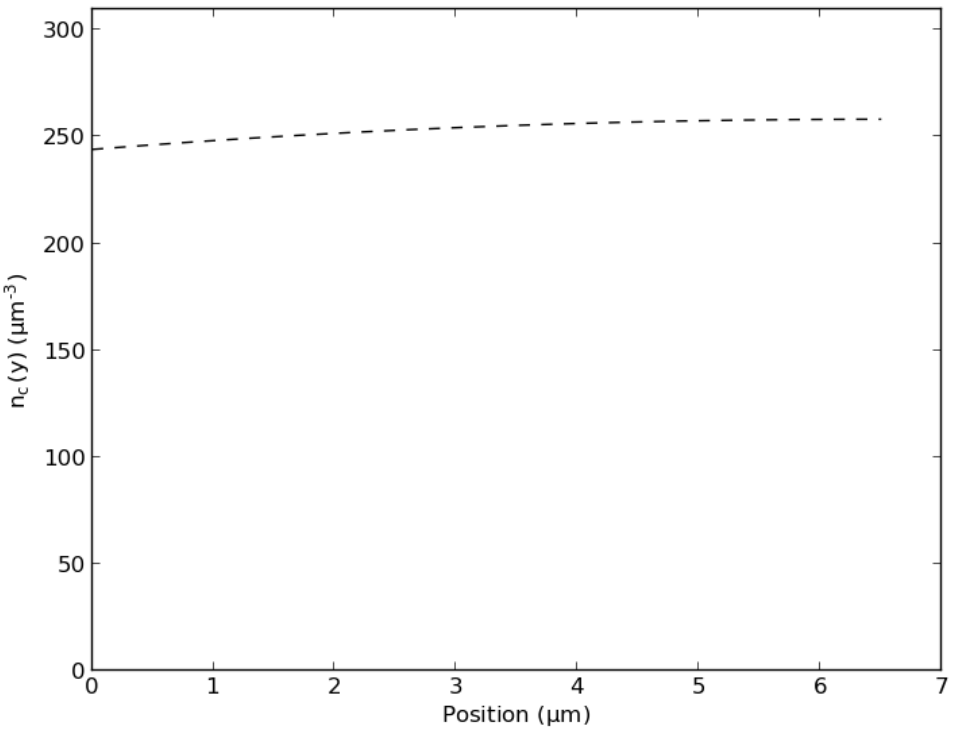

Figure 4.8: Solution to the continuity equation 2.11 showing the photoelectron concentration at the maximum power point where $D = 0.4\text{cm}^{-2}\text{s}^{-1}$, $\tau = 10^{-4}\text{s}^{-1}$,$d = 6.5$µm, $\alpha = 340\text{cm}^{-1}$ and photon flux $I_0 = 1 \times 10^{17}\text{cm}^{-2}\text{s}^{-1}$.

One remaining ambiguity is why the relative collection efficiency does not tend to 100% for very small ablation channels of width s. A likely explanation is that the FTO layer causes scattering and by removing half of this FTO the average path length through the TiO_2 film is decreased. Whatever the explanation it is difficult to see how this would change the fundamental interpretation of the result. Ultimately there is a well defined transition from good to poor collection and this must be governed by the diffusion length.

The results are in good agreement with impedance spectroscopy, front and rear side IPCE measurements and frequency resolved small amplitude techniques [49, 67, 65]. The method presented is a simple determination of the diffusion length which is intuitive and only dependant on the diffusion length itself. The diffusion length for the cells used was between 50 and 100μm increasing with fermi level, as would be expected from the continuity equation where $\beta = 0.88$. The diffusion length can be measured using a host of methods however the patterned substrate method is unique because it is so simple and intuitive leaving little room for debate. Although the method is probably too laborious to use on a regular basis it is a good 'yard stick' which can be used to evaluate the effectiveness of other methods.

Chapter 5

Real-Time Optical Waveguide Measurements of Dye Adsorption

DSC's have been studied for over 20 years, however, there is surprisingly little information available on some crucial aspects of cell construction and assembly, especially the application of dye to TiO_2 films. This chapter will study dye diffusion, adsorption and surface coverage in porous TiO_2 films used as DSC photo anodes, an area which has been addressed only minimally in the literature to date. Of particular interest is how the dye becomes attached to the TiO_2 and the requirement for long 12 hour dying times.

Conventionally TiO_2 films are immersed in dye solution for approximately 12 hours. A common example would be N-719 dye using a 0.3 m mol dm^{-3} solution dissolved in a 50:50 t-butanol-acetronitrile mixture [73]. This is a good method in the sense that it tends to produce the most efficient cells, however, there have been no quantitative studies as to why 12 hours is the optimal time and in any case a 12 hour dying process is impractical for any kind of mass production. Ideally, if the dye could be imaged as it moves through the film then perhaps it would be more straightforward to understand the key factors in this process. Figure 5.1 shows two possible ways that the dye might move though the TiO_2 film, one limited by diffusion and one limited by adsorption. The figure presents two extremes but it is still not clear if either of these represents the actual system.

The need to observe the distribution of dye throughout the film has become more

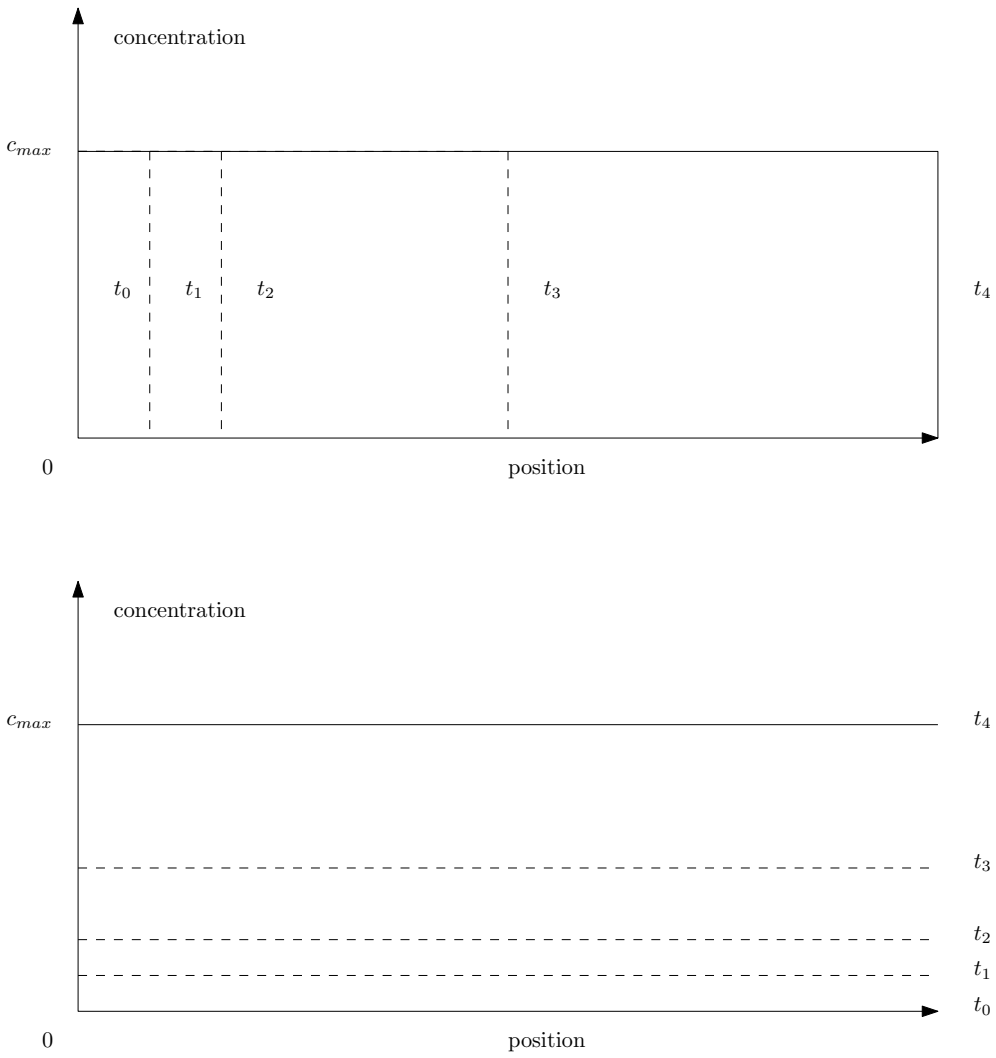

Figure 5.1: Two possible profiles of dye within a TiO_2 film at times t_0,t_1,t_2,t_3 and t_4 after the initial introduction of dye to the surface limited by transport (top) and adsorption (bottom).

pressing with the advent of new dyes with very high optical absorption coefficients where a thin surface coverage could give the illusion of a well dyed film [74, 75, 76, 77, 78]. The variety of dyes is also increasing. For example, organic indoline dyes and efficient copper dyes. It would be useful to compare the diffusion, adsorption and surface coverage of these dyes with more conventional dyes [79, 80, 81]. Similar studies of coadsorbates such as thiocyanate and deoxycholic acid, which have been found to increase efficiency, could be equally useful [78, 82, 83]. Finally, more detailed studies in this area could help to design fast dyeing techniques such as the addition of tetrabutyl-ammonium 30-hydrate to the dye solution but with a less negative impact on efficiency [84].

There are a plethora of so called integral techniques which can measure the total amount of dye in a film however, very little information is collected which describes where the dye is within the film (spatial information). Optical waveguide spectroscopy (OWS) is a new technique that uses a laser to excite guided modes within the TiO_2 film. A key result of this chapter will be that the wavevector of each guided mode can then be used to calculate the total amount of dye in the film. This is demonstrated using a computer model of the experiment which will be presented in sections 5.3 5.4 and 5.5. A second key result is that adaptation of the experiment will allow the measurement of dye concentration at the boundary of the film, while simultaneously measuring the total amount dye in the film. The initial findings have been published in the Journal of Physical Chemistry C [73]. Detailed information on the experimental techniques can be found in the thesis by Peic [85].

In the next section 5.1 other similar techniques to OWS are reviewed for comparison in order to justify the need for more sophisticated dye sensing techniques. OWS itself is described in detail in section 5.2. The physics of waveguides is described in section 5.3 and a model of dye diffusion and adsorption is presented in 5.5. Section 5.4 relates the concentration of dye within the film to the refractive index of the combination of dye, solvent and porous TiO_2. Using these models the whole system is simulated and some basic tests of the model are presented in section 5.6. Results are presented in section 5.7.

5.1 Dye Adsorption Experiments

In this section various existing methods of exploring dye diffusion and coverage will be reviewed. It will become apparent that these techniques either measure the total amount of dye within the film or the amount of dye at one very specific place (such as on a particular surface) but not both at the same time.

5.1.1 UV-Vis Spectroscopy

UV-Vis spectroscopy is the simplest of most longstanding method of analysis. The basic set up is shown in figure 5.2 [85, 83, 84, 86, 87]. The TiO_2 film is

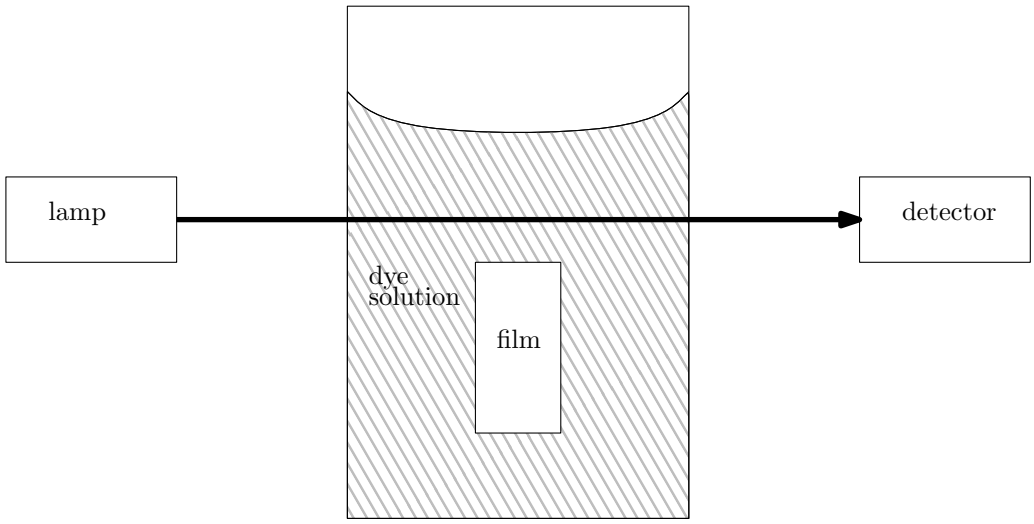

Figure 5.2: UV-Visible spectroscopy. The change in the fraction of light absorbed by the dye is used to infer the amount of dye in the film.

placed in a cuvette with dye solution. The degree of light adsorption through the solution is recorded as a function of time. Any decrease in dye concentration in solution is inferred to be due to an increase in dye concentration in the film. Through careful calibration the concentration of dye in solution can be related to the opacity of the solution. Clearly, this is an indirect method for measuring dye uptake and only the total amount of dye in the film can be deduced. A major shortcoming of this method is that at high concentrations dye tends to aggregate in the bottom of the cuvette, giving the illusion that it has entered the film. For example, the aggregation will occur in 0.3m mol dm^{-3} dye in ethanol solution which is a typical solution used to dye films. Little or no information about diffusion or about the position of dye within the film is gained, especially as the dye concentration is not comparable with the normal dying process. UV-Vis spectroscopy can be used to measure material properties of dyed TiO_2 films such as the refractive index or optical absorption coefficient, but only at low concentrations of dye. In addition the maximum density of dye molecules in the film Γ_m and ratio of the dye absorption to desorption rates K can be calculated. The determination of these constants will be revisited when the mathematical model of OWS is described. More details of UV-Vis spectroscopy can be found in the thesis by Peic [85].

5.1.2 Desorption Methods

In addition to UV-Vis spectroscopy, desorption methods are the second common method of measuring total dye adsorption [88]. A dyed film is placed into a basic solution (usually KOH) thus removing dye from the film. UV-Vis spectroscopy can then be used to measure the amount of dye desorbed from the film. As with UV-Visible spectroscopy this reveals the total amount of dye in the film but no spatial information. Desorption methods provide information similar to UV-Vis Spectroscopy. Piec compared both methods in order to check the results [85].

5.1.3 Photographic Method

Photographic methods have been reported in 2011 by Watson *et al.* [89] and again in 2012 by O'Regan *et al.* [90]. Dye is allowed to diffuse into one side of the film and at the far side a series of digital photographs are used to monitor how much dye has crossed the film. Through careful calibration this method can make quantitative measurements of the amount of dye that has crossed the film. The main result is that there appears to be a rapid initial uptake of dye followed by a second slower regime. There has been some conjecture that this may be due to additional layers of dye binding beyond one monolayer, or it may be due to paths through the film becoming blocked. Again these questions cannot be resolved easily since there is still little information available about the distribution of dye through the film. Watson *et al.* observed an initial rapid uptake of dye for 2h and then slow changes for another 16h using a 9μm film and a 0.3 m mol dm^{-3} dye bath. The study by O'Regan *et al.* focused on the consequences for electron transport and is less relevant to this chapter.

5.1.4 Indirect Nano Plasmonic Sensing (INPS)

Indirect nano plasmonic sensing (INPS) uses the resonance of gold nanoparticle discs (110nm $\times$ 20nm on average) embedded at the TiO_2 glass interface to detect the presence of dye as pictured in figure 5.3 [91]. Dye is introduced such that the dye must cross the film before approaching the nanoparticles. When dye approaches within $\sim$ 70nm of the nanoparticles they absorb light at 792nm. This

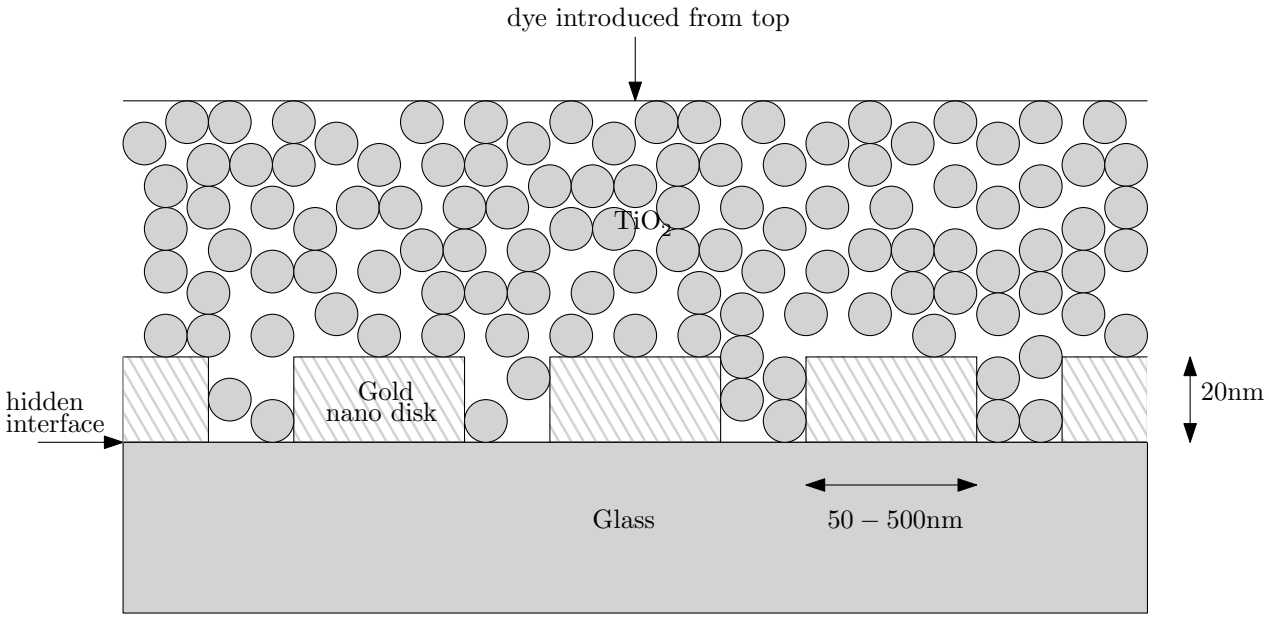

Figure 5.3: Diagram of the INPS method. Optical resonance of the gold nano discs causes light adsorption at 792nm.

gives a good indication of the presence of dye at the glass interface however, it gives little information about how much dye is at the interface or the amount of dye anywhere else within the film. The result has been interpreted by assuming a sharp diffusion front traveling across the 10μm film in time scales less than two hours, however, there seems to be little evidence that such a diffusion front exists. The result is in stark contrast to the photographic results by Watson [89], which is surprising, given both studies used a 0.3 m mol dm^{-3} dye bath, the thickness of the films only differ by 1μm.

5.2 Optical Waveguide Spectroscopy (OWS)

Section 5.1 showed that several methods are available for investigating dye application, however, they either measure concentration at the substrate or the concentration averaged over the whole film. This is not sufficient to answer questions such as: is transport limited by diffusion or adsorption? and is more dye at the surface of the film than at the center. The ultimate goal of this work was to ascertain if a new method, optical waveguide spectroscopy, can answer these questions using a computer simulation. This section will describe the OWS method in preparation for the following sections where a mathematical model of

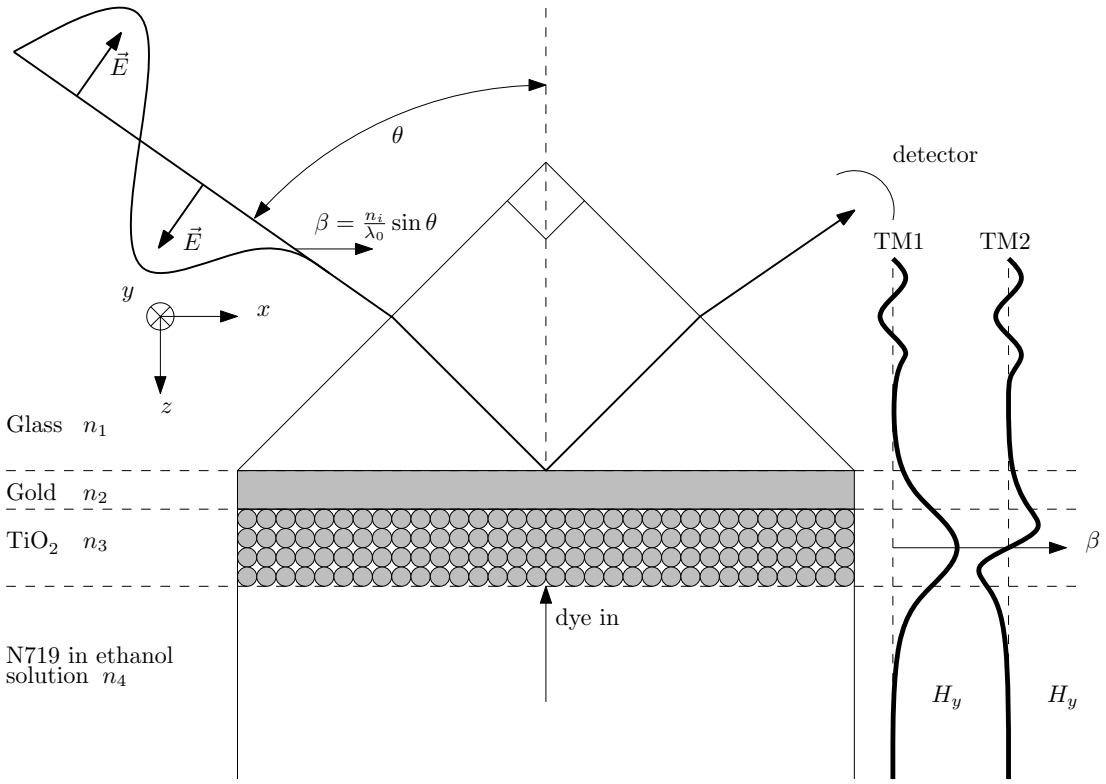

Figure 5.4: The basic layout of an OWS experiment for the case of TM modes (p-polorised light). The thick black lines show the profile of the magnetic field in the y-direction which is continuous. The modes have momentum β in the x-direction excited by light incident at angle θ and wavelength λ_0.

OWS will be presented. OWS has already been demonstrated as a technique for studying adsorption of proteins inside porous materials [92]. In this context the OWS technique is used to sense the position of dye within the cell, specifically ruthenium 535-bisTBA (N719) dye molecules.

The basic form of an OWS experiment is shown in figure 5.4. The TiO_2 photoanode is used as a planar waveguide stack. The experiment is very similar to a surface plasmon resonance (SPR) experiment in the Kretschmann configuration. Critically, the high refractive index TiO_2 film sits between a thin low refractive index gold film and a dye solution such that

$$n_3 > n_2 \text{ and } n_3 > n_4. \tag{5.1}$$

See table 5.1 for the refractive index of each layer. This satisfies the criteria for optical guided modes propagating in the TiO_2 film and forms a 2D planar waveguide. Modes are excited in the guiding structure using prism coupling of incident light with wavelength λ_0. Higher order modes can be excited by changing

Table 5.1: The refractive index and thickness of each layer in the wave guiding stack at 632.8nm provided by A. Peic [85]. The change in κ is small because N719 is almost transparent at 632.8nm. This prevents photobleaching.

	layer	thickness(nm)	n	κ
1	prism	∞	1.84498	0
2	gold	35.824	0.312	3.823
3	TiO_2 film (no dye)	1269.89	1.7942	0.0055
	TiO_2 film (with dye)	1269.89	1.8192	0.0075
			$\Delta n = 0.0245$	$\Delta k = 0.002$
4	ethanol	∞	1.3592	0

the incident angle θ of the beam (a $\lambda_0 = 632.8$nm HeNe laser). A polariser is used so that either transverse magnetic (TM) or transverse electric (TE) plane waves can be selected. Figure 5.4 shows the set up for p-polorised incident light resulting in TM modes where the magnetic field is always pointing in the $\pm$ y-direction. It is just as reasonable to perform the experiment with s-polarised light resulting in TE modes where the electric field is always pointing in the $\pm$ y-direction. The magnetic susceptibility of all of these materials is very small and can be ignored.

When dye enters the TiO_2 film the refractive index of the layer changes. Figure 5.5 shows typical OWS data at fixed times before and after the application of dye. The TE4, TE3 and TE2 modes are visible. As angle θ is changed, the intensity of light arriving at the detector changes dramatically. Each drop in intensity corresponds to an excited mode in the film. The 0.0245 change in refractive index of the film has caused each of the modes to shift by approximately $\Delta\theta \approx +2.5^\circ$ and the minimum reflected intensity (divided by incident intensity) has increased by $\Delta R \approx 0.1$.

Over a period of around 24 hours dye diffuses into the film and the position of each mode gradually changes with the presence of more and more dye. Figure 5.6 shows the position and the reflectivity of the TM4 mode tracked over time. It will be shown that the shift in the position of the mode is proportional to the amount of dye in the film. The plot shows a very rapid initial change in the position of the TM4 mode followed by a second regime with slow changes which show no sign of stopping after 20 hours. The result is similar to the photographic method by Watson except changes are observed well beyond 16h. The films used in the photographic method were 9µm thick, 1µm less than the 10µm OWS films. The dye baths were both at the same concentration. It is important to remember that the photographic method measured the concentration at the rear TiO_2 surface but

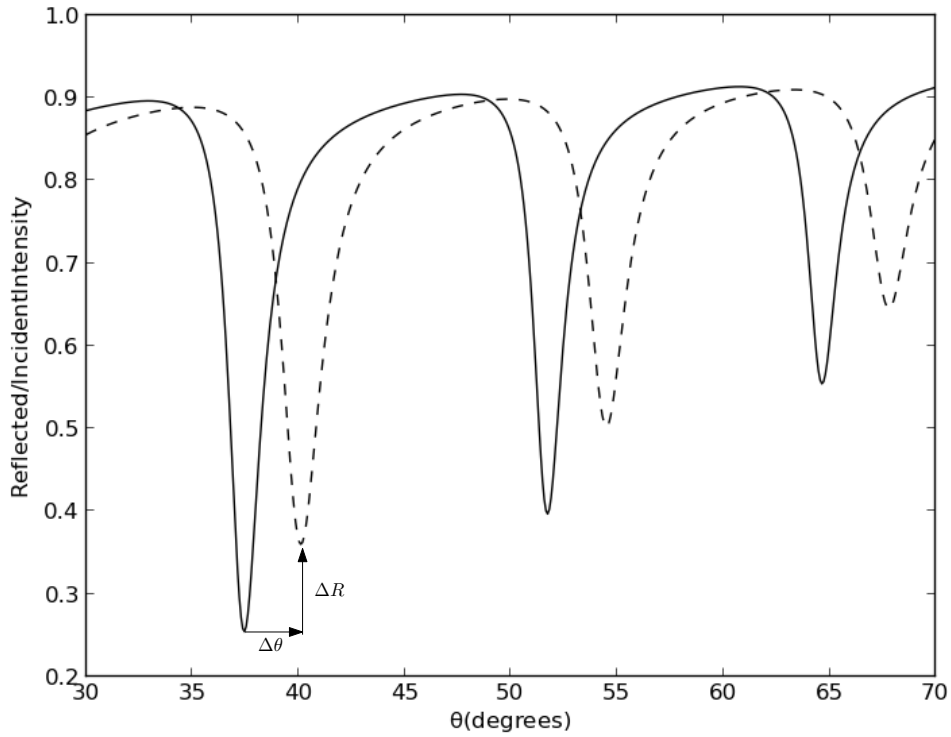

Figure 5.5: Typical signal recived by the detector in an OWS experiment before (solid line) and after (dashed line) the application of dye. Generated using the optical model in section 5.3 using the values in table 5.1.

the OWS experiment is sensitive to the whole film. It is interesting to speculate as to why the two results may differ. For instance, this could be explained by dye diffusing through large channels in the film and then smaller ones which may not penetrate through the whole film. These kinds of conclusions rely on an intuition about a system which is complex with many interacting elements. By modelling the system one can produce results to show exactly what one might expect if, for example, diffusion is rapid and adsorption is slow. These models can then be a useful point of comparison when interpreting experimental data.

In order to build a numerical model of an OWS experiment the physics of a planar waveguide stack will be used. This is described in the next section 5.3.

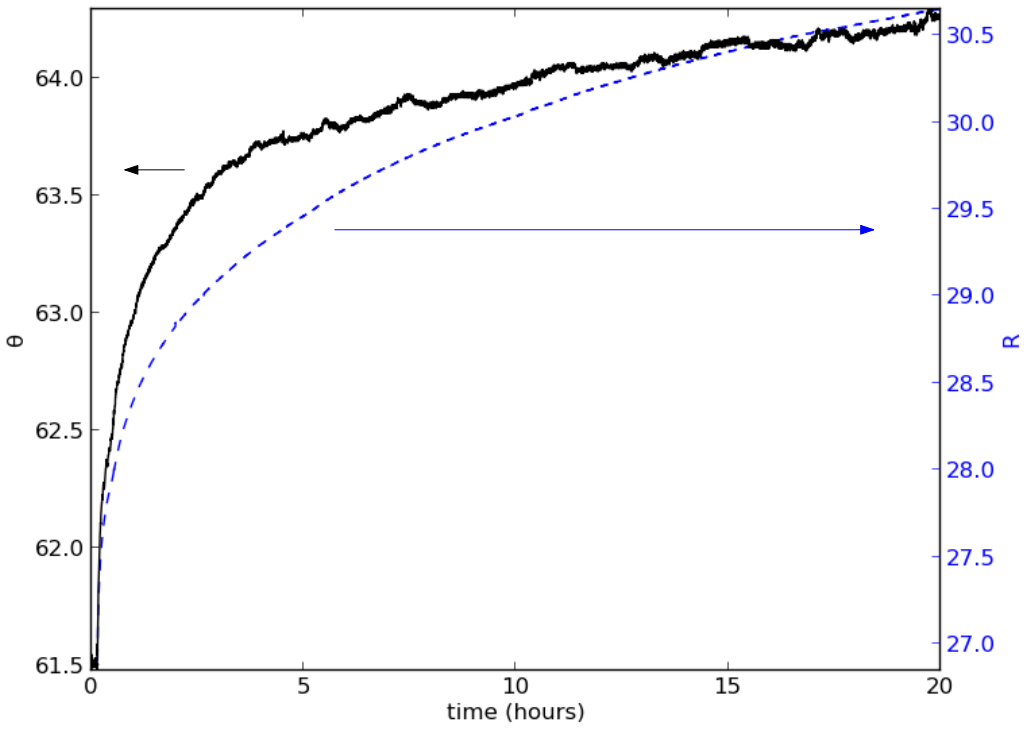

Figure 5.6: The shift in position of the TM4 mode once dye is flowed over the exposed TiO_2 surface used a 0.3 m mol dm^{-3} dye bath and 10µm film. Experimantal data taken by A. Peic [85].

5.3 The Optical Model

In this section a model of the OWS experiment is formulated. Firstly, it is helpful to clarify the concept of the refractive index and how they relate to the material properties of materials, namely the electric permittivity.

5.3.1 Material Properties

The refractive index is the ratio of the speed of light in a vacuum to the speed of light in some optical medium. By rearranging Maxwell's equations it can be seen that the refractive index is related to the relative electric permittivity ϵ_r and relative magnetic permeability μ_r by

$$n = \sqrt{\epsilon_r \mu_r}. \tag{5.2}$$

For all materials concerned with this chapter

$$\mu_r = 1. \tag{5.3}$$

For lossy materials where photons are adsorbed by the material along the optical path a loss term κ can be included in the refractive index so that the complex refractive index $\widetilde{n}$ is given by

$$\widetilde{n} = n + i\kappa \tag{5.4}$$

where $i = \sqrt{-1}$.

κ is related to the cross section σ of N absorbers per unit volume

$$\kappa = \frac{\sigma N \lambda_0}{4\pi} \tag{5.5}$$

where N and σ may be calculated from UV-Vis spectroscopy.

For an electromagnetic wave traveling in free space in the x-direction with wavelength λ_0 and angular frequency ω the electric field ψ will be the following function of time t and position x with amplitude A

$$\psi(x,t) = A\exp\left(i\left[k_x x - \omega t\right]\right) \tag{5.6}$$

where wavenumber $k_x = \widetilde{n}/\lambda_0$. Substituting $\widetilde{n}$ into equation 5.6 one can see that the real part of the complex refractive index describes the spacial periodicity of the wave and the imaginary part controls the rate of exponential decay of the amplitude in the x-direction

$$\psi(x,t) = A\exp\left(i\left[\frac{n}{\lambda_0}x - \omega t\right]\right)\exp\left(-\kappa x\right). \tag{5.7}$$

The thickness and refractive index of all the materials in the waveguide stack are included in table 5.1.

5.3.2 The Waveguide Equations

For TE modes and for each layer i the transverse electric field must satisfy [93, 94]

$$\frac{d^2E_y}{dx^2} + \left(n_i^2k_0^2 - \beta^2\right)E_y = 0 \tag{5.8}$$

where

$$\beta = \frac{n_i}{\lambda_0}\sin\theta \tag{5.9}$$

is the the component of the wavevector in the x direction. The magnetic field components are functions of E_y

$$H_x = -\frac{\beta}{\omega\mu_0}E_y \tag{5.10}$$

and

$$H_z = -\frac{1}{i\omega\mu_0}\frac{\partial E_y}{\partial z} \tag{5.11}$$

For TM modes

$$\frac{d^2H_y}{dx^2} + \left(n_i^2k_0^2 - \beta^2\right)H_y = 0 \tag{5.12}$$

where

$$E_x = \frac{\beta}{\omega\epsilon}H_y \tag{5.13}$$

and

$$E_z = \frac{i}{\omega\epsilon}\frac{\partial H_y}{\partial z}. \tag{5.14}$$

The fields must all be continuous. The gradient of the transverse fields in the y-direction must also be continuous otherwise E_z will be discontinuous. E_y and H_y can be solved for using the transfer-matrix formalism for planar waveguide stacks as presented by Chilwell and Hodgkinson and described in the next two subsections for completeness [94].

The transfer matrix for TE modes

In each layer of constant refractive index equation 5.6 is a valid trial solution. For a layer i of thickness d_i the condition for continuous fields requires that the

amplitude of forward travelling waves, A_i, and backward travelling waves, B_i, must be related to layer $i+1$ by

$$A_i + B_i = A_{i+1} \exp(\alpha_{i+1} d_{i+1}) + B_{i+1} \exp(-\alpha_{i+1} d_{i+1}). \tag{5.15}$$

where

$$\alpha_i = \sqrt{k_0^2 n_i^2 - \beta^2} \tag{5.16}$$

The condition for constant gradient of transverse fields requires that

$$\alpha_i A_i - \alpha_i B_i = A_{i+1}\alpha_{i+1} \exp(\alpha_{i+1} d_{i+1}) + B_{i+1}\alpha_{i+1} \exp(-\alpha_{i+1} d_{i+1}). \tag{5.17}$$

These two conditions can be written in matrix form as [93, 94]

$$\begin{bmatrix} A_i \\ B_i \end{bmatrix} = \mathbf{M}_{i,TE} \begin{bmatrix} A_{i+1} \\ B_{i+1} \end{bmatrix} \tag{5.18}$$

and

$$\mathbf{M}_{i,TE} = \frac{1}{2} \begin{bmatrix} \left(1 + \frac{\alpha_{i+1}}{\alpha_i}\right) \exp(-\alpha_{i+1} d_{i+1}) & \left(1 - \frac{\alpha_{i+1}}{\alpha_i}\right) \exp(-\alpha_{i+1} d_{i+1}) \\ \left(1 - \frac{\alpha_{i+1}}{\alpha_i}\right) \exp(\alpha_{i+1} d_{i+1}) & \left(1 + \frac{\alpha_{i+1}}{\alpha_i}\right) \exp(\alpha_{i+1} d_{i+1}) \end{bmatrix} \tag{5.19}$$

The transfer matrix for TM modes

For TM modes the condition for continuous fields is the same as equation 5.15. However, the condition for the derivative of the transverse field is now

$$\frac{\alpha_i A_i}{n_i^2} - \frac{\alpha_i B_i}{n_i^2} = \frac{A_{i+1}\alpha_{i+1}}{n_{i+1}^2} \exp(\alpha_{i+1} d_{i+1}) + \frac{B_{i+1}\alpha_{i+1}}{n_{i+1}^2} \exp(-\alpha_{i+1} d_{i+1}). \tag{5.20}$$

since

$$E_z = \frac{i}{\omega\epsilon} \frac{\delta H_y}{\delta z} \tag{5.21}$$

must be continuous. Hence, $\mathbf{M}_{i.TM}$ is given by [93, 94]

$$\mathbf{M}_{i.TM} = \frac{1}{2}\begin{bmatrix} \left(1+\frac{n_i^2\alpha_{i+1}}{n_{i+1}^2\alpha_i}\right)\exp\left(-\alpha_{i+1}d_{i+1}\right) & \left(1-\frac{n_i^2\alpha_{i+1}}{n_{i+1}^2\alpha_i}\right)\exp\left(-\alpha_{i+1}d_{i+1}\right) \\ \left(1-\frac{n_i^2\alpha_{i+1}}{n_{i+1}^2\alpha_i}\right)\exp\left(\alpha_{i+1}d_{i+1}\right) & \left(1+\frac{n_i^2\alpha_{i+1}}{n_{i+1}^2\alpha_i}\right)\exp\left(\alpha_{i+1}d_{i+1}\right) \end{bmatrix}. \tag{5.22}$$

Calculating the reflectance of the stack

In the final layer of the waveguide stack (dye dissolved in ethanol) there can only be forward traveling waves because there are no further interfaces. So,

$$\begin{bmatrix} A_4 \\ B_4 \end{bmatrix} = \begin{bmatrix} 1 \\ 0 \end{bmatrix}. \tag{5.23}$$

The field in the prism can then be calculated by summing the transfer matrix for each individual layer. For instance, in the prism

$$\begin{bmatrix} A_1 \\ B_1 \end{bmatrix} = \sum_{i=1}^{2} \mathbf{M}_{i,TE/TM} \times \begin{bmatrix} 1 \\ 0 \end{bmatrix}. \tag{5.24}$$

Once the amplitudes A and B are known for each layer the power being reflected off the stack is given by Poynting's vector which is the vector product of the magnetic and electric fields

$$\vec{S} = \vec{E} \times \vec{H}. \tag{5.25}$$

The optical model shows how to calculate the reflectance of a stack given a thickness and a complex refractive index for each layer. Next, the complex refractive index of each layer needs to be assigned depending on the concentration of dye at each point.

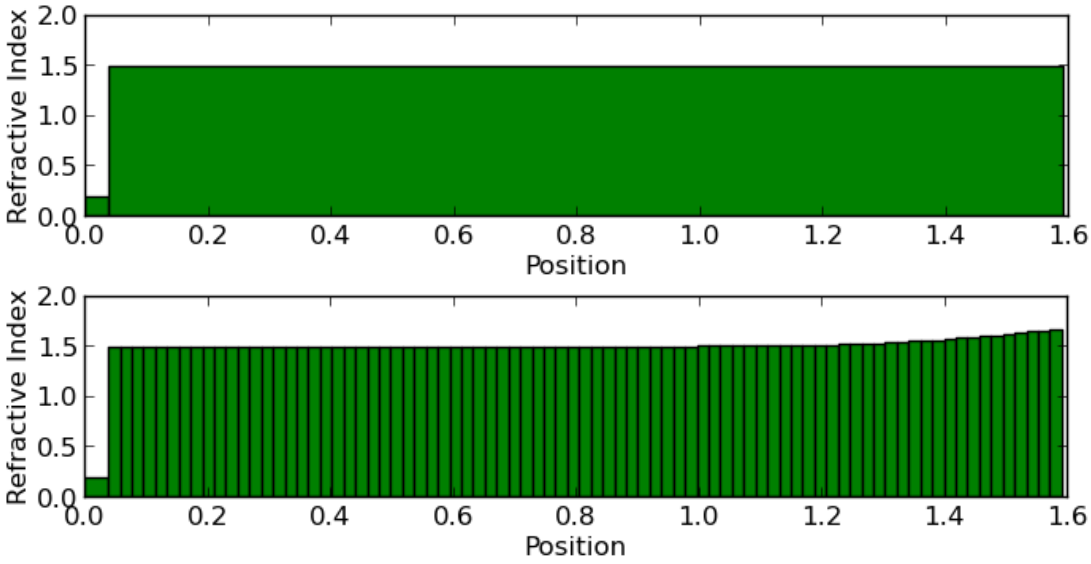

Figure 5.7: Top: Plot of the refractive index profile of the gold and TiO_2 layers before the application of dye. Bottom: After the application of dye the refractive index profile is approximated by dividing the TiO_2 film into many small layers of constant refractive index.

5.4 The refractive index model

Section 5.3 demonstrated how to calculate the reflectance of a planar waveguide stack with layers of constant refractive index. In practice, the OWS experiment has a layer of porous TiO_2 filled with an unknown profile of dye within it. It will be necessary to calculate the reflectance for any such profile of dye concentration. A continuous distribution of dye can be approximated by dividing the TiO_2 layer into many small individual layers each with a constant refractive index as in figure 5.7. This section covers how the refractive index of each layer with a concentration of dye, c is assigned.

It has been observed that the refractive index of N719 dye in ethanol is proportional to the concentration of dye by Peic [85]. The effective refractive index n_{eff} of the (approximately 50:50) mixture of dye and TiO_2 is calculated using Bruggeman's equation [95]

$$\frac{1}{2}\frac{\epsilon_1 - \epsilon_{eff}}{\epsilon_1 + 2\epsilon_{eff}} + \frac{1}{2}\frac{\epsilon_2 - \epsilon_{eff}}{\epsilon_2 + 2\epsilon_{eff}} = 0 \tag{5.26}$$

where the 50 : 50 mixture of materials 1 and 2 have dielectric constant ϵ_1 and

ϵ_2 [95, 96].

Figure 5.8 shows n_{eff} given by equation 5.26 where $\epsilon_1 = \sqrt{n_1} = \sqrt{2.57}$, the refractive index of anatase TiO_2. $\epsilon_2 = \sqrt{n_2}$ is varied between the refractive index for dyed and un-dyed films (between the vertical dashed lines). For such small changes in ϵ_2 there is a linear relationship between the refractive index of the solution n_2 and n_{eff}. Hence the relationship between the concentration of dye and the refractive index of the whole film is likely linear. Using the values listed in table 5.1 for an undyed film and a completely dyed film ($n = 1.7942$ and $n = 1.8192$ respectively and both marked with vertical dashed lines on figure 5.8) the following relation between refractive index and concentration was used for 0.5 m mol dm^{-3} N719 dye solution

$$n_{eff}(x,t) = 1.7942 + (1.8192 - 1.7942)\left(\frac{c(x,t)}{0.3}\right). \tag{5.27}$$

c is the concentration of dye with units m mol dm^{-3}. According to equation 5.5 the relationship between κ and the concentration c should also be linear.

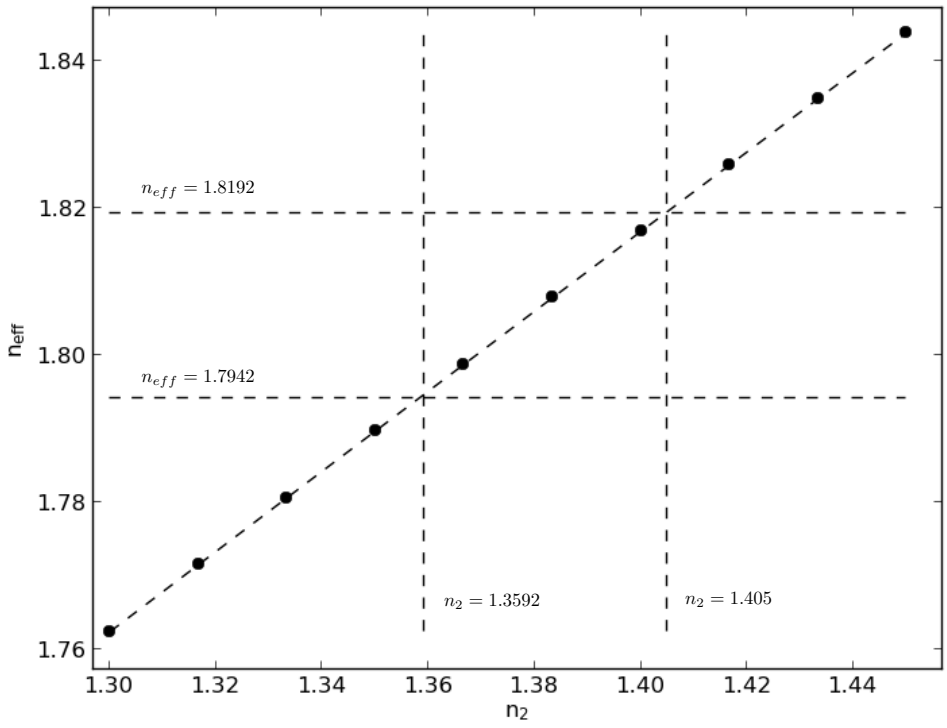

Figure 5.8: Solution to Bruggeman's equation (equation 5.26), $\sqrt{n_1} = \sqrt{2.57}$.

The rate of change in the refractive index of N719 dye in ethanol solution with respect to concentration, dn/dc, has been measured for low dye concentrations between 0.2 and 1.2 m mol dm^{-3}[73] and is linear

$$dn/dc = 0.238 \text{ dm}^{-3}/\text{mol}. \tag{5.28}$$

The use of Bruggeman's equation (5.26) ought to be a temporary measure as it should be possible to measure the refractive index of a set of films each in a solution with a different dye concentration. This would then provide a calibration curve which would relate dye concentration to refractive index.

The final step in making a complete OWS model is calculating how dye may diffuse and bind to the film as a function of position and time. If this is known, then the tools have been already presented to calculate the refractive index of each region and the reflectance at any given incident angle of the laser.

5.5 The Diffusion-Adsorption Model

The refractive index of each layer is assigned using the diffusion-adsorption model. The task at hand is two fold. The evolution of the dye concentration in solution as a function of position and time must be calculated. The evolution of the dye concentration on the TiO_2 surface must also be calculated as a function of position and time. Langmuir like behavior has been observed by Peic for low concentration of N719 dye and by Nazeeruddin using N3 dye on TiO_2 films using UV-Vis spectroscopy [73] [97]. In the next subsection the mathematics of Langmuir adsorption is described then in the following section this is included in the diffusion equation as a loss term to describe diffusing dye with Langmuir adsorption.

Table 5.2: Equilibrium constants and density of binding sites measured for N179 [73] and N3 dye [97].

Dye	K (dm^3/mol)	Γ_m (mol dm^{-3})
N719	2×10^4	0.247
N3	1×10^5	0.15

5.5.1 Langmuir Adsorption

Picture that the film consists of a certain number of binding sites Γ_m, of which Γ are occupied by dye molecules

$$\theta = \frac{\Gamma}{\Gamma_m}. \tag{5.29}$$

Then assume that the rate of dye molecules becoming bound to the surface is proportional to the number of vacant bind sites

$$\frac{d\theta}{dt} = k_a c \Gamma_m (1 - \theta) \tag{5.30}$$

where k_a is a constant of proportionality. Then assume that the rate of dye molecules becoming unbound is proportional to the number of occupied binding sites

$$\frac{d\theta}{dt} = k_d \Gamma_m \theta \tag{5.31}$$

where k_d is a second constant of proportionality. If one assumes that locally a state of quasi-equilibrium exists between dye bound to the surface and dye free from the surface, or symbolically

$$\frac{d\theta}{dt}, \tag{5.32}$$

then the preceding equation can be rearranged to arrive at the result

$$\theta = \frac{Kc}{1 + Kc} \tag{5.33}$$

where θ is a function of concentration of unbound dye c and $K = k_a/k_d$.

Measurements by Peic for low concentration of N719 dye and by Nazeeruddin using low concentrations N3 dye on TiO_2 films give similar results for the Langmuir parameters listed in table 5.2 [73] [97].

5.5.2 Diffusion with Langmuir Adsorption

The time evolution of concentration c is given by including this Langmuir adsorption behaviour as a loss term in the diffusion equation. This is a standard textbook result (e.g. Crank [98]).

$$\frac{\partial c\left(x,t\right)}{\partial t} = D_0 \frac{\partial^2 c\left(x,t\right)}{\partial x^2} - \frac{K\Gamma_m}{\left(1 - Kc\left(x,t\right)\right)^2} \frac{\partial c\left(x,t\right)}{\partial t} \tag{5.34}$$

Often, conceptually, this is thought of as a concentration dependent diffusion coefficient although care must be taken since the divergence of this term must be included to describe a true system with a concentration dependent diffusion coefficient.

$$\frac{\partial c\left(x,t\right)}{\partial t} = \frac{D_0}{\left(1 + \frac{K\Gamma_m}{\left(1 - Kc(x,t)^2\right)}\right)} \frac{\partial^2 c\left(x,t\right)}{\partial x^2} \neq \frac{\partial}{\partial x}\left(D\left(x\right) \frac{\partial c\left(x,t\right)}{\partial x}\right) \tag{5.35}$$

The total concentration of bound and unbound dye is

$$c_{tot}\left(x,t\right) = c\left(x,t\right)\left(1 + \frac{\Gamma_m K}{1 + Kc\left(x,t\right)}\right). \tag{5.36}$$

This can be solved by finite differencing using the same techniques in chapter 3.

5.6 Testing and Fitting

The optical model can be tested by comparing the results to existing software. The available existing software (Winspall) can only handle a small number of (< 8) manually assigned layers of different refractive index. Figure 5.9 shows the fit of the film using Winspall and the fit using code written for this chapter. The two data sets are exactly the same.

Manually fitting the film is extremely time consuming and often leads to a poor fit since a three dimensional parameter space often needs to be explored (film thickness, real and complex refractive index). As an experiment, the down hill simplex method was used to try and fit experimental data automatically. As a

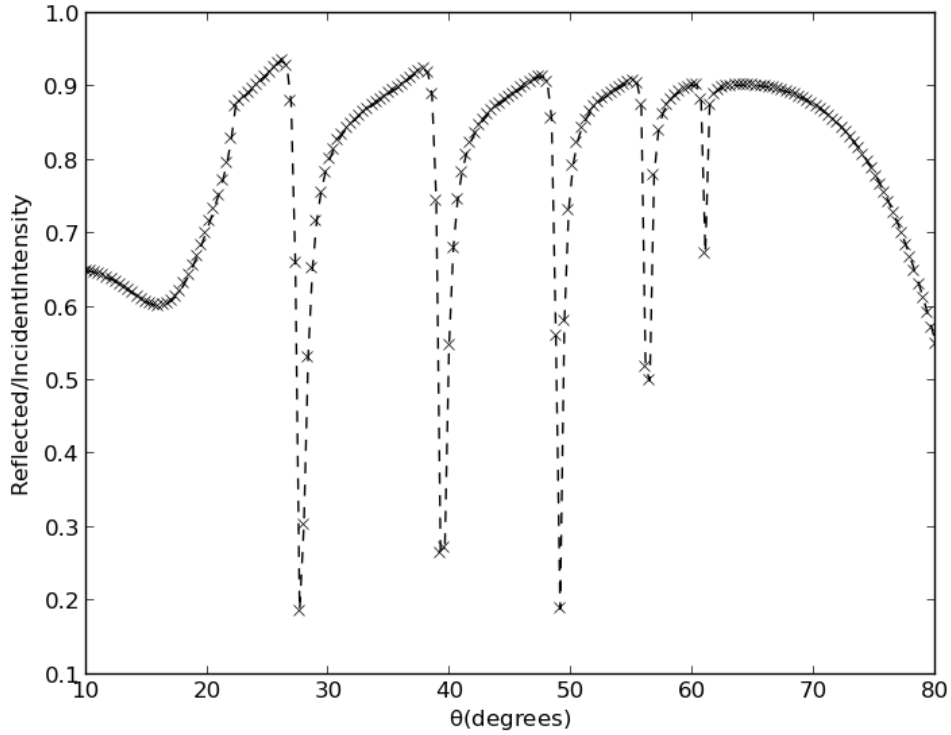

Figure 5.9: Spectra predicted by Winspall (dashed line) and the opical model (section 5.3) (crosses). The plot simulates a TiO_2 film in air. All values as in table 5.1 except for layer 3 $n = 1.5, \kappa = 5 \times 10^{-5}$ and for layer 4 $n = 1, \kappa = 0$. Thickness of the film was set to 1.518.

test case, film with no dye, in air (rather that ethanol), was chosen since it is reasonable to assume that the refractive index should be constant across the film. Figure 5.10 is a fit using the downhill simplex method. Figure 5.9 is in fact a manual fitting of the same film used for the automatic fitting in figure 5.10 The two methods give very similar film properties for the refractive index of the film, $n = 1.5$ and $n = 1.498$ and the film thickness $d = 1.518\mu$m and $d = 1.534\mu$m.

Fitting using the simplex method is a useful way of finding the thickness of a film. In figure 5.11 the same film has been fitted using one spectra in air and a second spectra in ethanol. The automated fitting identifies the thickness of the film (approximately 1.5µm in both cases) with a consistency down to $\pm 0.01\mu$m.

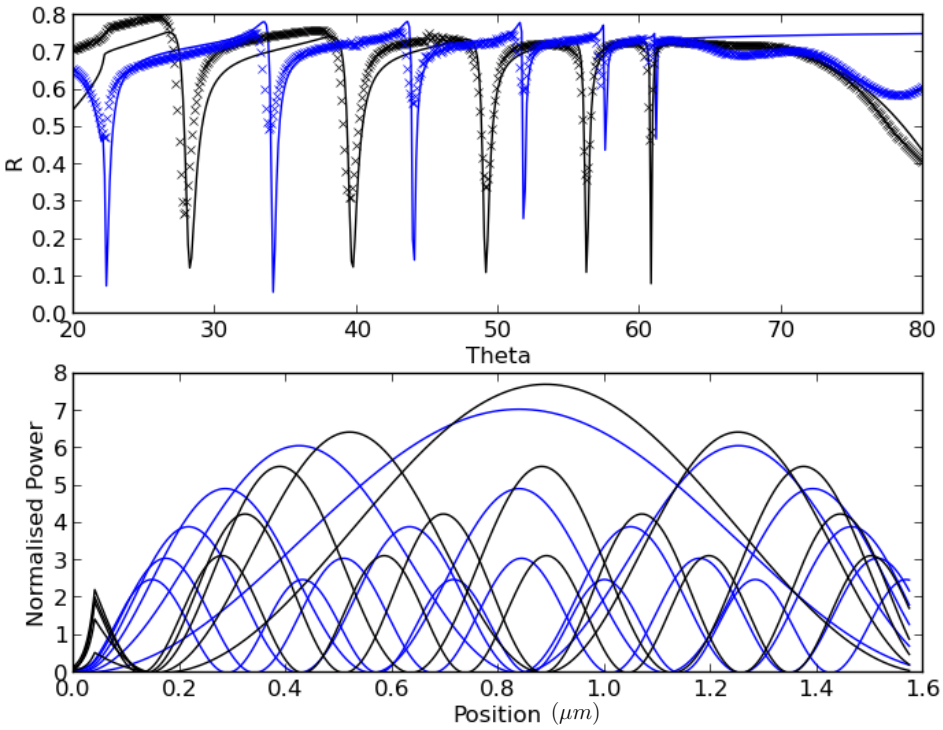

Figure 5.10: Fit for a TiO_2 film in air with no dye, experimental results crosses, optical model solid lines (top plot). Values have been determined using the optical model in section 5.3 and the downhill simplex method. For layer 3 $n = 1.498, \kappa = 0.00679$ and for layer 4 $n = 1$. The best fit for the thickness of the TiO_2 film was 1.534µm. In the lower plot the modes are plotted, each has been normalised so that they are all visable on the same scale. TE thin blue, TM thick black.

5.7 Results

The results section is ordered as followed. First the shift in the TM4 mode is simulated for very rapid and very slow dye binding. These curves will be useful for analysing experimental data.

Next the OWS is used to show that the shift in the angle of resonance for a given mode is approximately proportional to the total amount of dye in the film. Then finally the model is used to demonstrate how a rutile prism may be used to excite a surface plasmon. The shift in the resonant angle for the surface plasmon is predicted to be proportional to the concentration of dye at the gold/TiO_2 interface.

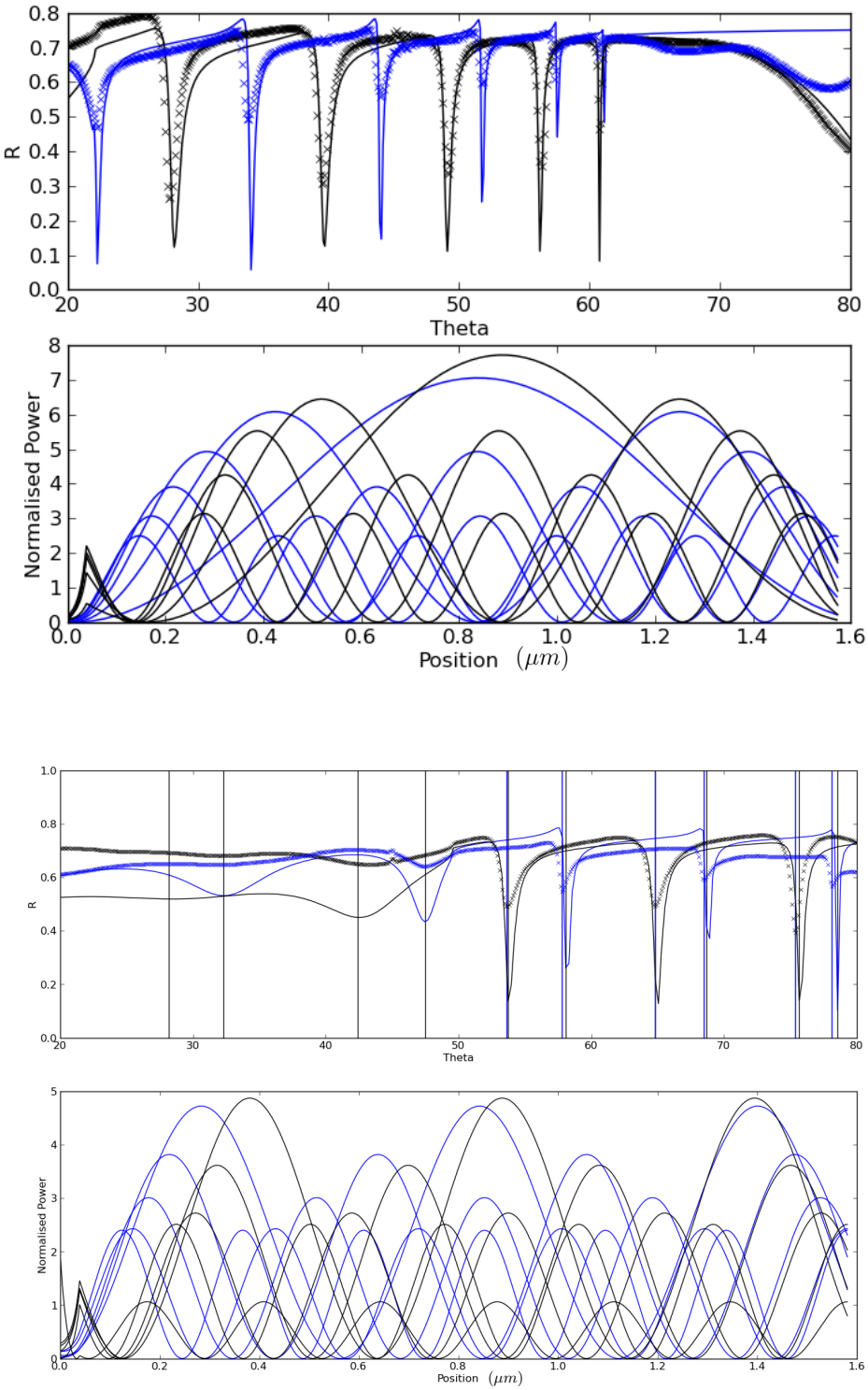

Figure 5.11: Fits (lines) to experimental data (crosses) using the downhill simplex method for the same film in air (top, fitted film refractive index $n = 1.498$ and thickness $d = 1.53\mu m$) and ethanol (bottom, fitted film refractive index $n = 1.73$ and thickness $d = 1.54\mu m$) TM thick black, TE thin blue.

5.7.1 Kinetic Measurements

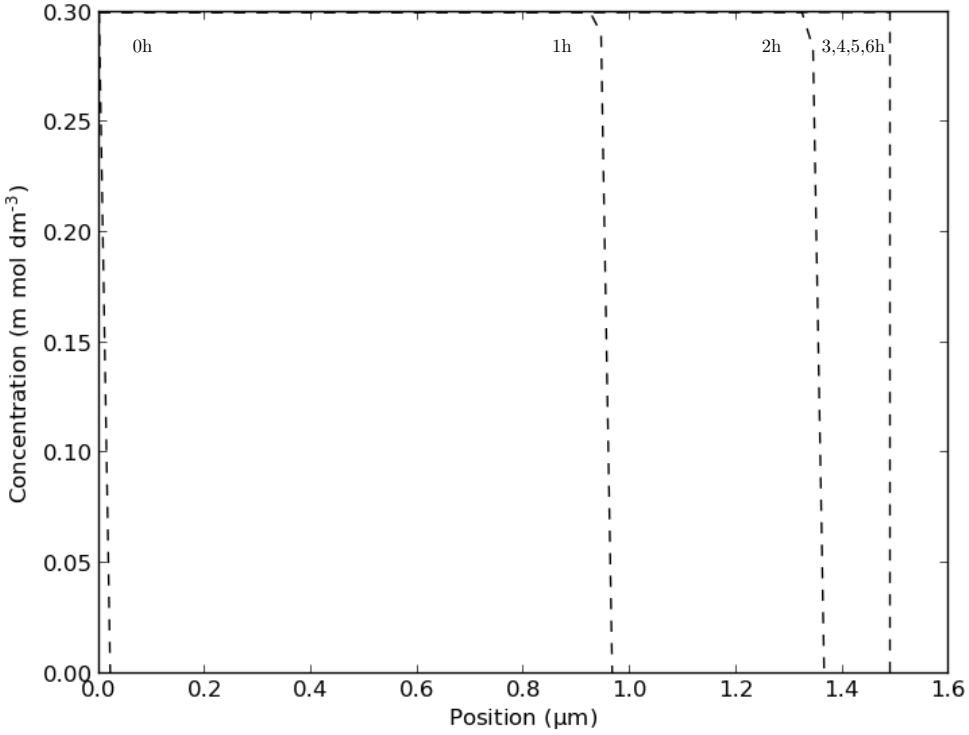

Figure 5.12: Solution to equation 5.34 approximating the concentration of $K = 1 \times 10^{10}$ dye through the film after each hour for a 1.552µm film. $D = 358\text{m}^2/\text{s}$, $\Gamma = 3$ m mol dm^{-3}. The concentration at the left hand side is fixed at 0.12 m mol dm^{-3}, zero flux at the right hand side. Solved on 70 internal points.

In this subsection the position of the TM4 mode over time is compared for the following two limits: extremely strong dye binding and extremely weak binding. The goal is to provide a point of reference so that experimental data can be compared to clear cut and well defined scenarios.

The position of the TM4 mode is simulated as a function of time by solving the diffusion absorption model (equation 5.34) with a very high equilibrium constant $K = 5 \times 10^{10}$. In other words, dye becomes bound to the film and never returns to solution. The profile of dye within the film as a function of position and time is shown in figure 5.12. Γ is set to 0.3 m mol dm^{-3} which is taken from values determined by unpublished UV-visible spectroscopy experiments and the concentration of the dye bath was set to 0.12 m mol dm^{-3}. This generates a diffusion front which travels through the film and any physical diffusion front is likely to behave in a similar way. Figure 5.14 shows both such results.

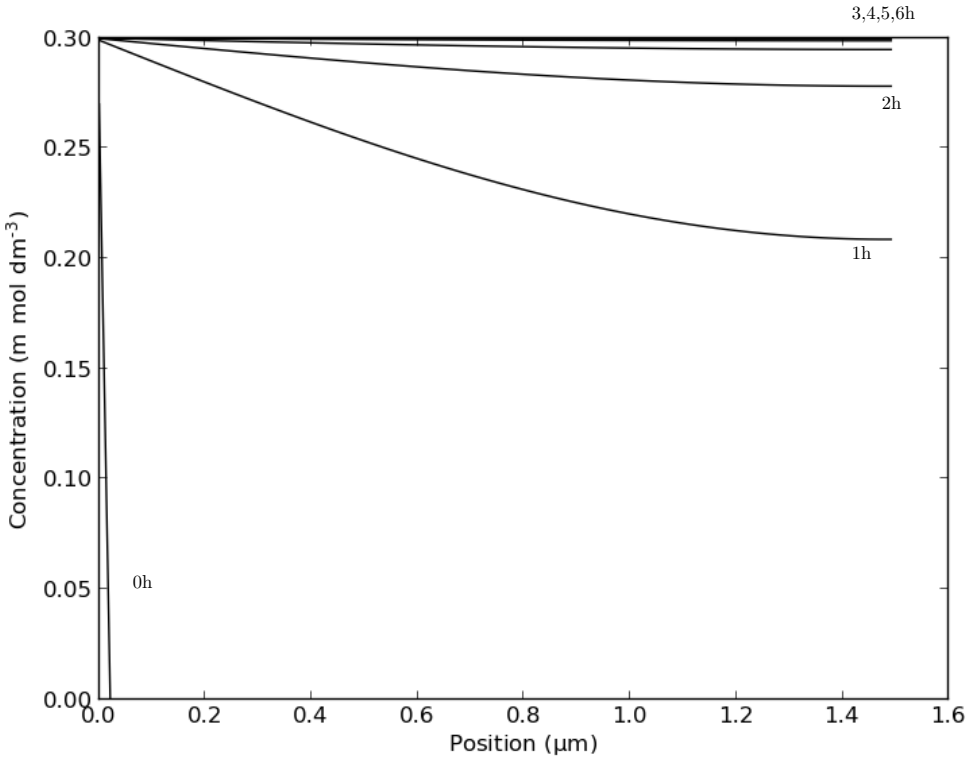

Figure 5.13: Solution to equation 5.34 approximating the concentration of $K = 0$ dye through the film after each hour for a 1.552µm film. $D = 358\text{m}^2/\text{s}$, $\Gamma = 0$. The concentration at the left hand side is fixed at 3 m mol dm^{-3}, zero flux at the right hand side. Solved on 70 internal points.

This simulation can be contrasted with the opposite case, where $K = 0$, also displayed in figure 5.14. Of course K is not zero in reality otherwise DSC's would not function, however, it is a well defined benchmark and weakly binding dye ought to tend towards this type of result. The concentration of the dye bath is set to Γ_m so that the films have the same refractive index before and after the application of dye. The profile of dye within the film as a function of position and time in this instance is shown in figure 5.12. In both cases the diffusion constant $D = 358$ m^2/s is exactly the same and the simulations reach the steady state after approximately 6 hours. For the purposes of demonstrating the difference between these two extremes the qualitative behaviour is not sensitive to the value of D. For the case of a diffusion front there is a clear change in gradient of the signal when the diffusion front reaches the gold layer. For diffusion like transport the curve is much smoother and much more similar to that seen experimentally in figure 5.6.

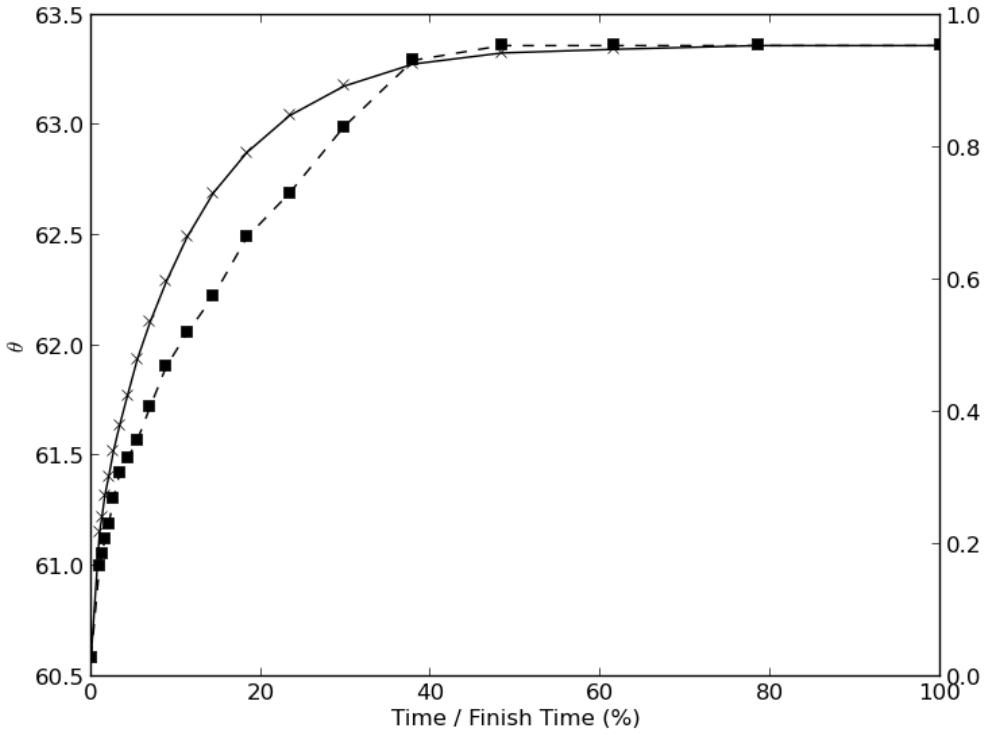

Figure 5.14: Simulated shifts in the TM4 mode for the case of a diffusion front ($K = 5 \times 10^{10}$, sqares) and pure diffusive behavior ($K = 0$) (crosses) produced using the optical model, the diffusion-adsorption model and the refractive index model. $D = 358$ m^2/s, dye bath concentration = 0.12 m mol dm^{-3}, $\Gamma_m = 0.3$ m mol dm^{-3}.

The very steep initial gradient followed by the slower shift in the signal as observed in experimental results is contrasted with a simulated fit in figure 5.15 using the values in table 5.2. Using the model, it is impossible to fit both the initial steep section of the experimental data and the following slow section. This led to conjecture suggesting that dye binding or dye diffusion may proceed over two or more stages. For example, the dye may diffuse initially through large pores in the film and then small pores, or some pores may become blocked in some way.

5.7.2 Spatial Resolution

In this section, the OWS model is used to show that to a good approximation the shift in any of the waveguide modes is proportional to the total amount of

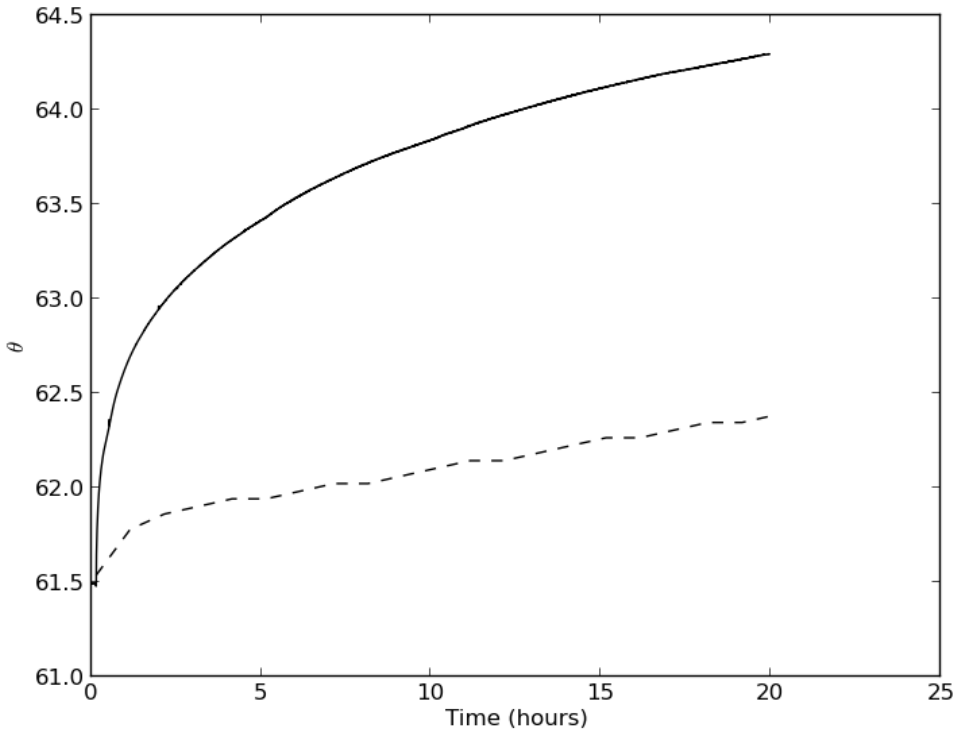

Figure 5.15: Simulated shifts in the TM4 mode for the case of a diffusion front $K = 5{\times}10^5$ (dashed line) produced using the optical model compared to the measured shift in the TM4 mode (solid line). $D = 1000$ m^2/s, dye bath concentration = 0.3 m mol dm^{-3}, $\Gamma_m = 0.247$ mol dm^{-3}.

dye in the film

$$\int_0^d c(x)\ dx. \tag{5.37}$$

An important objective of the OWS experiment is to produce a result that measures the profile of the dye within the film in addition to the total amount of dye present. In this section simulations are compared where the total amount of dye within the film is the same but the distribution of dye is different. Again, two completely contrasting cases are compared. In one extreme case there is no diffusion, the concentration of dye gradually increases uniformly across the whole film. In the second extreme, a sharp diffusion front progresses across the film, to the left of the front there is no dye, to the right there is the equilibrium concentration of dye. These two extremes are pictured in figure 5.1. By comparing the two cases against the total amount of dye in the film at each point an indication can be drawn about the degree of spatial information available from the

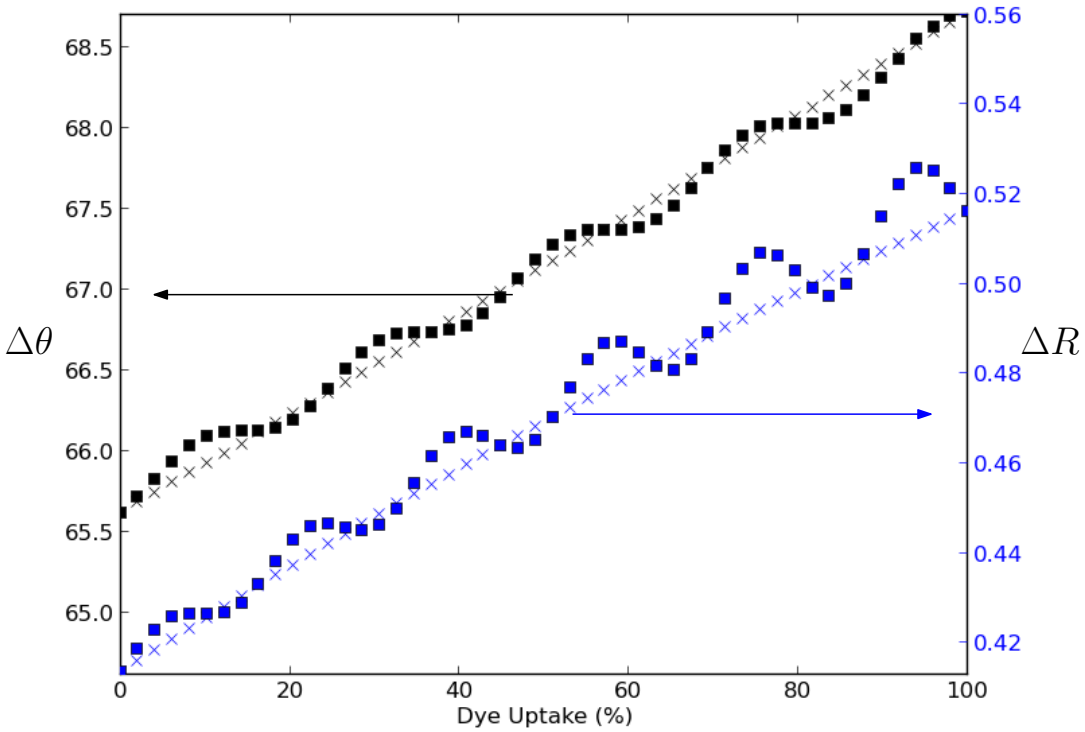

Figure 5.16: Shift in the TM4 mode for a sharp diffusion front (squares), and for a perfectly flat concentration (no positional dependence on concentration within the film), (crosses). $\Delta n = 0.0245$.

experiment and this is plotted in figure 5.16. The total before and after change in refractive index was set to 0.0245, the same as which has been observed experimentally [85]. Because two such simplistic cases are being compared there are no other parameters needed other than the refractive index of each material.

The solutions oscillate between being identical and differing by approximately one fifth of one degree and 2% greater reflectivity. Figure 5.16 suggests that it would be difficult to distinguish between the two dye distributions using only OWS. Although OWS is not strictly an integral method, spatial information would be difficult to extract from the experiment, but the total amount of dye in the film could be extracted very simply. The dyed section of the TiO_2 forms a waveguide in its own right and goes on and off resonance as the diffusion front moves through the film, hence the oscillations in figure 5.16.

5.7.3 Surface Plasmon Monitoring

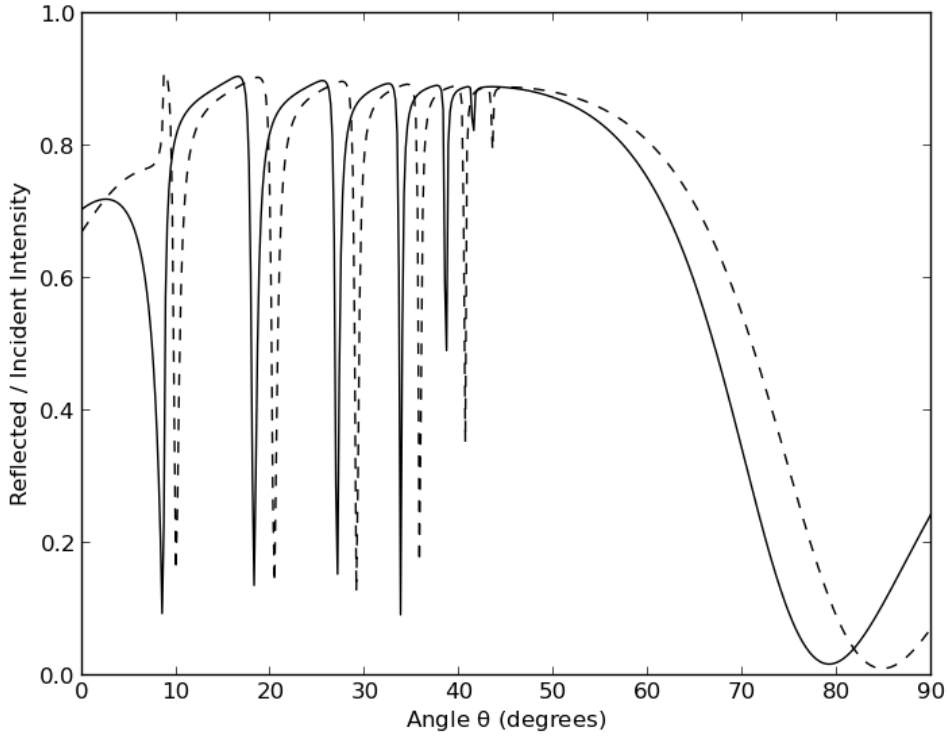

Figure 5.17: Simulated OWS angle scans using $n_0 = 2.584$ rutile prism and the values in table 5.1 before dye application (solid line) and after dye application (dashed line).

If waveguide modes measure the total amount of dye in the film then surface plasmon monitoring can measure the amount of dye at the hidden interface (the TiO_2/gold interface). Figure 5.17 shows a simulated OWS spectra before and after the application of dye for a TM illumination but using a rutile prism with a refractive index of $n = 2.584$ rather than glass. At large incident angles (95° and 79°) there is a large resonance due to the excitation of a surface plasmon. Using a glass prism the plasmon resonance is only visible if the film is in air rather than solution, however, using a rutile prism extra information is available because the plasmon is fundamentally different to the other waveguide modes. Unlike a waveguide mode which is an optical resonance across the whole TiO_2 layer, the plasmon mode is a resonance at the TiO_2 surface and as such it is only sensitive to conditions at the surface.

Figure 5.18 compares the magnetic field in the y-direction for a plasmon and a waveguide mode. The solid line in figure 5.18 shows the magnetic field in the

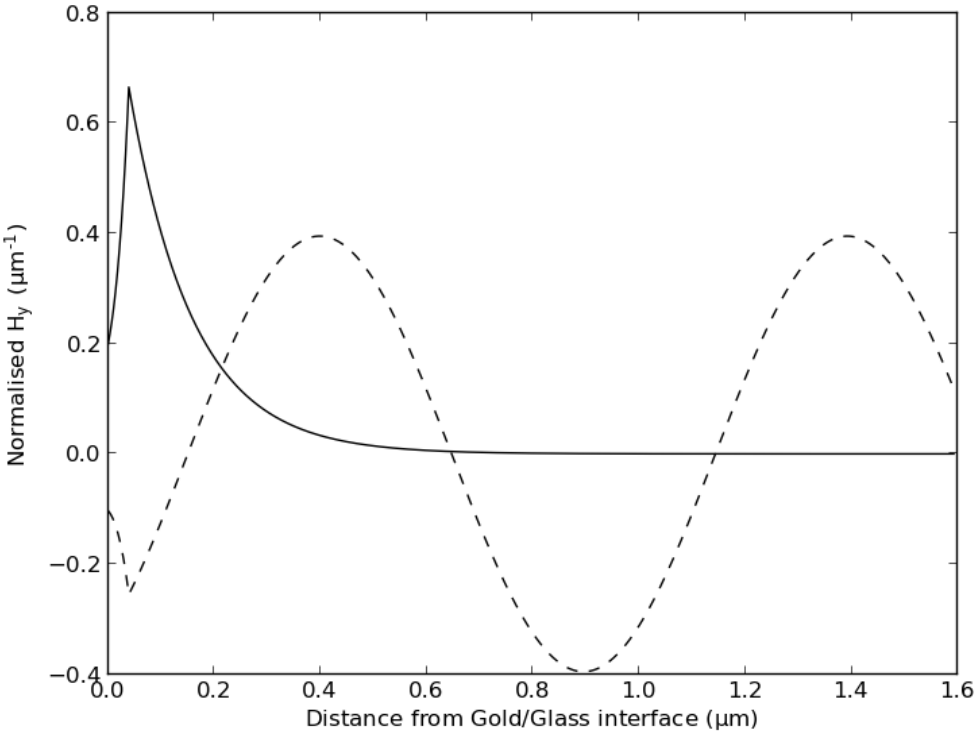

Figure 5.18: The surface plasmon (solid line) and TM3 mode (dashed line) simulated using $n_0 = 2.584$ rutile prism and the values in table 5.1 before dye application

y-direction for an incident angle of 79° (position of the plasmon resonance in figure 5.18) and the dashed line shows the guided mode excited at 28°. The waveguide mode is a standing wave between the gold/TiO_2 interface and the liquid/TiO_2 interface. The plasmon however propagates at the gold/TiO_2 interface and hence it is far more sensitive to the refractive index near the gold layer (left hand side of figure 5.18) than near the liquid layer (right hand side of figure 5.18). Both plasmon resonance and waveguide resonances are valid solutions to equation 5.12.

By monitoring both the plasmon resonance and the waveguide modes one can measure the change in refractive index at the gold/TiO_2 interface and the total amount of dye within the whole film providing much more information, particularly spatial information, than the conventional OWS experiment. This is demonstrated in figure 5.19 which is a repeat of the calculation performed in figure 5.16. The position of the plasmon only shifts when the diffusion front reaches within approximately 150nm of the gold layer. Clearly the incident angle that excites the plasmon is not a good indicator of the total amount of dye in the film,

but it is a very clear indicator of the presence of dye 150nm from the gold layer.

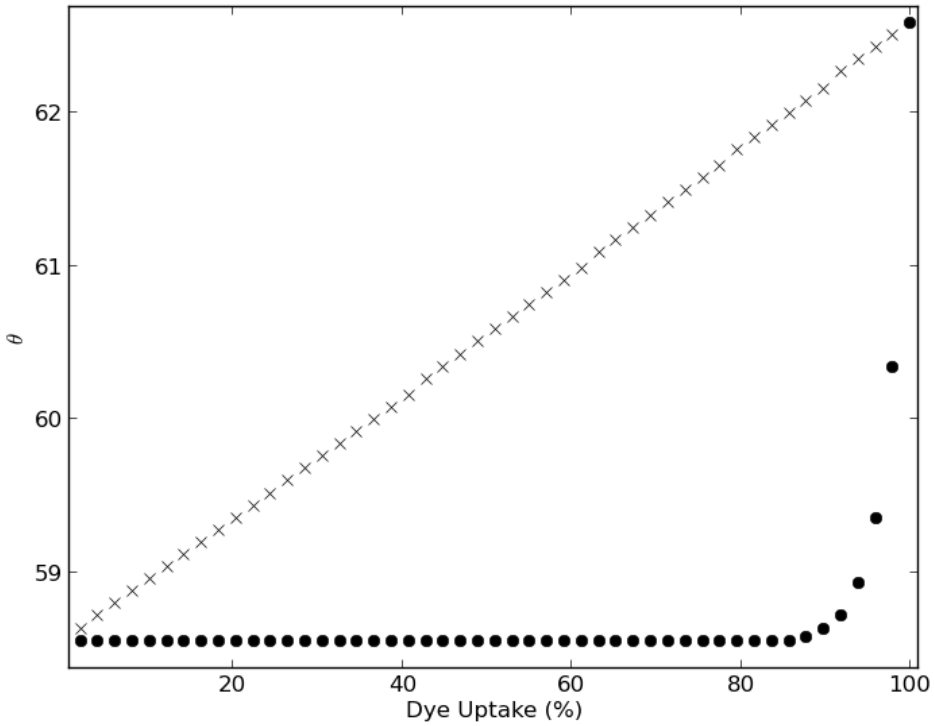

Figure 5.19: Simulated shift in the plasmon mode using a rutile prism ($n = 2.584$) and $\Delta n = 0.0245$ for a perfectly sharp diffusion front (circles), and for a perfectly flat concentration (no positional dependence on concentration within the film), (crosses).

Figure 5.20 is very similar to figure 5.14 however, here, because of the rutile prism the plasmon is plotted rather than the TM4 mode. Again, the case for equilibrium constant $K = 0$ is compared with the case where $K = 1 \times 10^{10}$. The position of the plasmon for the two different cases is now radically different and it is obvious when the dye has reached within 150nm of the gold layer. It should be stressed that the waveguide modes and the plasmon could be tracked simultaneously. Monitoring the plasmon is not at the expense of monitoring the waveguide modes.

5.8 Discussion

There are three principle observations from the results section that are particularly noteworthy and will be discussed further in the next three subsections.

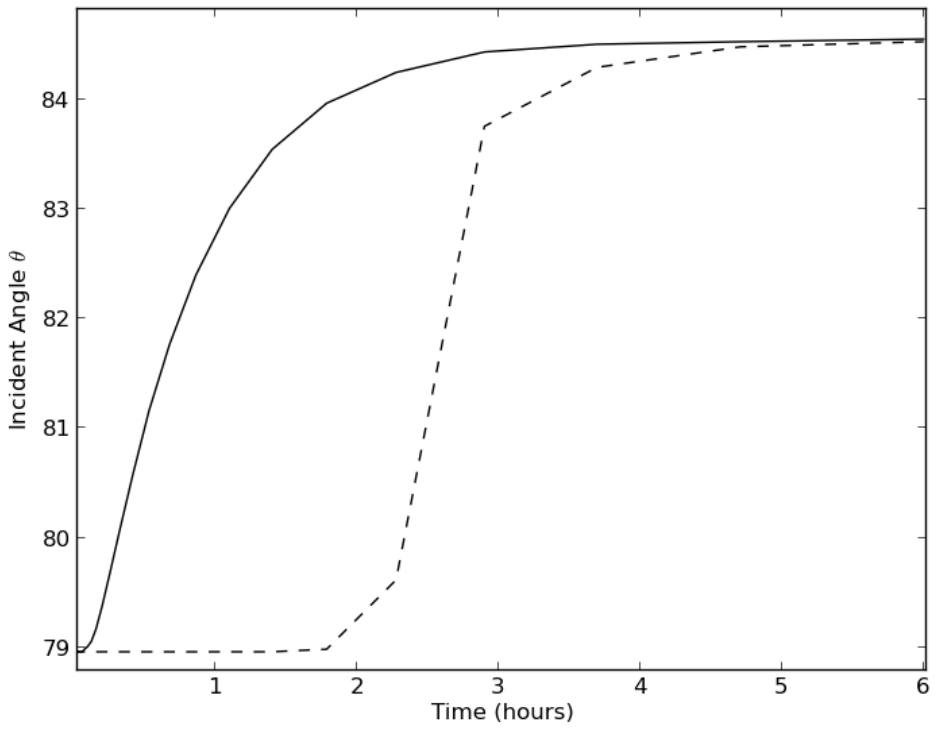

Figure 5.20: Simulated shifts in the plasmon resonance using a rutile prism ($n = 2.584$) for the case of a diffusion front ($K = 5 \times 10^{10}$, dashed line) and pure diffusive behavior ($K = 0$) (solid line) produced using the optical model, the diffusion-adsorption model and the refractive index model. $D = 358$ m^2/s, dye bath concentration = 0.12 m mol dm^{-3}, $\Gamma_m = 0.3$ m mol dm^{-3}.

5.8.1 Discrepancy between experimental and simulated data

The fact that the simple diffusion-adsorption model could not fit the experimental data has several implications. Firstly, one should note that the current body of experimental OWS data is very small and only data from a single TiO_2 film was available at the time of writing. Any conclusions are very much dependant on these films being typical of those being used by the wider academic and industrial community. This does not mean that there is any particular reason to think that these films are atypical, they have been produced using the standard doctor blading technique. This model will need to be applied to the growing body of data as it becomes available in order to test if any conclusions presented here are widely applicable.

In the measured film there appears to be a very rapid uptake of dye followed by a slow uptake which continues indefinitely and it was impossible to fit the data to both the rapid and the slow regimes using only one set of parameters. Either the form of diffusion and adsorption is different from that postulated in the model or the geometry of the film is causing the dye to behave unexpectedly. The first explanation is not supported by UV-Vis spectroscopy experiments at low concentrations which give results consistent with Langmuir type adsorption, as stated in section 5.5. UV-Vis spectroscopy experiments at higher concentrations are unreliable since the dye tends to aggregate at concentrations typical for dying films (0.12 m mol dm^{-3}) and this might be a clue as to why a simple diffusion-adsorption model is not sufficient. Dye molecules aggregating inside the film may be preventing more dye molecules entering the film behind them producing rapid and then slow transport as pathways become increasing constricted or cut off. An alternative hypothesis is that, even without the presence of dye, there are constricted pathways in the film and the dye is moving more slowly through these pathways compared to larger pathways.

Ascertaining which of these explanations is correct is important since they have implications for how DSSC are constructed and even suggest that there may be scope for increasing cell efficiency. If dye is aggregating inside the film then preventing this aggregation could seriously decrease dyeing times. A dyeing time of only 2-3 hours would be expected if the initial rate of dye uptake in figure 5.6 is extrapolated to longer time scales. If dye is moving slowing through constricted pathways at long time scales then this suggests that some fraction of the film may remain free of dye even once the dying process is complete and no light harvesting will take place in these regions leading to a drop in efficiency.

5.8.2 Spatial resolution of OWS without plasmon monitoring

One objective of this project was to calculate if OWS has the capacity to measure the concentration of dye as a function of position within the film. The OWS model has been used to show that the shift in any of the waveguide modes is essentially proportional to the total amount of dye across the whole film. In this regard the OWS experiment contains little more information that UV-Vis spectroscopy,

never the less OWS still does have several advantages over existing methods. OWS is a direct measurement of the TiO_2 film unlike UV-Vis spectroscopy that infers information about the film by measuring the surrounding solution and unlike UV-Vis spectroscopy OWS appears be reliable using high concentration dye baths. Other techniques such as INPS and the photographic method which use high concentrations of dye only measure the uptake of dye at a particular surface. OWS is unique in that it is compatible with high concentration dye baths and sensitive to the whole volume of the film.

The model presented here has allowed the interpretation of OWS to be greatly simplified. Now that it has been established that the shift in each of the modes is proportional to the total amount of dye in the film, one can compare the rate of uptake between different dyes or between different films made using different techniques without the need for further simulations.

5.8.3 OWS with plasmon monitoring

The model has shown that by using a rutile prism the surface plasmon at the gold layer can be used to measure the concentration of dye at the gold/glass interface, and that the shift in the plasmon is proportional to the concentration of dye at the gold layer. Where in the past different techniques in different laboratories have been used to measure dye concentration in the bulk of the film, and at the hidden interface, the OWS experiment offers the exciting prospect of measuring the total amount of dye within a film and the concentration of dye at the hidden interface simultaneously in the same film for the first time. OWS with plasmon monitoring gives this extra information without loosing any of the advantages that OWS has over other techniques.

From results with surface plasmon monitoring it should be possible to infer some information about how dye is diffusing and becoming bound to the surface of the film. For instance if a shift in the plasmon resonance is only observed once the wave guide resonances have shifted, then this is consistent with a diffusion front. On the other hand if the plasmon resonance and waveguide resonances move in unison then this is consistent with the concentration of dye increasing approximately evenly through the whole film and transport being much more rapid than dye binding. Such results could potentially help to explain why uptake

appears to be rapid at short time scales and slow at long time scales. For example, if the transition between rapid and slow uptake occurs at the same time as the plasmon shift then this might suggest that dye has diffused completely through large channels in the film and is continuing to diffuse slowly into constricted pathways or pathways that have been blocked by surface bound dye.

An OWS set up using a rutile prism is currently being constructed and the OWS model will be useful for interpreting the results.

5.9 Conclusions

By modelling the OWS experiment it has been possible to show that OWS is an integral method that measures the total amount of dye in a porous TiO_2 film. Strictly speaking there is some spatial information contained in the signal but it will be difficult to extract this information. Given that the model has shown the addition of plasmon monitoring would provide spatial information that is easy to extract and interpret, it appears that OWS with plasmon monitoring would be the best way of continuing to study dye uptake in TiO_2 films.

From the limited OWS available it appears that dye diffuses rapidly into the TiO_2 film before slowing for an unknown reason. Explaining why uptake appears to slow down is important since slow uptake presents a barrier to creating light sensitive films on a time scale compatible with mass production.

Chapter 6

Influence of Ionizing Dopants on Charge Transport in Organic Semiconductors

The transport properties of organic semiconductors can be improved by generating extra carriers through the use of ionizing chemical dopants. However, In addition to extra carriers, chemical doping produces anion-cation pairs in the organic matrix. This chapter presents a collaboration where computer simulation and experimental studies by A. Abate are used to study the influence of these pairs on the charge mobility. The key result is that, at doping levels below 1%, the anion-cation pairs result in an order of magnitude decrease in mobility compared to zero doping. At higher doping levels the decrease in mobility is small. The study helps to explain the relationship between doping level and conductivity in organic semiconductors and suggests that doping levels below 1% are less effective.

6.1 Introduction

Conventionally, we think of polymers and plastics as insulating materials, especially so since plastics are frequently used to insulate metal wires. However, in 1977 the polymer polyacetylene was synthesised as a film and then oxidised by

a halogen vapour, (Cl_2, Br_2 or I_2) [99]. After exposure to the vapour the polymer increased in conductivity by around nine orders of magnitude to 10^5 S/m, for comparison, copper has a conductivity of around 10^7 S/m and glass no more than 10^{-10} S/m. By analogy with solid state semiconductor physics, polyacetylene was the first example of doping in an organic semiconductor by introducing carriers into the polymer chain.

Organic semiconductors are either polymers such as polyacetylene with alternating double bonds along the carbon backbone (conjugated polymers) or small molecules (a simple example is pentacene) containing benzene rings [100]. Organic semiconductors have been used to construct organic light emitting diodes, organic transistors and organic solar cells [101, 102, 14]. In particular ssDSCs have been constructed using a doped organic semiconductor where doping has been shown to increase performance [16].

Dopants can either reduce or oxidise the polymer. For example, I_2 reduces polyacetylene resulting in an additional charge carrier (oxidative doping) [100].

$$[\mathrm{CH}]_n + \frac{3}{2}\mathrm{I}_2 \rightarrow [\mathrm{CH}]_n^+ + \mathrm{I}_3^- \tag{6.1}$$

Alkali metals reduce polyacetylene in a process called reductive doping and a negative carrier is created.

$$[\mathrm{CH}]_n + \mathrm{Na} \rightarrow [\mathrm{CH}]_n^- + \mathrm{Na}^+ \tag{6.2}$$

The additional polymer radical is a mobile charge coupled to a distortion in the polymer known as a polaron [100].

Gregg *et al.* demonstrated that the majority of doping induced charges are bound to their counter ions at room temperature forming anion-cation pairs [103]. Although it is accepted that the extra carriers will increase conductivity [104], the electrostatic interaction between carriers and the remaining anion-cation pairs has received little attention. It is hard to study only the influence of anion-cation pairs under normal working conditions when both free carriers and anion-cation pairs are present in the system. If a system can be constructed and understood where there are no free carriers, and only anion-cation pairs, the influence on mobility of these anion-cation pairs can be measured and predicted.

The focus of this chapter is on small molecules, in particular the commonly used hole transporter 2,2,7,7-tetrakis(N,N-di-p-methoxyphenyl-amine)9,9-Spirobifluorene (Spiro-OMeTAD) because it has been used with dopants in ssDSCs [16]. In particular, the influence of anion-cation pairs on mobility is isolated. This is possible because measurements of the conductivity of Spiro-OMeTAD have been performed with the inert additives $Et_4N^+ - TFSI^-$ and $Na^+ - TFSI^-$. These inert salts only produces anion-cation pairs and no extra carriers. Monte Carlo simulations of conductivity measurements on Spiro-OMeTAD doped by inert salts are presented here and compared to a parallel experimental investigation by A. Abate.

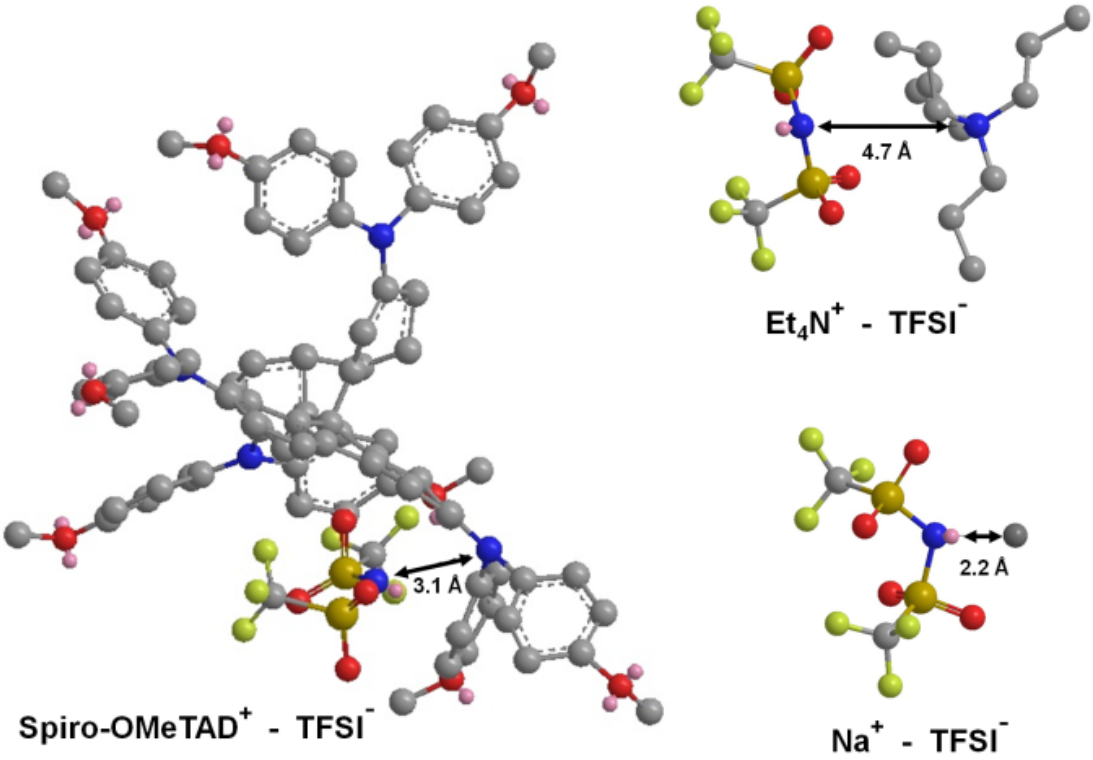

Figure 6.1: The ionic species generated by lithium doping of Spiro-OMeTAD and the inert salts Et4N-TFSI and Na-TFSI. C gray,N blue, F yellow, O red, S orange, Na black. Generated by A. Abate.

By measuring and simulating the addition of Na^+ $TFSI^-$ and Et_4N^+ $TFSI^-$ to Spiro-OMeTAD the loss in conductivity due to anion-cation pairs embedded in the Spiro-OMeTAD matrix can be quantified. At doping concentrations below 1% a sharp one order of magnitude drop in conductivity was measured. Above 1% the decrease in conductivity is less than an $\approx$ a factor of 5 drop and independent of doping level. These measurements are consistent with the Monte Carlo simulations presented in this chapter and suggest that the electrostatic interaction

between carriers and anion-cation pairs is responsible for the observed trends. The results are compared with measurements using Li^+ $TFSI^-$ which is an ionizing dopant of Spiro-OMeTAD despite earlier reports to the contrary [105, 106]. Abate and co-workers propose that in the presence of oxygen doping takes place through the following mechanism[105]

$$\text{Spiro}-\text{OMeTAD} + \text{O}_2 \longleftrightarrow \text{Spiro}-\text{OMeTAD}^{\cdot+}\text{O}_2^{\cdot-} \tag{6.3}$$

$$\text{Spiro}-\text{OMeTAD}^{\cdot+}\text{O}_2^{\cdot-} \longrightarrow \text{Spiro}-\text{OMeTAD}^{\cdot+}\text{TFSI}^- + \text{Li}_x\text{O}_y \tag{6.4}$$

The observed increase in conductivity is consistent with the conclusions from this study. Li^+ $TFSI^-$ has also been seen to increase the efficiency if ssDSCs using Spiro-OMeTAD and MEH-PPV [107, 108]. The results of this study can easily be applied to other similar systems such as poly-3-hexylthiophene (P3HT) and pentacene as both are often doped by tetrafluorotetracyanoquinodimethane (F4TCNQ) in a similar process. The remainder of this chapter will focus on the Monte Carlo simulations used in this study. Carriers in the organic matrix are described by the hopping model.

6.2 The Hopping Model

The hopping model describes the motion of carriers in an organic conducting matrix by asserting that the carrier moves between discrete hopping sites. The carrier is a polaron which sits in a potential well due to the distortion it creates and must overcome a potential barrier in order to hop between polymer segments [109]. Figure 6.2 shows a particle with energy U_i in a metastable state. There is a certain probability that, if given some thermal energy, the particle could overcome energy barrier $\Delta U = U_j - U_i$ and move into the lower energy state at distance r. It is important to note that the energy of the vacant potential well is not important, it is the height of the barrier that controls the chance of a transition [110]. In the classical limit the probability of a transition is given by a Boltzmann distribution [110]

$$P \propto \exp \frac{-\Delta U}{k_B T} \tag{6.5}$$

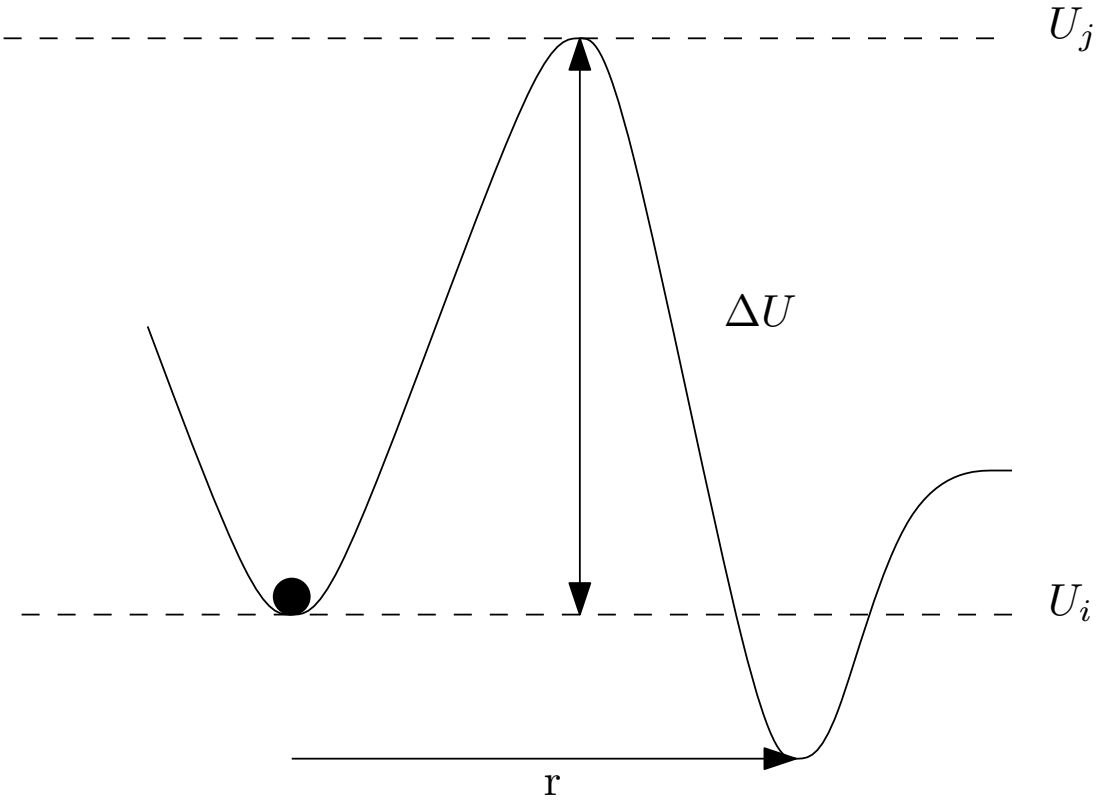

Figure 6.2: Picture of the energetic landscape used in the hopping model. Particles have to overcome energy barrier ΔU to move between hopping sites separated by distance r.

where P is the chance that a heat reservoir at temperature T provides sufficient energy to overcome the barrier. Using a constant of proportionality ν this can be written as a rate

$$k = \nu \exp \frac{-\Delta U}{k_B T} \tag{6.6}$$

where ν has units of frequency and can be pictured as the number of attempts made per unit time to overcome the barrier. The hopping model for polarons is not just dependent on the barrier height but also the distance between hopping sites. Also, one needs to consider what the rate might be if there is no barrier. This leads to the variable-range hopping model of Miller and Abrahams

$$k = \begin{cases} \nu \exp\left(-\Delta U / k_B T\right) \exp\left(-2\alpha r\right) & \text{if } \Delta U > 0 \\ \nu \exp\left(-2\alpha r\right) & \text{if } \Delta U < 0 \end{cases} \tag{6.7}$$

Equation 6.7 was first derived for hopping between isolated band gap states just below the Fermi energy [111, 112, 109]. α is the localization constant which determines how far the polaron can move between two sites in one hop.

In order to investigate the influence of anion-cation pairs on carrier mobility equation the hopping model is solved using the Kinetic Monte Carlo (KMC) model.

6.3 The Kinetic Monte Carlo (KMC) Method

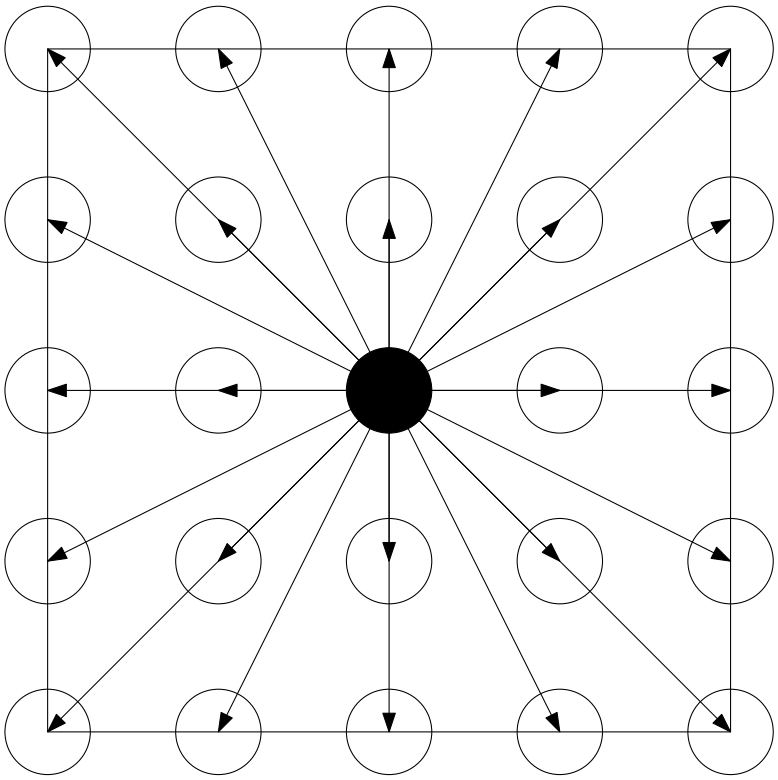

Figure 6.3: A particle in a grid of 25 hopping sites each with an associated rate k. The KMC method moves the particle between sites and calculates the time taken for each transition.

Imagine the situation in figure 6.3, this is much more complex than the situation in figure 6.2. There are 24 possible transitions each which may have a different energy barrier, hopping distance and hence rate. There is no transition which is certain to take place first nor is there a definitive length of time before the first transition is complete. For a particle where many such transitions are possible the Kinetic Monte Carlo (KMC) method can take a set of probabilities and move the particle with the correct dynamics in a statistically correct fashion. In essence, the KMC method is described by algorithm 1 [110].

STEP 1: If there are N hopping sites, number every hopping site with a unique integer i;
Set time $t = 0$;
for *each iteration* **do**
  for $i = 0$ *to* N **do**
    calculate transition rate k_i;
    calculate cumulative sum $K_i = \sum_{j=0}^{j=i} k_j$;
  end
  Get a random number r between 0 and 1;
  for $i = 0$ *to* $N - 1$ **do**
    if $K_i < rK_N < K_{i+1}$ **then**
      move the particle to site $i + 1$;
    end
  end
  STEP 2: Get a new random number r;
  $t = t - \log r / K_N$;
end

Algorithm 1: The KMC method

Algorithm 1 can be split into two parts. In part 1 a transition is chosen with a probability proportional to the rate of that transition using the first random deviate. In part 2 the time t is updated using a second random deviate. In step 1 the rate of transition is set to be proportional to the probability of the transition and a transition is chosen accordingly. The use of a cumulative sum K and a single random number r is an example of the roulette wheel selection method.

Part 2 is subtle so it will be explained here in more detail. It is useful to note that each transition is totally independent of any of the other transitions. Each transition is also independent of the history of the particle. This is an example of a Poisson process, a subject that has been extensively studied. The probability density of a Poisson process $\rho(t)$ with rate k_i is

$$\rho(t) = k_i \exp(-k_i t). \tag{6.8}$$

The second property of a Poisson process is that, for a large set of Poisson processes N, the probability density for any one of the processes to occur is given by [110]

$$\Gamma(t) = K_N \exp(-K_N t) \tag{6.9}$$

where

$$K_N = \sum_{i=0}^{N} k_i. \tag{6.10}$$

To calculate the transition time correctly, a time needs to be selected randomly but also with a probability proportional to $\Gamma(t)$. Formally, if one equates a uniform random deviate r between 0 and 1 to the integral of the probability density

$$r = \int \Gamma(t)dt = \exp\left(-K_N t\right) \tag{6.11}$$

and then rearranges the result to give

$$t = -\frac{\ln r}{K_N}. \tag{6.12}$$

then t is a time sampled correctly from $\Gamma(t)$ [110].

6.3.1 Pseudo-random numbers

For all studies in this chapter the assignment of random numbers was performed using the Mersenne Twister algorithm [113]. Pseudo-random number generators are by their nature deterministic and from a given starting point (or seed state) they will always produce exactly the same set of numbers. The period of the generator is the number of calls to the generator before the seed state is returned and the generator starts cycling over the same set of numbers. The Mersenne Twister has an extremely high period of $2^{19937} - 1$. Such a high period ensures no cycling before the end of the simulation is reached otherwise unwanted statistical bias could be introduced into the simulations.

6.4 The dipole model

The KMC model can be used to simulate polaron hopping but it relies on sets of site energies to calculate hopping rates [109]. These site energies are calculated using the dipole model which is described in this section. KMC hopping models of doped organic systems have been presented before yet they only considered the interaction between charges of opposite sign [114, 115]. The dipole model

includes the interactions between carriers, positive charges and negative charges. This is essential in order to capture the short range forces resulting from dipole interactions.

The energy U_i of each site i is the sum of contributions from random disorder $U_{i,Gauss}$, the electrostatic interaction energy from anion-cation pairs $U_{i,dipole}$ and the energy from any macroscopic electric field due to an applied bias $U_{i,bias}$.

$$U_i = U_{i,Gauss} + U_{i,dipole} + U_{i,bias}. \tag{6.13}$$

The intrinsic carrier density is always less than $10^7 \mathrm{cm}^{-3}$ so only a single particle (hole) is considered in the simulation [116]. Each term will now be examined in more detail.

The Gaussian Disorder Model (GDM) assigns the energy of each site U_i using a Gaussian distribution with standard deviation σ so that the probability of finding site i with energy $U_{i,Gauss}$ is

$$d\rho\left(U_{i,Gauss}\right) = f(U_{i,Gauss}) dU_{i,Gauss}. \tag{6.14}$$

$$f\left(U_{i,Gauss}\right) = \left(2\pi\sigma\right)^{-\frac{1}{2}} \exp\left[\frac{U_{i,Gauss}^2}{2\sigma^2}\right] dU_{i,Gauss}. \tag{6.15}$$

In order to calculate the term $U_{i,dipole}$, a cube of dimensions $L \times L \times L$ with periodic boundaries is simulated containing a simple cubic lattice of hopping sites with lattice constant $n = 2\mathrm{nm}$ (this is approximately the size of the Spiro-OMeTAD molecule in figure 6.1). Figure 6.4 shows $f(x)$ for $(L/n)^3 = 1000$ sites, the smallest number of sites used in this study, and demonstrates that it is indicative of a Gaussian distribution. A dipole is placed in the center of the lattice where each coordinate has position $\pm\left(d, d, d\right)$. $(0, 0, 0)$ is the center of the cube. At every hopping site i, $U_{i,dipole}$ is calculated using Coulombs law, this includes the electrostatic potential from the dipole at the center of the cube and an infinite lattice of dipoles centred at $(m_1 L, m_2 L, m_3 L)$. (m_1, m_2, m_3) is a translation vector of any three integers between $\pm\infty$. $U_{i,dipole}$ can then be calculated by summing coulombs law or by using a Ewald summation until the sum has converged. The concentration of dipoles is simply $1/L^3$. Figure 6.5 illustrates a 2D slice of the 3D square lattice of hopping sites with $U_{i,dipole}/\sigma$ plotted using contour lines. U_{guass} is not shown because it obscures the data. Future figures show only one unit

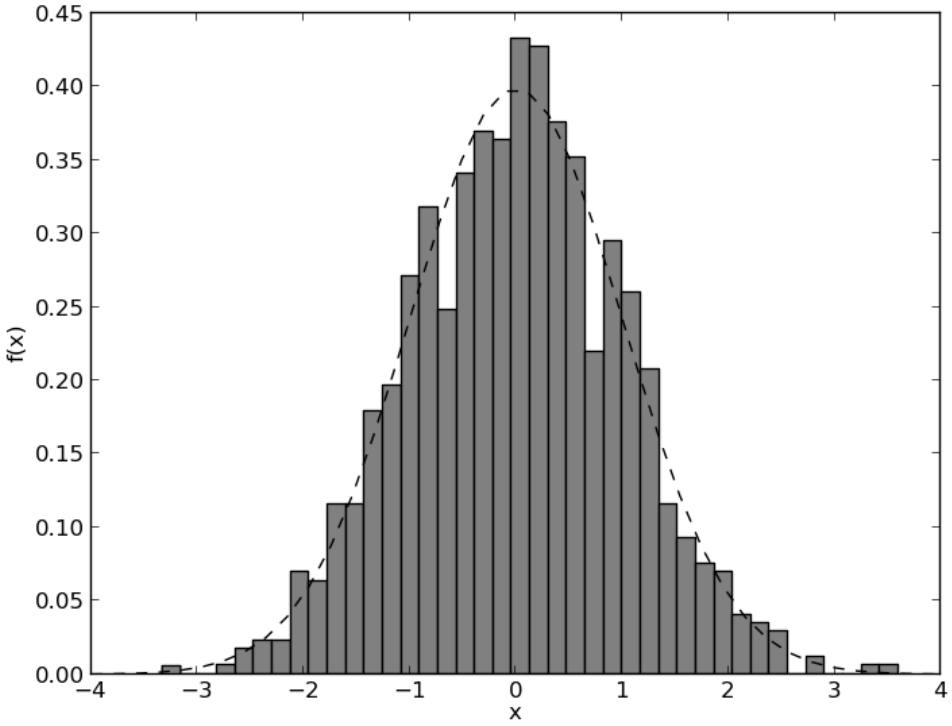

Figure 6.4: Histogram: 1000 random deviates sampled from a Gaussian distribution using the Mersenne Twister algorithm with a standard deviation of $\sigma = 1$. Dashed line: A Gaussian distribution with standard deviation $\sigma = 1$.

cell of the periodic potential since this contains the same information in a more compact form. The doping level is the number of dipoles divided by the number of hopping sites in the unit cell.

$U_{i,bias}$ is set so that the carrier is subjected to a constant force in the x-direction. For a hop from site i to site j, separated by length x, an energy $U_{i,bias}$ is added to the energy of site j to simulate an electric field E in the x direction where

$$U_{i,bias} = -qxE. \tag{6.16}$$

For every transition between hopping sites, the displacement in the x direction is added to a running tally. The elapsed time is added to a separate tally. As such it is straight forward to calculate the drift velocity for an applied electric field E.

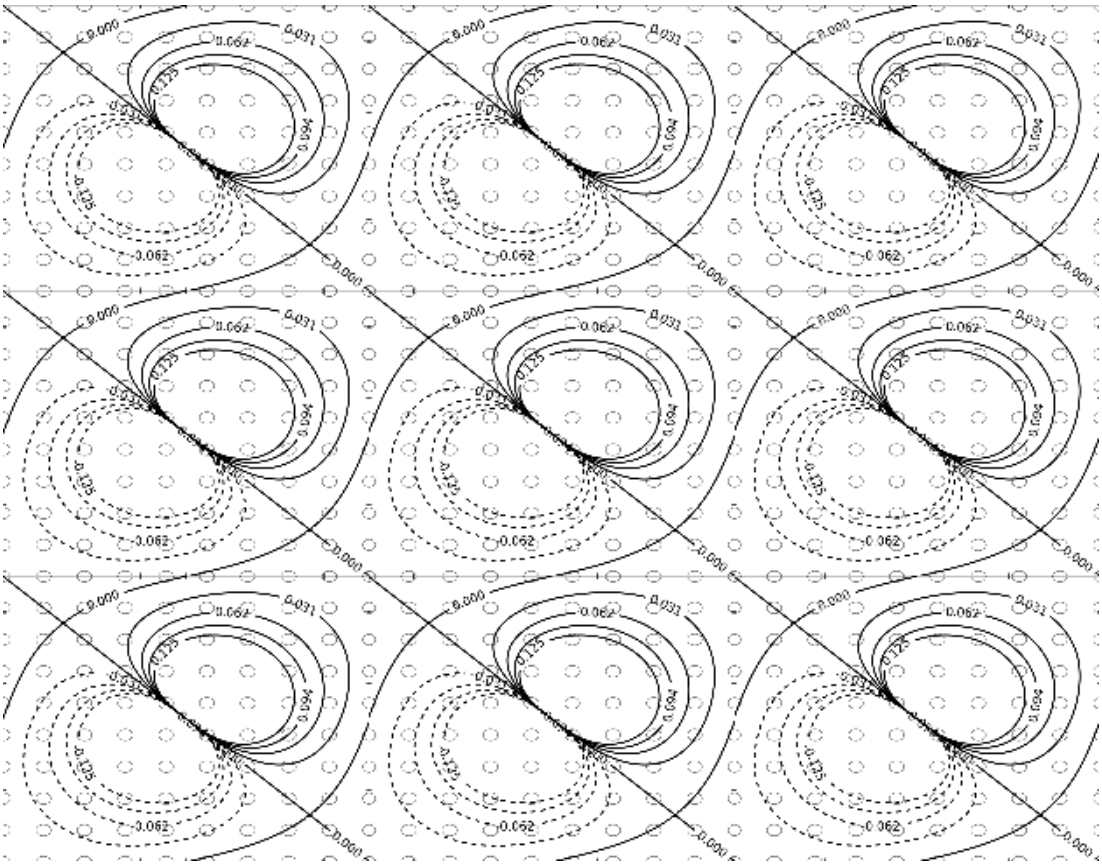

Figure 6.5: A 2D slice of the periodic electrostatic potential landscape U_{dipole}/σ experienced by the carrier with hopping sites (circles) overlaid. In this case a periodic array of 9 dipoles is shown where the potential is unchanged over 9 hopping sites. The calculation has been performed for an infinite 3D square lattice of dipoles.

6.4.1 Accompanying experimental study

An accompanying experimental study was carried out by A. Abate which will feature in the results and discussion. Spiro-OMeTAD was spin coated onto glass substrates with various concentrations of salts to compare the conductivity of the sample at different doping levels.

6.5 Results

The expected increase in conductivity is three orders of magnitude for a 1% doping level with Li^+ ions. This is represented by the dashed line in figure 6.6. It is evident from figure 6.6 that the observed increase in conductivity is less

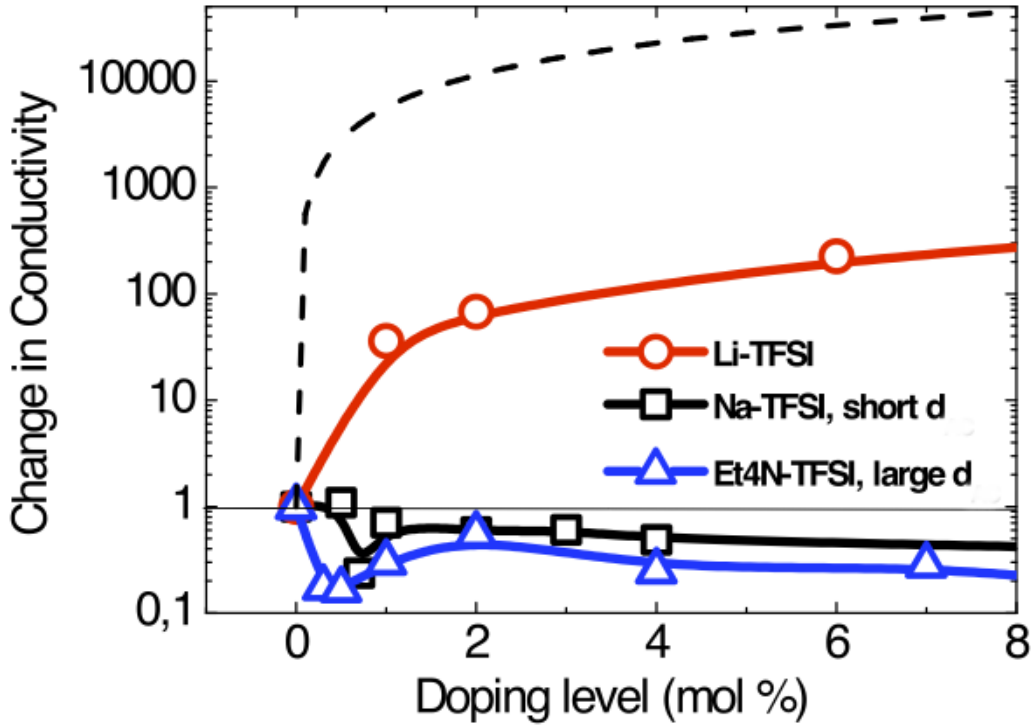

Figure 6.6: Conductivity of Spiro-OMeTAD doped with Li-TFSI and the inert salts Na-TFSI (small dipole moment) and Et4N-TFSI (large dipole moment), normalized to the conductivity of undoped Spiro-OMeTAD. The dashed line shows the expected increase in conductivity if every Li^+ ion provides one extra carrier. Provided by A. Abate.

than two orders of magnitude at the 1% doping level. This 'missing' increase in conductivity is approximately accounted for by the one order of magnitude reduction in conductivity at the 1% Na^+ and Et_4N^+ doping level in figure 6.6.

Parameter	Symbol	Value
Disorder	σ	0.065 eV
Dielectric Constant		3
Localization Constant	α	2nm
Electric Field	E	0.02V/nm

Table 6.1: Parameters used to generate figure 6.7 taken from references [25, 117].

These trends are qualitatively reproduced by the KMC simulations in figure 6.7. In each case the modelled inert-salt and Spiro-OMeTAD mixture has a minimum below the 1% doping level. As the dipole moment increases the decrease in conductivity becomes less dramatic, and the minimum is predicted to be at increasingly low doping levels. At doping concentrations close to zero there is not a sufficient concentration of anion-cation pairs for carriers to become trapped on

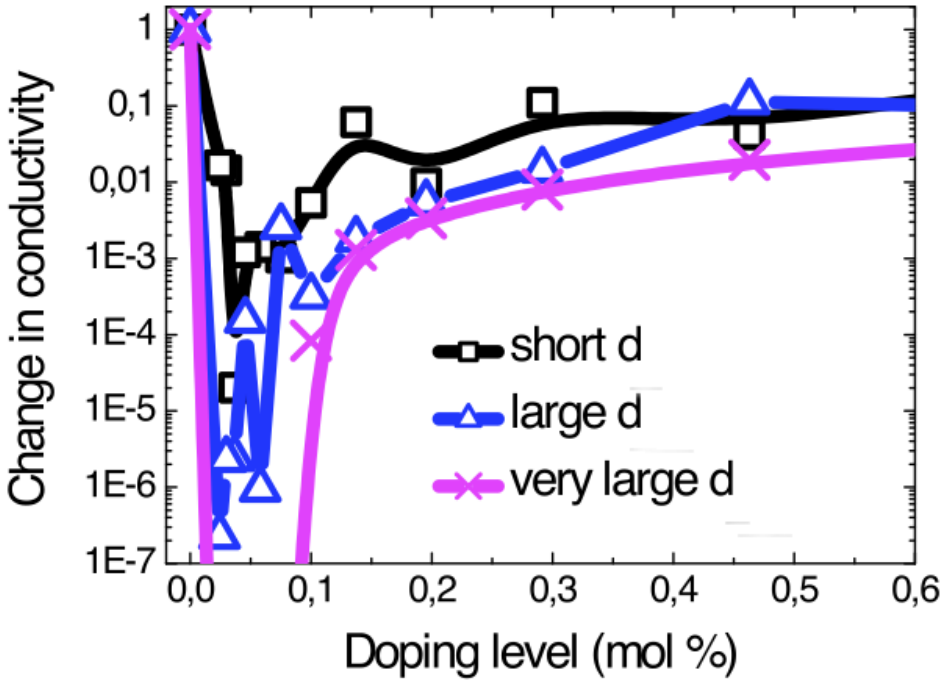

Figure 6.7: Predicted conductivities generated using the KMC and dipole model where $d = 4, 6, 8$Å. All other parameters are in table 6.1. Plotted by A. Abate.

a sufficiently regular basis, so the conductivity remains unchanged. At concentrations higher than 1% the potential wells produced by the anion-cation pairs start to overlap and the resulting traps become increasingly shallow.

Figure 6.8 shows an example of a well converged result from the KMC simulation. The displacement of the hole is proportional to the simulation time so the hole is well described by a singe drift velocity and hence the plot produces a straight line. All of the data sets are well converged and in every case the displacement time relationship can be fit using linear regression with an R^2 value greater than $1 - 10^{-5}$.

Figures 6.9, 6.10 and 6.11 show a cross section of the potential landscape for progressively lower concentrations of dipoles. It should be stressed that the lattice constant $n = 2$nm is the same in each case, only the periodicity governed by the simulation size $L = 3n, 9n$ and $15n$ is changing. The images have been scaled so that they are all the same size for clarity. The cross section goes through the center of the dipole and in the plane of the dipole moment. Figure 6.12 plots the most negative of all the site energies $U_{i,dipole}$ for dipole moment and for simulation

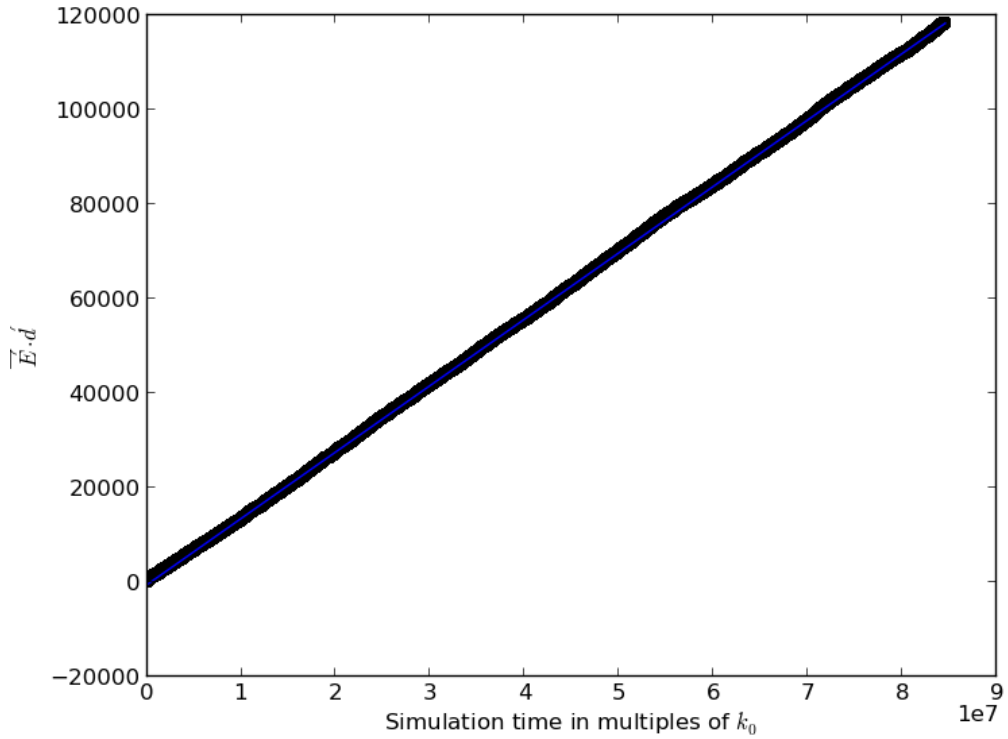

Figure 6.8: Displacement in the direction of the applied field against time with a 0.1% doping level of dipoles with an anion-cation separation of $d = 6$Å. The figure is typical of all data sets.

sizes between $L = 3n$ and $L = 15n$. If each dipole represents a trap for the carrier then this energy is the trap depth.

6.6 Discussion

Figure 6.6 suggests that the deficit between the expected and measured increase in conductivity of Spiro-OMeTAD doped with Li−TFSI may be accounted for by a decrease in mobility from dipole moments embedded in the Spiro-OMeTAD matrix. Gregg has predicted that these dipoles form in Spiro-OMeTAD doped with Li−TFSI because the majority of Li−TFSI salts will not dope Spiro-OMeTAD but rather, the anion and cation will separate slightly forming a dipole. The inert salts, which can only produce dipoles, decrease the mobility by around half an order of magnitude at doping levels less than 1%, and at higher doping levels the mobility is decreased by an approximately constant factor. By comparison

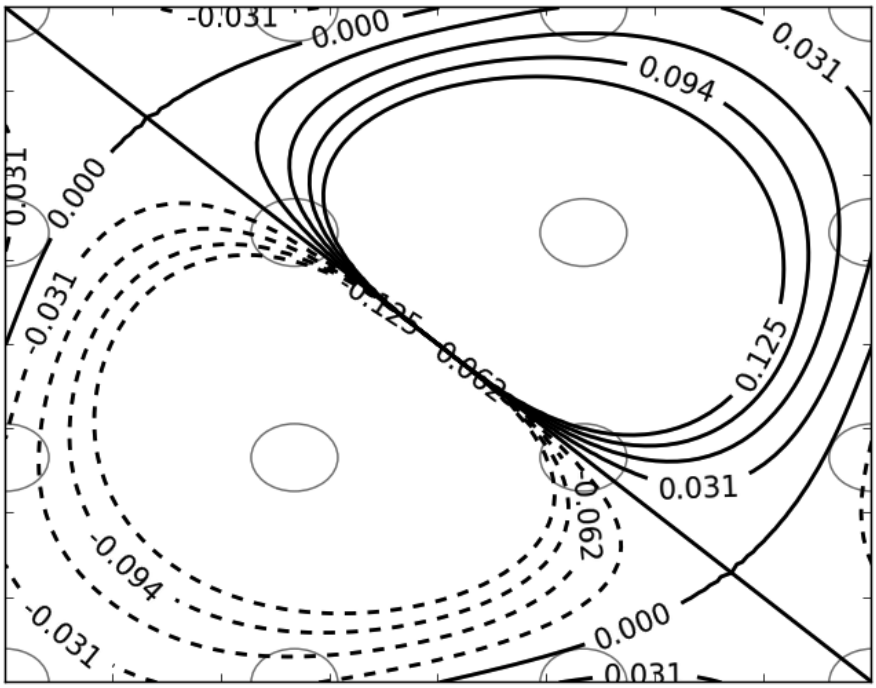

Figure 6.9: Potential landscape generated by taking a 2D slice through the center of the 3D array of site energies U_{dipole} in the plane of the dipole moment where $L = 3n$ and lattice constant $n = 2$nm.

the greatest deficit between the measured and expected conductivity is at doping levels less than 1%. Above 1% the discrepancy is approximately constant so qualitatively the results support the dipole hypothesis. Quantitatively the results do not agree but this is to be expected, since the dipoles from the inert salts in the matrix may have different properties (such as dipole moment) to Li−TFSI.

The monte carlo simulations can be used to test if the dipole hypothesis is energetically plausible. Indeed the monte carlo simulations of Spiro-OMeTAD doped with inert salts in figure 6.7 are qualitatively similar to the measurements in figure 6.6. At low doping concentrations there is a sharp decrease in carrier mobility which then tends towards a smaller but constant reduction in mobility at high doping levels above 1%. Again, quantitatively the results do not match Li doped Spiro-OMeTAD, but for such a basic model which only includes the core physics of the problem the qualitative trends are surprisingly similar.

Figures 6.9, 6.10, 6.11 and 6.12 help to explain the trends in the simulated and experimental data.

The relatively high mobility at high doping levels can be explained by figures 6.9

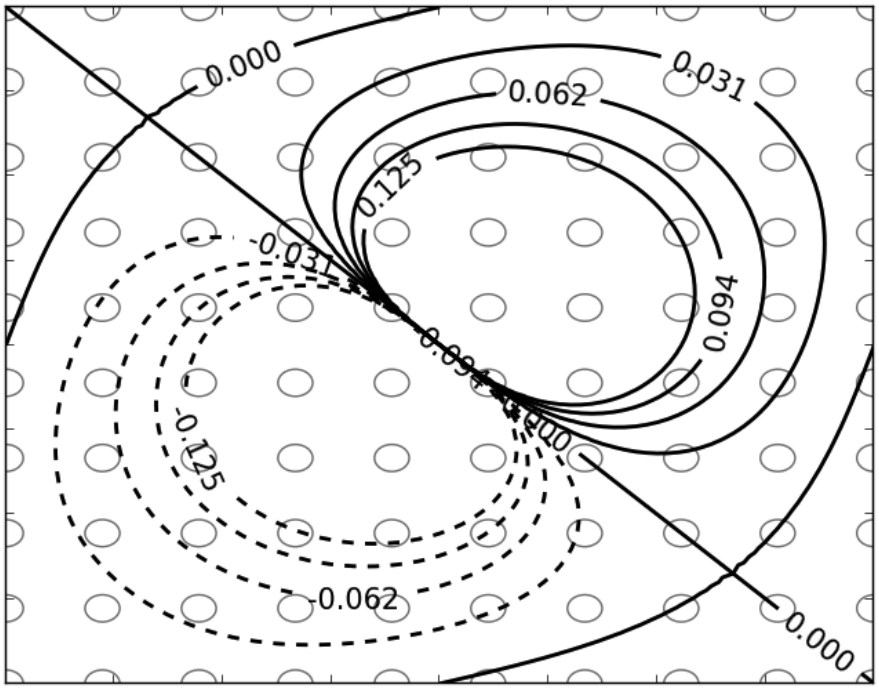

Figure 6.10: Potential landscape generated by taking a 2D slice through the center of the 3D array of site energies U_{dipole} in the plane of the dipole moment where $L = 9n$ and lattice constant $n = 2$nm.

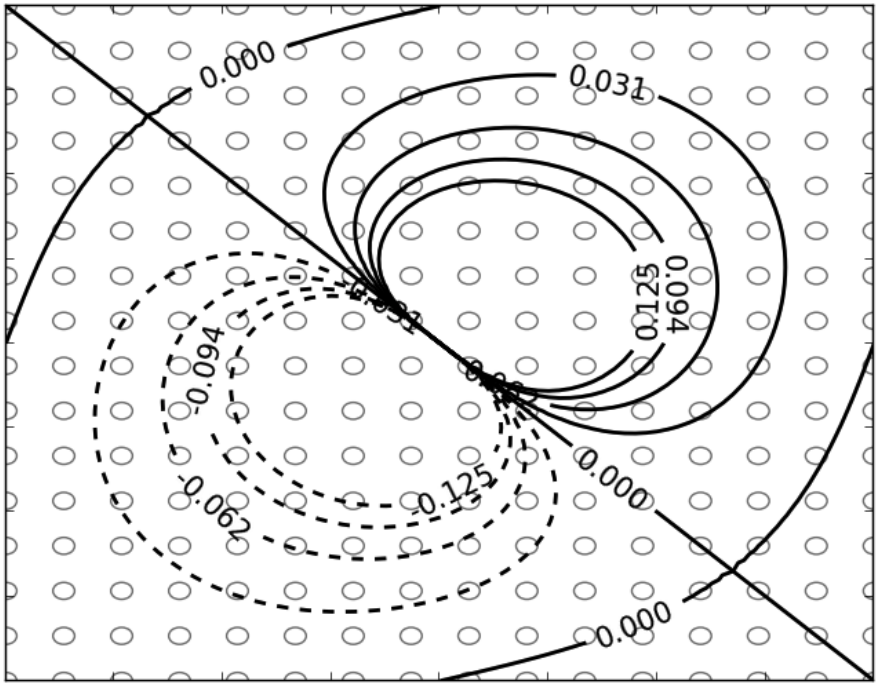

Figure 6.11: Potential landscape generated by taking a 2D slice through the center of the 3D array of site energies U_{dipole} in the plane of the dipole moment where $L = 15n$ and lattice constant $n = 2$nm.

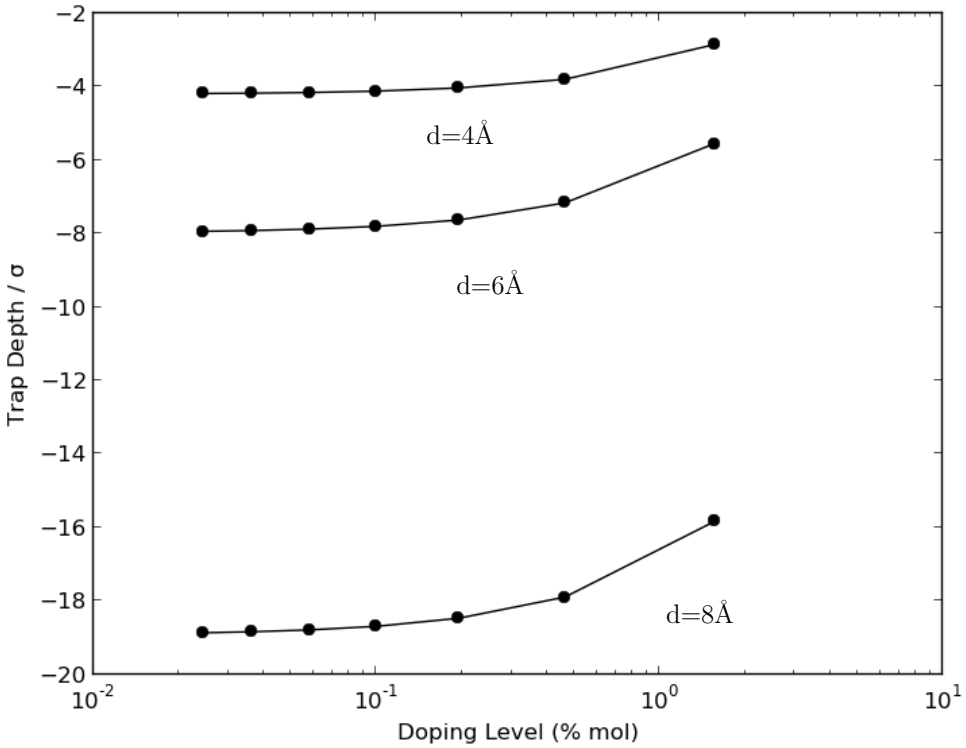

Figure 6.12: The most negative site potential (trap depth) for each doping level and anion-cation separations of $d = 4, 6, 8$Å. All other parameters are in table 6.1

and 6.12. In figure 6.9, where L is small and consequently the dipole concentration is high, only one site immediately adjacent to the dipole sits at a potential lower than 0.125σ, constituting one lone site which is effectively a trap.

Figure 6.12 shows that at high doping concentrations the depth of this trap is relatively small in comparison to low doping levels. In this case the trap depth is -6σ, but at low concentrations it is -8σ. For each dipole length the trap depth always decreases at high doping levels because the potentials from the dipole start to cancel as they are moved close together. This explains why mobility is relatively high at doping levels above 1%.

At very low doping levels the mobility is also relatively high. Figure 6.12 shows that the depths of the traps is greatest at low concentrations however figure 6.11 shows that only a small fraction of the hopping sites are influenced by the dipoles. Although there are strong traps in the system carriers are relatively unlikely to encounter them as the doping concentration decreases. This is not a surprising result if one imagines that the case of zero dopents is the limit where the distance

between dipoles tends to infinity.

At intermediate doping levels there is a combination of deep traps which are close together. The carriers become trapped frequently and for long periods of time resulting in the observed minima in mobility and conductivity.

Figure 6.12 can also be used to interpret the trends with respect to the magnitude of the dipole moment. As the separation between anions and cations is increased the trapping effects increase dramatically. When the separation is doubled from 4Å to 8Å the depth of the traps at low concentrations increases by a factor greater than 4. It is therefore not surprising that when the ions are separated by 8Å the mobility is effectively reduced to a negligible quantity. For larger dipole moments one would expect the minima in conductivity to be shifted towards lower doping concentrations because the extent of the traps will be greater and the change in trap depth and different concentrations will also be greater. At low concentrations the carriers are more likely to encounter the traps but as the doping level increases the potentials from the dipoles start to cancel more rapidly and the mobility will start to increase at lower doping levels. The is observed in the experimental data but is less clear in the monte carlo simulations which appears to contain oscillations which makes the data harder to interpret.

These oscillations in the data are not expected. The results appear to be well converged as in figure 6.8 and the potentials appear to change smoothly as the doping level is varied as shown in figure 6.12. By a process of elimination this seems to suggest that the oscillations are due to finite size effects where the periodicity of the simulation has introduced an unphysical contribution to the mobility. Although it would be preferable to eliminate these effects it is unlikely to change the core interpretation of the data or the resulting conclusions. Especially since by examining the potential landscape the trends in the monte carlo simulations are largely expected and easily explained.

6.7 Conclusions

The existence of anion-cation dipoles resulting from incomplete doping in Spiro-OMeTAD has until now has been postulated, but there has been no study into

how these dipoles might change the carrier mobility and if the impact will be significant. This study has shown for the first time that not only is the existence of these dipoles plausible but they have a significant impact on the carriers, decreasing mobility by half an order of magnitude. The experimental results show that when inert salts are added to the Spiro-OMeTAD they reduce conductivity, and this reduction is qualitatively consistent with the difference between expected and observed increases in conductivity using the active dopant Li−TFSI. This suggests that a significant fraction of Li^+ ions are not reduced, but remain in the Spiro-OMeTAD matrix bound to $TFSI^-$ ions forming dipoles. Moreover the computational study suggests that the trends seen in the experimental results are qualitatively what one would expect if dipoles are present in the organic conductor and these trends can be explained simply from the electrostatic potential generated from a periodic array of dipoles.

If more complete doping could be achieved, where all of the dopants produce an extra carrier and none reside as inert charged pairs then doping in Spiro-OMeTAD and other similar small molecule systems could be much more effective since any increase in carrier density would not be offset by a factor of 5 drop in carrier mobility. In tern this could enable ssDSC and perovskite absorber cells with superior charge collection and higher efficiency. For devices using Li−TFSI doped Spiro-OMeTAD the study suggests that one should use doping levels above 1% to avoid the deep trapping effects observed at lower concentrations.

Chapter 7

Closing Remarks

The attraction of DSC is two fold. Firstly very little energy is required to construct the device. Energy intense purification steps are not required since the precise doping of semiconductors is not required as the device has no built in field. Only relatively modest temperatures of around 400°are required to sinter the DSC photoanode. Secondly DSC are well suited to building integrated applications given that they are flexible and aesthetically pleasing. Yet despite over 20 years of development dye sensitized solar cells have not achieved a commercial dominance over existing PV devices. Ultimately, either the efficiency of DSC must increase or DSC must become cheaper and more practical to manufacture. In addition, new devices such as the solid state DSC have evolved from the original DSC design and it may be these devices that have the biggest impact on the PV market. This thesis has attempted to address each of these three principle areas of efficiency, manufacture and emerging devices.

As the understanding of DSC becomes increasingly complex modelling is becoming an increasingly useful tool for improving DSC. The discovery of non-linear recombination in DSC, and trap distributions characterised by a trapping temperature have brought into question the validity of how measurements of DSC are interpreted, especially cell impedance. Although in some special circumstances DSC can be described by reasonably simple mathematical expressions, such as at open circuit, in general only numerical modelling can correctly predict the influence of these new factors on cell behaviour at the maximum power point and at short circuit.

In this thesis a diffusion model has been presented which rigorously includes the effects of non-linear recombination and trapping for the first time. Conveniently the mathematics of diffusion underpins several other problems relating to DSC and it has been possible to study seemingly distantly related processes using reasonably similar computational methods. The diffusion of dye within porous medium has been modelled to better understand the process of introducing dye to the porous anode of the DSC. Finally the drift and diffusion on polarons in organic semiconductors has been modelled in order to explain the relationship between dopant concentration and conductivity in these systems which are frequently used to construct solid state DSC. Each of these studies will now be summarised and the key conclusions will be emphasised starting with describing DSC impedance.

The frequency dependant DSC model provides a vital link between the microscopic parameters describing DSC and the macroscopic parameters that describe the impedance of DSC. Conventionally the impedance of the DSC anode is described by three equivalent circuit parameters, the transport resistance, the charge transfer resistance and the chemical capacitance. Assuming that the rate of photoelectron recombination is proportional to photoelectron concentration (linear recombination) and if the proportion of trapped photoelectrons is constant with respect to the fermi level then the resistances and capacitances of the cell may be easily related to the density of traps and the diffusion coefficient and recombination rate of the carriers. These assumptions have been shown to be incorrect, never the less the equivalent circuit model does provide a good fit to cell impedances. There has been little analysis regarding the implications of these non-ideality factors because until now a model has not existed that can predict how non-linear recombination will change the device impedance.

One clear implication is that the diffusion length, the square root quotient of the diffusion coefficient and the recombination rate of carriers, becomes ambiguous. For the case of linear recombination all carriers in the device have the same diffusion length yet when recombination is not linear the diffusion length will depend of carrier concentration. The diffusion length is no longer a property of the device unless the carrier concentration is perfectly equal at all points through the DSC anode. Despite this the frequency dependant model has been used to show that if one does fit an equivalent circuit to DSC impedance at the maximum power point the extracted diffusion length is simply related to the average carrier concentration.

DSC exhibit capacitative dispersion at high frequencies where the chemical capacitance becomes frequency dependant, this is consistent with the presence of a constant phase element in the equivalent circuit rather than a capacitor. The model demonstrates that neither non-linear recombination or trapping account for observed capacitative dispersion supporting the proposition that capacitative dispersion results from capacitance at the interface between the anode and the electrolyte.

Because of non-linear recombination and trapping, measuring the diffusion length has become controversial and there has been much disagreement on how to measure it correctly. The patterned electrode experiment was design to measure the diffusion length in the most unambiguous way possible. By removing half of the electron extracting contact of a set of DSC, and by varying the distance between extracting and non-extracting regions one can control the distance electrons must travel in order to be extracted and compare this to the collection efficiency giving a true indication of the diffusion length at open circuit. The results are consistent with those determined using impedance measurements and IPCE measurements. What is unique about the patterned electrode experiment is that it removes any doubt over the validity of these experiments.

Diffusion modelling was used to ensure that a one dimensional model could be used to describe diffusion of carriers to the patterned substrates which is, strictly speaking, a two dimensional problem. The 2D model verifies that a simple analytical expression can be used to extract the diffusion length from the experiment at open circuit. This verification was especially important given that the intention was to make a particularly rigorous measurement of the diffusion length. Experiments at the maximum power point revealed that the results are still indicative of the diffusion length within the cell provided that one recognises that the potential at the substrate will be lower than the average potential within the film.

Extremely efficient PV devices are of no use if they are not practical for mass production. When sensitising the DSC anode best efficiencies are achieved when dye is allowed to diffuse into the film over 12 hours. This is clearly costly on any large scale because the cells would need to be stored and it is not compatible with a production line. If one could monitor the progression of dye through the film during sensitisation then this would give several benefits. One can test to

see if aggregation or pore blocking is preventing rapid sensitization. One can also make comparisons between different dyes and different anchoring groups to find which dyes are most suited to rapid sensitisation.

A diffusion model was constructed to simulate an Opical Waveguide Spectroscopy (OWS) sensor. The sensor monitors the total amount of dye within the film in real time. The model can be used to predict responses of the sensor to clearly defined scenarios such as dye diffusing into the film with no binding to the film, a diffusion front of dye progressing through the film with very strong binding or diffusion with Langmuir adsorption. The model can also be used to test different experimental set-ups which yield more information.

The results show that dye moves anomalously through the film, progressing rapidly into the film for 2-3 hours and then progressing slower than would be expected. There are several possible explanations for this observation which will need to be tested. The geometry of the film could cause dye to move through large pores before moving through constricted pathways on slower time scales. Alternatively the presence of dye could prevent additional dye moving into the film. For instance, dye bound to the surface may be blocking the pores or dye molecules aggregating together may be responsible. If the cause of slow sensitization at long time scales could be identified and resolved films could be sensitised in approximately half the present time scales.

One way of gaining more insight is to monitor the position of dye within the film in addition to the integral amount of dye present in the pores. Initially it was hoped that this information could be extracted from the OWS sensor without modification however, the OWS model demonstrated that this is not possible. On the other hand the model showed that it would be a relatively simple matter to identify when dye has reached the rear of the film by increasing the refractive index of the prism used to couple light into the sensor. Rutile was identified as a material with the correct refractive index commonly available as a prism. Once this modification has been made it will be possible to distinguish between dye moving as a diffusion front and dye concentration increasing evenly through the film. If aggregation or pore blocking is taking place one would not expect to see the latter scenario since one would expect an excess of dye near the surface.

DSC must be practical to install and maintain even if they can be manufactured

easily with high efficiencies. The inclusion of a liquid component in the device and the risk of leakage or degradation by evaporation is fundamentally undesirable to the end user. Solid state DSC present a solution by replacing the liquid electrolyte with a solid state hole conductor. These solid state hole conductors are of wider interest to the scientific community because they can be be used to manufacture flexible electronics such as organic transistors and LEDs. Current is carried by charges coupled to lattice distortions (polarons), the intrinsic density of these polarons is too small to be used in DSC so doping is critical if the hole conductor is to regenerate dye effectively.

Despite the importance of doping in organic semiconductors to a myriad of devices the relationship between conductivity and doping level is not well understood for the small molecule semiconductors used in DSC such as Spiro-OMeTAD. At low doping concentrations the increase in conductivity is less than expected and it has been postulated that this may be due to ineffective doping where some dopants fail to create extra carriers and reside as impurities which act as trapping centres. Trapping takes place due to the electrostatic interaction between polarons and the dipole like potential of these impurities.

A kinetic monte carlo (KMC) model was used to simulate the polaron-dipole interaction at different concentrations of dipoles. This was then compared to the conductivity of Spiro-OMeTAD samples containing only dipole impurities and no active dopants. Qualitatively the results are surprisingly similar given that the KMC model only contains the fundamental details of the system. Moreover, the results are intuitive when one inspects the electrostatic potential landscape generated by a lattice of dipole moments. Finally the detrimental effect of the impurities is consistent with lack of increase in conductivity when the dopant $Li-TFSI$ is introduced to Spiro-OMeTAD. One can conclude that there is scope to increase the conductivity of these organic materials if dopants with small resulting dipole moments can be found. Otherwise one can use high concentrations of dopants to minimise the dipole interaction and achieve the greatest increase in conductivity.

This thesis has covered a broad range of DSC related processes and problems. The underlying message should be that DSC are in many ways surprisingly complex devices which are not completely understood. The fundamentals of recombination, trapping, transport and dye application have complexities which are not entirely expected, but the modelling of DSC has the capacity to add clarity to

our understanding of these processes by playing out the precise consequences of each new finding.

References

[1] K. Kalyanasundaram, editor. *Dye-Sensitized Solar Cells*. EPFL Press, 2010.

[2] R. L. Bailey. *Solar-Electrics*. Ann Arbor Science, 1980.

[3] P. Würful. *The Physics of Solar Cells*. Wiley-VCH, 2009.

[4] D. J. C. Mackay. Sustainable energy – without the hot air, 2007.

[5] A. Cameron. *Desert Energy*. Routledge, 2013.

[6] M. A. Green, K. Emery, Y. Hishikawa, W. Warta and E. D. Dunlop. Solar cell efficiency tables (version 41). *Progress in Photovoltaics: Research and Applications*, 21(1):1–11, 2013.

[7] J. R. Bolton, editor. *Solar Power and Fuels*. Academic Press, Inc., 1977.

[8] M. Grätzel. Photovoltaic and photoelectrochemical conversion of solar energy. *Philosophical Transactions of the Royal Society A: Mathematical, Physical and Engineering Sciences*, 365(1853):993, 2007.

[9] M. Grätzel. Photoelectrochemical cells. *Nature*, 414(6861):338–344, 2001.

[10] B. O'Regan and M. Grätzel. A low-cost, high efficiency solar-cell based on dye-sensitized colloidal TiO2 films. *Nature*, 353(6346):737–740, OCT 24 1991.

[11] J. Nelson. *The Physics of Solar Cells*. Imperial College Press, 2003.

[12] K. Tennakone, G. R. R. A. Kumara, I. R. M. Kottegoda and V. P. S. Perera. An efficient dye-sensitized photoelectrochemical solar cell made from oxides of tin and zinc. *Chem. Commun.*, 0:15–16, 1999.

[13] I. Bedja, S. Hotchandani and P. V. Kamat. Preparation and photoelectrochemical characterization of thin sno2 nanocrystalline semiconductor films and their sensitization with bis(2,2'-bipyridine)(2,2'-bipyridine-4,4'-dicarboxylic acid)ruthenium(ii) complex. *The Journal of Physical Chemistry*, 98(15):4133–4140, 1994.

[14] A. Yella, H. Lee, H. Tsao, C. Yi, A. Chandiran, M. Nazeeruddin, E. Wei-Guang Diau, C. Yeh, S. Zakeeruddin and M. Grätzel. Porphyrin-sensitized solar cells with cobalt (ii/iii)based redox electrolyte exceed 12 percent efficiency. *Science*, 334(6056):629–634, 2011.

[15] U. Bach, D. Lupo, P. Comte, J.E. Moser, F. Weissörtel, J. Salbeck, H. Spreitzer and M. Grätzel. Solid-state dye-sensitized mesoporous tio2 solar cells with high photon-to-electron conversion efficiencies. *Nature*, 395:583–585, 1998.

[16] J. Burschka, A. Dualeh, F. Kessler, E. Baranoff, N. Cevey-Ha, C. Yi, M. Nazeeruddin and M. Grtzel. Tris(2-(1h-pyrazol-1-yl)pyridine)cobalt(iii) as p-type dopant for organic semiconductors and its application in highly efficient solid-state dye-sensitized solar cells. *Journal of the American Chemical Society*, 133(45):18042–18045, 2011.

[17] M. Grätzel. Dye-sensitized solar cells. *Journal of Photochemistry and Photobiology C: Photochemistry Reviews*, 4(2):145 – 153, 2003.

[18] S. Ardo and G. J. Meyer. Photodriven heterogeneous charge transfer with transition-metal compounds anchored to tio2 semiconductor surfaces. *Chem. Soc. Rev.*, 38:115–164, 2009.

[19] J. Lagemaat and A. J. Frank. Effect of the surface-state distribution on electron transport in dye-sensitized tio2 solar cells: Nonlinear electron-transport kinetics. *The Journal of Physical Chemistry B*, 104(18):4292–4294, 2000.

[20] B. E. Hardin, H. J. Snaith and M. D. McGehee The renaissance of dye-sensitized solar cells. *Nature Photonics*, 6:162–169, 2012.

[21] P. R. F. Barnes, A. Y. Anderson, J. R. Durrant and B. C. O'Regan. Simulation and measurement of complete dye sensitised solar cells: including the influence of trapping, electrolyte, oxidised dyes and light intensity on steady state and transient device behaviour. *Phys. Chem. Chem. Phys.*, 13:5798–5816, 2011.

[22] M. M. Lee, J. Teuscher, T. Miyasaka, T. N. Murakami and H. J. Snaith. Efficient hybrid solar cells based on meso-superstructured organometal halide perovskites. *Science*, 338(6107):643–647, 2012.

[23] V. G. Kytin, J. Bisquert, I. Abayev and A. Zaban. Determination of density of electronic states using the potential dependence of electron density measured at nonzero temperatures. *Phys. Rev. B*, 70:193304, Nov 2004.

[24] J. L. Movilla, G. Garcia-Belmonte, J. Bisquert and J. Planelles. Calculation of electronic density of states induced by impurities in Tio_2 quantum dots. *Phys. Rev. B*, 72:153313, Oct 2005.

[25] J. Bisquert, F. Fabregat-Santiago, I. Mora-Seró, G. Garcia-Belmonte, E. M. Barea and E. Palomares. A review of recent results on electrochemical determination of the density of electronic states of nanostructured metal-oxide semiconductors and organic hole conductors. *Inorganica Chimica Acta*, 361(3):684 – 698, 2008.

[26] L. M. Peter. "Sticky Electrons" Transport and interfacial transfer of electrons in the dye-sensitized solar cell. *Accounts of Chemical Research*, 42(11):1839–1847, 2009. PMID: 19637905.

[27] L. M. Peter. Dye-sensitized nanocrystalline solar cells. *Phys. Chem. Chem. Phys.*, 9:2630–2642, 2007.

[28] W. Albery and P. Bartlett. The transport and kinetics of photogenerated carriers in colloidal semiconductor electrode particles. *Journal of The Electrochemical Society*, 131(2):315–325, 1984.

[29] A. Hagfeldt and M. Grätzel. Light-induced redox reactions in nanocrystalline systems. *Chemical Reviews*, 95(1):49–68, 1995.

[30] W. Shockley and G. L. Pearson. Modulation of conductance of thin films of semi-conductors by surface charges. *Phys. Rev.*, 74:232–233, Jul 1948.

[31] J. Bardeen. Surface states and rectification at a metal semi-conductor contact. *Phys. Rev.*, 71:717–727, May 1947.

[32] T. T. Oanh Nguyen, L. M. Peter and H. Wang. Characterization of electron trapping in dye-sensitized solar cells by near-ir transmittance measurements. *The Journal of Physical Chemistry C*, 113(19):8532–8536, 2009.

[33] J. Nelson. Continuous-time random-walk model of electron transport in nanocrystalline tio$_2$ electrodes. *Phys. Rev. B*, 59:15374–15380, Jun 1999.

[34] K. Schwarzburg and F. Willig. Influence of trap filling on photocurrent transients in polycrystalline tio2. *Applied Physics Letters*, 58:2520, 1991.

[35] J. Bisquert, A. Zaban and P. Salvador. Analysis of the mechanisms of electron recombination in nanoporous tio2 dye-sensitized solar cells. nonequilibrium steady-state statistics and interfacial electron transfer via surface states. *The Journal of Physical Chemistry B*, 106(34):8774–8782, 2002.

[36] J. R. Jennings, A. Ghicov, L. M. Peter, P. Schmuki and A. B. Walker. Dye-sensitized solar cells based on oriented tio2 nanotube arrays: Transport, trapping and transfer of electrons. *Journal of the American Chemical Society*, 130(40):13364–13372, 2008.

[37] K. D. Benkstein, N. Kopidakis, J. van de Lagemaat and A. J. Frank. Influence of the percolation network geometry on electron transport in dye-sensitized titanium dioxide solar cells. *The Journal of Physical Chemistry B*, 107(31):7759–7767, 2003.

[38] L. M. Peter. Characterization and modeling of dye-sensitized solar cells. *The Journal of Physical Chemistry C*, 111(18):6601–6612, 2007.

[39] S. E. Koops, B. C. O'Regan, P. R. F. Barnes and J. R. Durrant. Parameters influencing the efficiency of electron injection in dye-sensitized solar cells. *Journal of the American Chemical Society*, 131(13):4808–4818, 2009.

[40] N. W. Duffy, L. M. Peter, R. M. G. Rajapakse and K. G. U. Wijayantha. Investigation of the kinetics of the back reaction of electrons with tri-iodide in dye-sensitized nanocrystalline photovoltaic cells. *The Journal of Physical Chemistry B*, 104(38):8916–8919, 2000.

[41] J. Bisquert and V. S. Vikhrenko. Interpretation of the time constants measured by kinetic techniques in nanostructured semiconductor electrodes and dye-sensitized solar cells. *The Journal of Physical Chemistry B*, 108(7):2313–2322, 2004.

[42] A. Kambili, A.B Walker, F.L Qiu, A.C Fisher, A.D. Savin and L.M Peter. Electron transport in the dye sensitized nanocrystalline cell. *Physica E: Low-dimensional Systems and Nanostructures*, 14(12):203 – 209, 2002.

[43] L. Dloczik, O. Ileperuma, I. Lauermann, L. M. Peter, E. A. Ponomarev, G. Redmond, N. J. Shaw and I. Uhlendorf. Dynamic response of dye-sensitized nanocrystalline solar cells:? characterization by intensity-modulated photocurrent spectroscopy. *The Journal of Physical Chemistry B*, 101(49):10281–10289, 1997.

[44] L.M Peter and K.G.U Wijayantha. Electron transport and back reaction in dye sensitised nanocrystalline photovoltaic cells. *Electrochimica Acta*, 45(28):4543 – 4551, 2000.

[45] A. C. Fisher, L. M. Peter, E. A. Ponomarev, A. B. Walker and K. G. U. Wijayantha. Intensity dependence of the back reaction and transport of electrons in dye-sensitized nanocrystalline tio2 solar cells. *The Journal of Physical Chemistry B*, 104(5):949–958, 2000.

[46] S. Y. Huang, G. Schlichthrl, A. J. Nozik, M. Grtzel and A. J. Frank. Charge recombination in dye-sensitized nanocrystalline tio2 solar cells. *The Journal of Physical Chemistry B*, 101(14):2576–2582, 1997.

[47] P. Salvador, M. G. Hidalgo, A. Zaban and J. Bisquert. Illumination intensity dependence of the photovoltage in nanostructured tio2 dye-sensitized solar cells. *The Journal of Physical Chemistry B*, 109(33):15915–15926, 2005.

[48] J. Villanueva-Cab, H. Wang, G. Oskam and L. M. Peter. Electron diffusion and back reaction in dye-sensitized solar cells: The effect of nonlinear recombination kinetics. *The Journal of Physical Chemistry Letters*, 1(4):748–751, 2010.

[49] H. Wang and L. M. Peter. A comparison of different methods to determine the electron diffusion length in dye-sensitized solar cells. *The Journal of Physical Chemistry C*, 113(42):18125–18133, 2009.

[50] B. C. O'Regan and J. R. Durrant. Kinetic and energetic paradigms for dye-sensitized solar cells: Moving from the ideal to the real. *Accounts of Chemical Research*, 42(11):1799–1808, 2009. PMID: 19754041.

[51] F. Cao, G. Oskam, G. J. Meyer and P. C. Searson. Electron transport in porous nanocrystalline tio2 photoelectrochemical cells. *The Journal of Physical Chemistry*, 100(42):17021–17027, 1996.

[52] J. Ferber, R. Stangl and J. Luther. An electrical model of the dye-sensitized solar cell. *Solar Energy Materials and Solar Cells*, 53(12):29 – 54, 1998.

[53] M. J. Cass, F. L. Qiu, A. B. Walker, A. C. Fisher and L. M. Peter. Influence of grain morphology on electron transport in dye sensitized nanocrystalline solar cells. *The Journal of Physical Chemistry B*, 107(1):113–119, 2003.

[54] J. A. Anta, J. Idigoras, E. Guillen, J. Villanueva-Cab, H. J. Mandujano-Ramirez, G. Oskam, L. Pelleja and E. Palomares. A continuity equation for the simulation of the current-voltage curve and the time-dependent properties of dye-sensitized solar cells. *Phys. Chem. Chem. Phys.*, 14:10285–10299, 2012.

[55] F. Fabregat-Santiago, J. Bisquert, E. Palomares, L. Otero, D. Kuang, S. M. Zakeeruddin and Michael Grätzel. Correlation between photovoltaic performance and impedance spectroscopy of dye-sensitized solar cells based on ionic liquids. *The Journal of Physical Chemistry C*, 111(17):6550–6560, 2007.

[56] J. Halme, P. Vahermaa, K. Miettunen and P. Lund. Device physics of dye solar cells. *Advanced Materials*, 22(35):E210–E234, 2010.

[57] J. Halme. Linking optical and electrical small amplitude perturbation techniques for dynamic performance characterization of dye solar cells. *Phys. Chem. Chem. Phys.*, 13:12435–12446, 2011.

[58] Q. Wang, J. E. Moser and M. Grätzel. Electrochemical impedance spectroscopic analysis of dye-sensitized solar cells. *The Journal of Physical Chemistry B*, 109(31):14945–14953, 2005.

[59] G. Franco, J. Gehring, L. M. Peter, E. A. Ponomarev and I. Uhlendorf. Frequency-resolved optical detection of photoinjected electrons in dye-sensitized nanocrystalline photovoltaic cells. *The Journal of Physical Chemistry B*, 103(4):692–698, 1999.

[60] J. Bisquert. Theory of the impedance of electron diffusion and recombination in a thin layer. *The Journal of Physical Chemistry B*, 106(2):325–333, 2002.

[61] A. Pitarch, G. Garcia-Belmonte, I. Mora-Sero and J. Bisquert. Electrochemical impedance spectra for the complete equivalent circuit of diffusion

and reaction under steady-state recombination current. *Phys. Chem. Chem. Phys.*, 6:2983–2988, 2004.

[62] J. Bisquert, G. Garcia-Belmonte, F. Fabregat-Santiago, N.S. Ferriols, P. Bogdanoff and E.C. Pereira. Doubling Exponent Models for the Analysis of Porous Film Electrodes by Impedance. Relaxation of TiO2 Nanoporous in Aqueous Solution. *The Journal of Physical Chemistry B*, 104(10):2287-2298, 2000.

[63] V. Sivaram, J. Kirkpatrick and H. Snaith. Critique of charge collection efficiencies calculated through small perturbation measurements of dye sensitized solar cells. *J. Appl. Phys.*, 113:063709, 2013.

[64] N. J. Harrick. *J. Appl. Phys.*, 27:1439, 1956.

[65] J. R. Jennings, F. Li and Q. Wang. Reliable determination of electron diffusion length and charge separation efficiency in dye-sensitized solar cells. *The Journal of Physical Chemistry C*, 114(34):14665–14674, 2010.

[66] P. R. F. Barnes, L. Liu, X. Li, A. Y. Anderson, H. Kisserwan, T. H. Ghaddar, J. R. Durrant and B. C. O'Regan. Re-evaluation of recombination losses in dye-sensitized cells: The failure of dynamic relaxation methods to correctly predict diffusion length in nanoporous photoelectrodes. *Nano Letters*, 9(10):3532–3538, 2009. PMID: 19645462.

[67] J. Bisquert, F. Fabregat-Santiago, I. Mora-Seró, G. Garcia-Belmonte and S. Giménez. Electron lifetime in dye-sensitized solar cells: Theory and interpretation of measurements. *The Journal of Physical Chemistry C*, 113(40):17278–17290, 2009.

[68] P. R. F. Barnes, A. Y. Anderson, S. E. Koops, J. R. Durrant and B. C. O'Regan. Electron injection efficiency and diffusion length in dye-sensitized solar cells derived from incident photon conversion efficiency measurements. *The Journal of Physical Chemistry C*, 113(3):1126–1136, 2009.

[69] H. K. Dunn, P. Westin, D. R. Staff, L. M. Peter, A. B. Walker, G. Boschloo and A. Hagfeldt. Determination of the electron diffusion length in dye-sensitized solar cells by substrate contact patterning. *The Journal of Physical Chemistry C*, 115(28):13932–13937, 2011.

[70] J. Bisquert and I. Mora-Sero. Simulation of steady-state characteristics of dye-sensitized solar cells and the interpretation of the diffusion length. *The Journal of Physical Chemistry Letters*, 1(1):450–456, 2010.

[71] P. R. F. Barnes and B. C. ORegan. Electron recombination kinetics and the analysis of collection efficiency and diffusion length measurements in dye sensitized solar cells. *The Journal of Physical Chemistry C*, 114(44):19134–19140, 2010.

[72] J. Halme, G. Boschloo, A. Hagfeldt and P. Lund. Spectral characteristics of light harvesting, electron injection and steady-state charge collection in pressed tio2 dye solar cells. *The Journal of Physical Chemistry C*, 112(14):5623–5637, 2008.

[73] A. Peic, D. Staff, T. Risbridger, B. Menges, L. M. Peter, A. B. Walker and P. J. Cameron. Real-time optical waveguide measurements of dye adsorption into nanocrystalline tio2 films with relevance to dye-sensitized solar cells. *The Journal of Physical Chemistry C*, 115(3):613–619, 2011.

[74] T. Bessho, E. Yoneda, J. Yum, M. Guglielmi, I. Tavernelli, H. Imai, U. Rothlisberger, M. Nazeeruddin and M. Gratzel. New paradigm in molecular engineering of sensitizers for solar cell applications. *Journal of the American Chemical Society*, 131(16):5930–5934, 2009.

[75] Y. Cao, Y. Bai, Q. Yu, Y. Cheng, S. Liu, D. Shi, F. Gao, and P. Wang. Dye-sensitized solar cells with a high absorptivity ruthenium sensitizer featuring a 2-(hexylthio)thiophene conjugated bipyridine. *The Journal of Physical Chemistry C*, 113(15):6290–6297, 2009.

[76] F. Gao, Y. Wang, D. Shi, J. Zhang, M. Wang, X. Jing, R. Humphry-Baker, P. Wang, S. M. Zakeeruddin and M. Gratzel. Enhance the optical absorptivity of nanocrystalline tio2 film with high molar extinction coefficient ruthenium sensitizers for high performance dye-sensitized solar cells. *Journal of the American Chemical Society*, 130(32):10720–10728, 2008.

[77] H. Imahori, T. Umeyama and S. Ito. Large -aromatic molecules as potential sensitizers for highly efficient dye-sensitized solar cells. *Accounts of Chemical Research*, 42(11):1809–1818, 2009. PMID: 19408942.

[78] M. Wang, X. Li, H. Lin, P. Pechy, S. M. Zakeeruddin and M. Grätzel. Passivation of nanocrystalline tio2 junctions by surface adsorbed phosphinate

amphiphiles enhances the photovoltaic performance of dye sensitized solar cells. *Dalton Trans.*, 0:10015–10020, 2009.

[79] T. Horiuchi, H. Miura and S. Uchida. Highly efficient metal-free organic dyes for dye-sensitized solar cells. *Journal of Photochemistry and Photobiology A: Chemistry*, 164(13):29 – 32, 2004. ¡ce:title¿Proceedings of the Dye Solar Cell Osaka ICP-21 Pre-symposium. Dedicated to Professor Shozo Yanagida on the occasion of his retirement¡/ce:title¿.

[80] W. H. Howie, F. Claeyssens, H. Miura and L. M. Peter. Characterization of solid-state dye-sensitized solar cells utilizing high absorption coefficient metal-free organic dyes. *Journal of the American Chemical Society*, 130(4):1367–1375, 2008.

[81] T. Bessho, E. C. Constable, M. Graetzel, A. Hernandez Redondo, C. E. Housecroft, W. Kylberg, M. K. Nazeeruddin, M. Neuburger and S. Schaffner. An element of surprise-efficient copper-functionalized dye-sensitized solar cells. *Chem. Commun.*, 0:3717–3719, 2008.

[82] N. Kopidakis, N. R. Neale and A. J. Frank. Effect of an adsorbent on recombination and band-edge movement in dye-sensitized tio2 solar cells: evidence for surface passivation. *The Journal of Physical Chemistry B*, 110(25):12485–12489, 2006. PMID: 16800576.

[83] C. Zhang, Y. Huang, Z. Huo, S. Chen and S. Dai. Photoelectrochemical effects of guanidinium thiocyanate on dye-sensitized solar cell performance and stability. *The Journal of Physical Chemistry C*, 113(52):21779–21783, 2009.

[84] M. K. Nazeeruddin, R. Splivallo, P. Liska, P. Comte and M. Grätzel. A swift dye uptake procedure for dye sensitized solar cells. *Chem. Commun.*, 0:1456–1457, 2003.

[85] A. Peic. *Mesoporous Thin-film Materials Studied by Optical Waveguide Spectroscopy.* PhD thesis, Department of Chemistry, University of Bath, 2009.

[86] P. J. Holliman, B. V. Velasco, I. Butler, M. Wijdekop and D.A. Worsley. Studies of dye sensitisation kinetics and sorption isotherms of direct red 23 on titania. *International Journal of Photoenergy*, page Article ID 827605, 2008.

[87] M. Dürr, A. Schmid, M. Obermaier, A. Yasuda and G. Nelles. Diffusion properties of dye molecules in nanoporous tio2 networks. *The Journal of Physical Chemistry A*, 109(17):3967–3970, 2005. PMID: 16833717.

[88] M. K. Nazeeruddin, A. Kay, I. Rodicio, R. Humphry-Baker, E. Mueller, P. Liska, N. Vlachopoulos and M. Grätzel. Conversion of light to electricity by cis-x2bis(2,2'-bipyridyl-4,4'-dicarboxylate)ruthenium(ii) charge-transfer sensitizers (x = cl-, br-, i-, cn- and scn-) on nanocrystalline titanium dioxide electrodes. *Journal of the American Chemical Society*, 115(14):6382–6390, 1993.

[89] T. Watson, P. Holliman and D. Worsley. Rapid, continuous in situ monitoring of dye sensitisation in dye-sensitized solar cells. *J. Mater. Chem.*, 21:4321–4325, 2011.

[90] B. O'Regan, L. Xiaoe and T. Ghaddar. Dye adsorption, desorption, and distribution in mesoporous tio2 films, and its effects on recombination losses in dye sensitized solar cells. *Energy Environ. Sci.*, 5:7203–7215, 2012.

[91] V. Gusak, L. Heiniger, M. Grätzel, C. Langhammer, and B. Kasemo. Time-resolved indirect nanoplasmonic sensing spectroscopy of dye molecule interactions with dense and mesoporous tio2 films. *Nano Letters*, 12(5):2397–2403, 2012.

[92] K. H. Lau, L. Tan, K. Tamada, M. S. Sander and W. Knoll. Highly sensitive detection of processes occurring inside nanoporous anodic alumina templates: a waveguide optical study. *The Journal of Physical Chemistry B*, 108(30):10812–10818, 2004.

[93] R.R.A. Syms and J.R. Cozens. *Optical Guided Waves and Devices*. McGraw-Hill Publishing Co., 1992.

[94] J Chilwell and I Hodgkinson. Thin-films field-transfer matrix-theory of planar multilayer waveguides and reflection from prism-loaded waveguides. *Journal of the optical society of America A - Optics image science and vision*, 1(7):742–753, 1984.

[95] D. E. Aspnes. Local-field effects and effective-medium theory: A microscopic perspective. *American Journal of Physics*, 50(8):704–709, 1982.

[96] D.E. Aspnes. Optical properties of thin films. *Thin Solid Films*, 89(3):249 – 262, 1982.

[97] M. K. Nazeeruddin, P. Pechy, T. Renouard, S. M. Zakeeruddin, R. Humphry-Baker, P. Comte, P. Liska, L. Cevey, E. Costa, V. Shklover, L. Spiccia, G. B. Deacon, C. A. Bignozzi and M. Grätzel. Engineering of efficient panchromatic sensitizers for nanocrystalline TiO2-based solar cells. *Journal of the American Chemical Society*, 123(8):1613–1624, FEB 28 2001.

[98] J Crank. *The Mathematics of Diffusion*. Oxford Science Publications, 1975.

[99] H. Shirakawa, E. J. Louis, A. G. MacDiarmid, C. K. Chiang and A. J.Heeger. Synthesis of electrically conducting organic polymers: halogen derivatives of polyacetylene, (ch). *J. Chem. Soc., Chem. Commun.*, 0:578–580, 1977.

[100] A. J. Heeger, S. Kivelson, J. R. Schrieffer and W. P. Su. Solitons in conducting polymers. *Rev. Mod. Phys.*, 60:781–850, Jul 1988.

[101] Z. B. Wang, M. G. Helander, J. Qiu, D. P. Puzzo, M. T. Greiner, Z. M. Hudson, S. Wang, Z. W. Liu and Z. H. Lu. Unlocking the full potential of organic light-emitting diodes on flexible plastic. *Nat. Photon.*, 5(12):753–757, December 2011.

[102] C.D. Dimitrakopoulos and P.R.L. Malenfant. Organic thin film transistors for large area electronics. *Advanced Materials*, 14(2):99–117, 2002.

[103] B. A. Gregg, S. Chen and R. A. Cormier. Coulomb forces and doping in organic semiconductors. *Chemistry of Materials*, 16(23):4586–4599, 2004.

[104] W. F. Pasveer, J. Cottaar, C. Tanase, R. Coehoorn, P. A. Bobbert, P. W. M. Blom, D. M. de Leeuw and M. A. J. Michels. Unified description of charge-carrier mobilities in disordered semiconducting polymers. *Phys. Rev. Lett.*, 94:206601, May 2005.

[105] A. Abate, T. Leijtens, S. Pathak, J. Teuscher, R Avolio, M. E. Errico, J. Kirkpatrik, J. M. Ball, P. Docampo, I. McPherson and H. J. Snaith. Lithium salts as "redox active" p-type dopants for organic semiconductors and their impact in solid-state dye-sensitized solar cells. *Phys. Chem. Chem. Phys.*, 2013.

[106] H. J. Snaith and M. Grätzel. Enhanced charge mobility in a molecular hole transporter via addition of redox inactive ionic dopant: Implication to dye-sensitized solar cells. *Applied Physics Letters*, 89(26):262114, 2006.

[107] A. Abrusci, R. S. Santosh Kumar, M. Al-Hashimi, M. Heeney, A. Petrozza and H. J. Snaith. Influence of ion induced local coulomb field and polarity on charge generation and efficiency in poly(3-hexylthiophene)-based solid-state dye-sensitized solar cells. *Advanced Functional Materials*, 21(13):2571–2579, 2011.

[108] A. R. Barkhouse, H. E. Bishop, B. M. Henry, G. R. Webster, P. L. Burn and H. E. Assender. Improving efficiency of meh-ppv/tio2 solar cells by lithium salt modification. *Organic Electronics*, 11(4):649 – 657, 2010.

[109] H. Bässler. Charge transport in disordered organic photoconductors a monte carlo simulation study. *physica status solidi (b)*, 175(1):15–56, 1993.

[110] A. F. Voter. Introduction to the kinetic monte carlo method. In *Radiation Effects in Solids*, pages 1–23. Springer, 2007.

[111] A. Miller and E. Abrahams. Impurity conduction at low concentrations. *Physical Review*, 120(3):745, 1960.

[112] V. Ambegaokar, B. I. Halperin and J. S. Langer. Hopping conductivity in disordered systems. *Physical review B*, 4(8):2612, 1971.

[113] M. Matsumoto and T. Nishimura. Mersenne twister: a 623-dimensionally equidistributed uniform pseudo-random number generator. *ACM Trans. Model. Comput. Simul.*, 8(1):3–30, January 1998.

[114] V. I. Arkhipov, E. V. Emelianova, P. Heremans and H. Bässler. Analytic model of carrier mobility in doped disordered organic semiconductors. *Phys. Rev. B*, 72:235202, Dec 2005.

[115] V. I. Arkhipov, P. Heremans, E. V. Emelianova and H. Bässler. Effect of doping on the density-of-states distribution and carrier hopping in disordered organic semiconductors. *Phys. Rev. B*, 71:045214, Jan 2005.

[116] J. García-Cañadas, F. Fabregat-Santiago, H. J. Bolink, E. Palomares, G. Garcia-Belmonte and J. Bisquert. Determination of electron and hole energy levels in mesoporous nanocrystalline tio2 solid-state dye solar cell. *Synthetic Metals*, 156(1415):944 – 948, 2006.

[117] J. Kirkpatrick and J. Nelson. Theoretical study of the transfer integral and density of states in spiro-linked triphenylamine derivatives. *The Journal of Chemical Physics*, 123(8):084703, 2005.